Supersonic, Single-Mode and Dual-Mode Kelvin-Helmholtz Instability Experiments Driven by a Laser-Produced Shockwave

by

Willow C. Wan

A dissertation submitted in partial fulfillment
of the requirements for the degree of
Doctor of Philosophy
(Atmospheric, Oceanic, and Space Sciences)
in The University of Michigan
2017

Doctoral Committee:

Professor R. Paul Drake, Co-Chair
Associate Research Scientist Carolyn C. Kuranz, Co-Chair
Assistant Professor Jeremy Bassis
Professor Robert Krasny
Professor Mark B. Moldwin

Willow C. Wan

wwan@umich.edu

ORCID: 0000-0001-8874-4458

To Logan Williams

ACKNOWLEDGEMENTS

Paul Drake and Carolyn Kuranz have my deepest gratitude for their continued guidance over the past years. It is an understatement to say that I underestimated both the emotional strain that I would endure in the pursuit of this thesis, and the persistent patience, mentorship, and support that my advisors would grant me in my academic and personal development.

I would like to thank Guy Malamud, Assaf Shimony, and Matt Trantham for their computational and theoretical support. This thesis could not have happened without their contributions and guidance. I deeply appreciate the time Carlos Di Stefano had taken out of writing his thesis to train me as an experimentalist, and the ingenuity of Sallee Klein and Rob Gillespie, for turning my drawings into a reality.

Logan Williams and Justin Perket kept me grounded during the most difficult years of my life, and provided the emotional support I needed whenever things felt overwhelming.

Finally, I am eternally grateful to my parents, Fayfay and Gary Wan, for raising me and giving the countless opportunities that have brought me this far.

TABLE OF CONTENTS

DEDICATION ii

ACKNOWLEDGEMENTS iii

LIST OF TABLES vi

LIST OF FIGURES vii

LIST OF APPENDICES ix

LIST OF ABBREVIATIONS x

CHAPTER

I. Introduction 1

1.1 Introduction 1
1.2 The Kelvin-Helmholtz instability (KHI) 3
1.2.1 Overview of the KHI 3
1.2.2 Incompressible, linear KHI growth rate 6
1.2.3 Effects of compressibility 10
1.3 High-energy-density (HED) physics 12
1.4 Selected examples of the KHI in a compressible flow 13
1.4.1 KHI in inertial confinement fusion (ICF) experiments 13
1.4.2 KHI at the magnetopause 15
1.5 History of hydrodynamic instability experiments 17
1.5.1 Shock-tubes, wind tunnels, and tilt tables 17
1.5.2 High-energy-density (HED) experiments 23
1.6 Individual contributions 32
1.7 Summary of chapters 33

II. Experimental platform and platform development 36

2.1 Introduction 36
2.2 Target design and methodology 37

2.3 Results and discussion 41
2.4 Conclusion 46

III. Single-mode experiment 48

3.1 Introduction 48
3.2 Experimental design 49
3.3 Results and discussion 50
3.4 Conclusion 55

IV. Dual-mode experiment 56

4.1 Introduction 56
4.2 Experimental setup 58
4.3 Experimental results 62
4.4 Comparison to shear flow simulations, and a discussion of local Mach number effects 69
4.5 Conclusion 73

V. Conclusions and future directions 74

5.1 Conclusion 74
5.2 Future work 75

APPENDICES 78

BIBLIOGRAPHY 116

LIST OF TABLES

Table

3.1	Experimentally inferred parameters are compared to their predicted values.	52
C.1	Shot log for the first experiment (platform development).	91
D.1	Shot log for the second experiment (single-mode).	96
E.1	Shot log for the third experiment (dual-mode).	104

LIST OF FIGURES

Figure

1.1	Evolution of a sinusoidal interface under the influence of the KHI.	4
1.2	KHI observed in the clouds above Capitol Hill, Seattle.	5
1.3	Vortex model by A. Rikanati showing single-vortex and dual-vortex evolution.	6
1.4	Basic flow configuration of the KHI	9
1.5	Contour plot of the ratio of the compressible to incompressible growth rate coefficients, γ/γ_{ic}, in the $M_c - A$ plane.	10
1.6	Regimes of high-energy-density physics.	11
1.7	Schematic of a hohlraum used in indirect-drive ICF experiments.	14
1.8	KHI at magnetospheric boundaries	16
1.9	KHI vortices observed in the Brown and Roshko 1974 experiment	20
1.10	KHI vortices observed in the McFarland et. al 2013 experiment	22
1.11	KHI vortices observed in the Harding et. al 2009 experiment	25
1.12	Schematic of the OMEGA-EP laser bay.	29
1.13	Photo of an expanding blast wave from the Trinity test explosion, taken 0.025 seconds after detonation.	30
2.1	Radiograph by J. Cowan (LANL) showing the transmission of Cu x-rays through the different layers of the revised target.	38
2.2	2D DAFNA simulation showing a density map of the experimental system at $t = 40$ ns.	40
2.3	Data comparison between the original target and the revised target	42
2.4	Density (a,c) and pressure (b,d) distance - time plots from 1D HYADES simulations.	43
2.5	Density (a,c) and pressure (b,d) cell-number - time plots from 1D HYADES simulations.	44
3.1	Schematic view of the single-mode target	49
3.2	Re-calibrated 2D DAFNA simulation showing log(density(g/cm^3)) at $t = 65$ ns.	50
3.3	Single-mode radiographic data at $t = 65$ ns	51
3.4	Normalized single-mode experimental data fit against theoretical predictions with (dashed red) and without (solid black) significant compression	54

4.1 Schematic view of the dual-mode target. 58
4.2 2D DAFNA simulation at $t = 65$ ns, with the 60:120 initial perturbation from Eq. 4.1. 59
4.3 Dual-mode radiographic data at $t = 65$ ns. 62
4.4 Normalized dual-mode experimental data fit against predictions from numerical simulations, with peak-to-valley amplitude on the ordinate and time on the abscissa. 63
4.5 Long-term evolution of the peak-to-valley amplitude vs. time. . . . 66
4.6 Normalized experimental data fit against numerical simulation predictions, with vortex separation distance on the ordinate and time on the abscissa. 68
4.7 Normalized experimental data fit against predictions from a steady, shear flow model with (solid) and without (dashed) significant compression. 70
4.8 Velocity map showing the convective Mach number in a merging vortex-pair. Simulation performed by A. Shimony. 72
A.1 Photo of Rayleigh-Taylor instability (RTI) structure in a soap dispenser 80
A.2 Schematic of the Richtmyer-Meshkov instability (RMI) evolving along a shocked interface. 83
B.1 Vector diagram for the velocity shear calculation 86
C.1 Experiment 1, shot 1 91
C.2 Experiment 1, shot 2 92
C.3 Experiment 1, shot 3 92
C.4 Experiment 1, shot 4 93
C.5 Experiment 1, shot 5 93
C.6 Experiment 1, shot 6 94
C.7 Experiment 1, shot 7 94
D.1 Experiment 2, shot 1 96
D.2 Experiment 2, shot 2 97
D.3 Experiment 2, shot 3 98
D.4 Experiment 2, shot 4 99
D.5 Experiment 2, shot 5 100
D.6 Experiment 2, shot 6 101
D.7 Experiment 2, shot 7 102
E.1 Experiment 3, shot 1 104
E.2 Experiment 3, shot 2 105
E.3 Experiment 3, shot 3 106
E.4 Experiment 3, shot 4 107
E.5 Experiment 3, shot 5 108
E.6 Experiment 3, shot 6 109
E.7 Experiment 3, shot 7 110
E.8 Experiment 3, shot 8 111

LIST OF APPENDICES

Appendix

A. The Rayleigh-Taylor instability (RTI) and Richtmyer-Meshkov instability (RMI) 79

B. Key calculations 84

C. Target development data 90

D. Single-mode data 95

E. Dual-mode data 103

F. Unsharp mask algorithm 112

LIST OF ABBREVIATIONS

AMR Adaptive Mesh Refinement

CHBr brominated polystyrene

CHI iodinated polystyrene

CRF carbonized-resorcinol-formaldehyde

EOS equation of state

HED high-energy-density

HLLC Harten-Lax-van Leer-Contact

ICF inertial confinement fusion

KHI Kelvin-Helmholtz instability

LANL Los Alamos National Laboratory

LLE Laboratory for Laser Energetics

LLNL Lawrence Livermore National Laboratory

MHD magnetohydrodynamic

NIF National Ignition Facility

PAI polyamide-imide

PC polycarbonate

RMI Richtmyer-Meshkov instability

RTI Rayleigh-Taylor instability

SRF shot request form

ABSTRACT

We developed a novel experimental platform that utilizes a laser-produced shock-wave to study the evolution of hydrodynamic instabilities in a steady, supersonic (compressible) flow, from precision-machined and well-characterized seed perturbations. Hydrodynamic instabilities, such as the Kelvin-Helmholtz instability (KHI), are mechanisms that allow a system of fluids to transition to a more stable state through the transport of mass, momentum, and energy. The KHI occurs when a strong shear layer develops between two fluids moving parallel to one another, with a sharp velocity gradient across the interface. When shear forces overcome restraining forces, any disturbance along this interface rapidly grows, and then curls into a vortical structure. This process is ubiquitous in nature and engineering, and can be commonly found in terrestrial systems such as cloud formations and ocean waves, astrophysical systems such as supernovae and magnetospheric boundaries, and laboratory systems such as fusion experiments. In past decades, limitations in our understanding of these processes have led to discrepancies between predictions and observations, particularly in high-energy-density (HED) systems.

This experimental platform was used to produce the first direct measurements of the KHI evolving from single-mode and dual-mode seed perturbations in a compressible flow. The data obtained from single-mode initial conditions provided the first direct measurements of the growth rate and structure of the instability in a compressible flow, while data obtained from the dual-mode initial conditions provided the first direct measurements of the instability's vortex merger rate. After fine-tuning the convective mach number and polytropic index of the equation of state (EOS) to match the observed shock timing and interface deflection, a hydrodynamic code was used

to reproduce the observed structures at scales where they were well-resolved. These data support an inhibition of the growth rate and vortex merger rate of the KHI in a compressible flow.

These results have improved our understanding of the two basic elements of the KHI, the behavior of individual modulations and how two vortices interact with another. These data will contribute to the development of a comprehensive model for the evolution of the KHI from broad-band, multi-mode initial conditions in a compressible, vortex-merger dominated regime.

CHAPTER I

Introduction

1.1 Introduction

"One could nominate hydrodynamic instabilities and turbulence for an award in the category of area of physics in which the least fundamental progress has been made during the last century." -R P Drake, *High Energy Density Physics* (2006).

A physically unstable system is a system that, when disturbed, will evolve in a manner that progressively departs from the initial, undisturbed state. For a classic example taken from mechanics, one can imagine a ball resting upon the top of a hill. Although the ball can remain at rest indefinitely if undisturbed, it will roll off the hill as soon as any motion is imparted upon it. In hydrodynamics, disturbing an unstable system of fluids will result in the formation of intricate structures that lead to the intermixing and rearranging of those fluids. This process will continue until a more stable state is achieved (like the ball coming to a rest at the bottom of a valley), or until others factors disturb this process.

We are motivated to study these instabilities, in part, so that we can accurately predict, account for, and mitigate their effects in engineering systems. A fusion reactor operating by inertial confinement, for example, could theoretically provide a source of clean, efficient, and safe energy. In practice, however, we have yet to produce a

fusion reaction in the laboratory that has yielded a net energy gain (*Zylstra et al.*, 2014; *Moody et al.*, 2014; *Edwards et al.*, 2013; *McCrory et al.*, 2008; *Betti et al.*, 2006). Hydrodynamic instabilities are one of the greatest contributors to performance degradation (*Pickworth et al.*, 2016; *Robey et al.*, 2016), as slight asymmetries along the surface of the fuel pellet or within the radiation source inevitably results in the cold layers of the capsule's shell displacing and diluting the hot fusion fuel. By improving our understanding of these instabilities, we can plan for and alleviate these negative effects.

The study of hydrodynamic instabilities also furthers fundamental science efforts. The vast majority of the known universe exists in a fluid state that can be well-described through adaptations of the Euler equations (§ 1.2.2). Hydrodynamic instabilities, by extension, are found in systems that span all manner of size scales, temperature and pressure regimes, magnetic field strength, and viscosities, to name but a few of the countless parameters. Each of these parameters may contribute to slight differences in the behavior of the instability, such that a model that accurately describes their behavior and contributions in deep-ocean dynamics (*van Haren and Gostiaux*, 2010) may easily over-predict or under-predict their influence at magnetospheric boundaries (*Delamere et al.*, 2013), in planetary atmospheres (*Fromang et al.*, 2016), astrophysical jets (*Gardner and Dwyer*, 2009), stellar ejecta (*Zhelyazkov*, 2015), or in supernova explosions (*Feng et al.*, 2013; *Guzman and Plewa*, 2009). This speaks to the ubiquitous presence of hydrodynamic instabilities, but also to the difficulties inherent to studying them.

While one might apply statistics to draw general conclusions about how various parameters affect the evolution of the instability, this method is complicated by the unsteady nature of uncontrolled systems; researchers typically lack thorough knowledge of the initial conditions that seed the growth of the instabilities we observe in nature, and these instabilities rarely reach advanced stages of evolution without being

repeatedly disturbed by unsteady environmental conditions. Hydrodynamic instabilities are also difficult to study computationally (*Remington et al.*, 2017; *Srinivasan and Tang*, 2014); although the early stages of hydrodynamic instability growth can be well-described by simple equations and ample approximations (e.g. the Boussinesq approximation for nearly incompressible fluids (§ 1.2.2)), a comprehensive model often requires careful attention to the many nonlinear terms that affect the later stages of evolution. The presence of these non-linear terms makes it computationally demanding to run simulations at an adequate resolution to capture non-linear contributions to late-time, large-scale dynamics. Thus, in order to develop a comprehensive model for a given hydrodynamic instability, it becomes necessary to perform dedicated experiments with well-controlled initial conditions that isolate the contribution of specific parameters, and then apply this knowledge back to their respective systems.

This thesis presents my contributions to a series of experiments (*Wan et al.*, 2015, 2017a,b) that studied the effects of compressibility on the evolution of the Kelvin-Helmholtz instability (KHI) (*Choudhury*, 1997; *Shimony*, 2016; *Shimony et al.*, 2016b). As the experimental lead, I was responsible for developing an experimental platform capable of producing the first observations of the KHI evolving from precision-machined, well-characterized seed perturbations in a steady, supersonic flow, and for processing, and analyzing the resulting data.

1.2 The Kelvin-Helmholtz instability (KHI)

1.2.1 Overview of the KHI

The Kelvin-Helmholtz instability (KHI) (*Kelvin*, 1871; *Helmholtz*, 1868) is an iconic hydrodynamic instability that arises when two fluids move parallel to one another at different velocities, with a sufficiently narrow transition region between the fluids. This system, which we refer to as shear flow, becomes unstable when shear

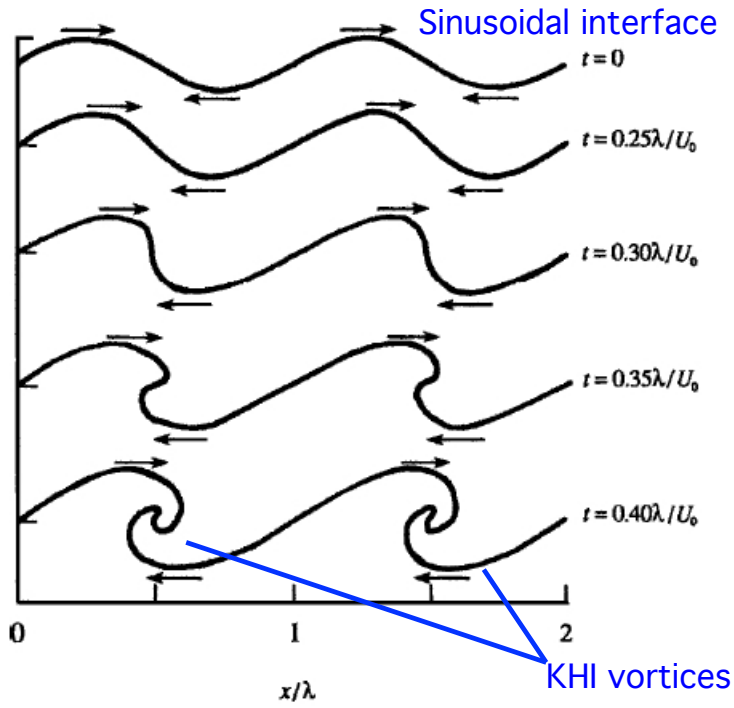

Figure 1.1: Evolution of a sinusoidal interface under the influence of the KHI. The density difference between the fluids is 0, and the velocity difference across the sheet is U_o. Figure adapted from J. S. Turner, *Buoyancy Effects in Fluids*, 1973.

forces overcome restraining forces (such as viscosity and surface tension). The interaction between the velocity shear and the Reynolds stress (turbulent vertical advection) draws kinetic energy out of the main flow in order to feed the growth of vortical structures (*Kundu and Cohen*, 2000). Figure 1.1 (*Turner*, 1973) demonstrates the evolution of a sinusoidal interface under the influence of the KHI, whereas Fig. 1.2 is an example of the KHI in nature.

The two basic components of KHI evolution are single-vortex growth and two-vortex merger (*Rikanati et al.*, 2003). The study of single-vortex behavior encompasses the growth rate and structure of an individual modulation evolving under the influence of the KHI. The single-vortex growth can be simply-described during the early, linear phase of evolution, but rapidly becomes complicated as non-linear terms become significant (*Chandrasekhar*, 1961; *Drake*, 2006). Two-vortex merger describes the interaction between two vortices. In a regime dominated by vortex-merger, larger

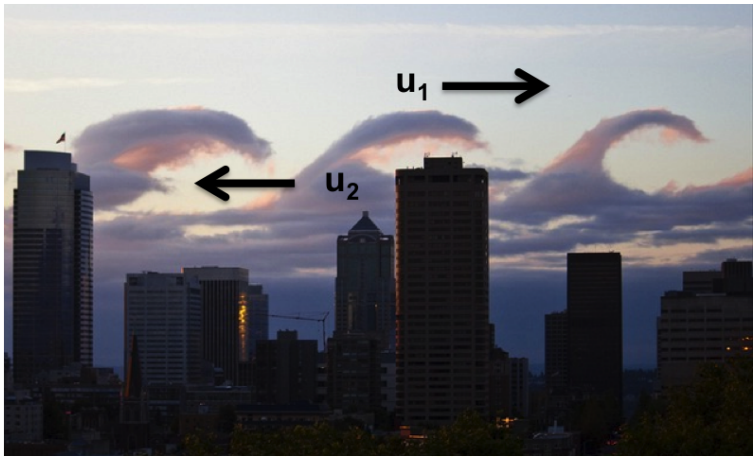

Figure 1.2: KHI observed in the clouds above Capitol Hill, Seattle. Photo credit: Chat Noir Photographie, 2010.

vortices evolve faster and overtake their smaller neighbors, resulting in fewer but larger vortices (*Rikanati et al.*, 2003). The two-vortex-merger rate is still poorly understood, and does not have a simple analytic solution. In order to develop a comprehensive model for the evolution of the KHI, it is necessary to achieve a thorough understanding of these two components of KHI evolution. Chapter III will present the results of our single-mode experiment (*Wan et al.*, 2015), while Chapter IV will present the results of our dual-mode experiment (*Wan et al.*, 2017b).

Figure 1.3 (*Rikanati et al.*, 2003) demonstrates these two aspects of KHI evolution in frames a, b, and c. In these three frames, we can observe two small vortices merging on the left, while one large vortex is far enough away to evolve independently on the right. Given enough time, the large vortex will merge as well. Frame d is a plot of amplitude vs. time for the merging vortices. There are three main stages to KHI vortex merger: the initial, sharp surge in growth is the linear phase of evolution, in which the behavior can be described with simple equations and ample approximations. The second stage is the early non-linear phase, which is also referred to as the co-existence phase. In this phase, the amplitude is relatively steady and oscillates about an asymptotic value. In the final phase of evolution, one vortex is consumed, while the other receives a surge in growth until it reaches a new asymptotic amplitude.

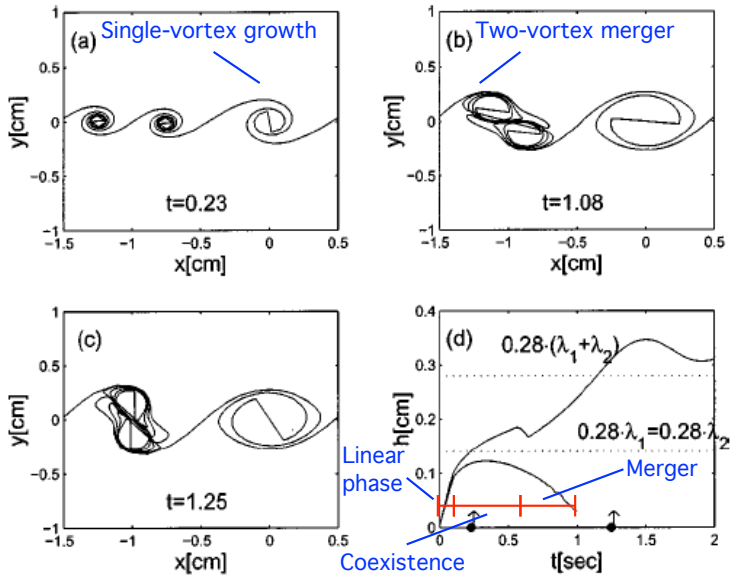

Figure 1.3: Vortex model by A. Rikanati showing single-vortex and dual-vortex evolution. In frames a, b, and c, two small vortices are merging on the left, while one larger vortex evolves independently on the right. In frame d, the height of the two paired vortices are plotted against time. Figure adapted from A. Rikanati et al., *Physics of Fluids*, 2003.

1.2.2 Incompressible, linear KHI growth rate

The growth rate of hydrodynamic instabilities can be determined from the equations of motion. The simplest forms of the equations of motion are the Euler equations for a polytropic gas, as expressed below (*Kundu and Cohen*, 2000; *Drake*, 2006):

$$\frac{\partial \rho}{\partial t} + \nabla \cdot \rho u = 0 \qquad \text{Continuity equation} \qquad (1.1a)$$

$$\rho\left(\frac{\partial u}{\partial t} + u \cdot \nabla u\right) = -\nabla p \qquad \text{Momentum equation} \qquad (1.1b)$$

$$\frac{\partial \rho}{\partial t} + u \cdot \nabla p = -\gamma p \nabla \cdot u \qquad \text{Energy equation} \qquad (1.1c)$$

In these equations, ρ is the mass density, u is the velocity, p is the pressure, and γ is the adiabatic index (the ratio of the specific heats). These three equations represent the conservation of mass, momentum, and energy respectively, and can be

easily customized as necessary by adding situation specific source and loss terms to the right side of the equations. Since the number of unknowns is greater than the number of equations, information about the equation of state must be obtained in order to close these equations.

It is worth noting that even the simplest of these equations is a nonlinear equation. When working with these equations, it is common to make assumptions to reduce the number of nonlinear terms. One such assumption is the Boussinesq approximation (*Kundu and Cohen*, 2000), which assumes that fluids are nearly incompressible. This approximation treats density, ρ, as a constant, and ignores any density differences except when they are multiplied by large values. By applying the Boussinesq approximation, the continuity equation (Eq. 1.1a) can be reduced to: $\nabla \cdot u = 0$. This approximation greatly simplifies the analytic solution, and is generally valid for liquids (but not gases) that we are likely to encounter in daily life. The Boussinesq approximation breaks down in supersonic flows, because blast waves and shock waves (§ 1.5.2.2) can lead to significant compression of the medium, and in HED systems (§ 1.3), in which the energy densities are large compared to the bulk modulus. When the Boussinesq approximation is invalid, the nonlinear terms rapidly become intractable, even for computer simulations. The nonlinear effects of compressibility will be discussed further in the next subsection (§ 1.2.3).

Although growth rates obtained by linearizing and combining the equations of motion (*Chandrasekhar*, 1961) break down at late times in the instability's evolution (once nonlinear terms become significant), they still provide valuable insight into the nature and mechanics of the instability. While the amplitude h is small compared to the wavelength λ (i.e. $h/\lambda \ll 1$), the linearized flow equations result in exponential growth,

$$h(t) = h_o e^{i(kx-\omega t)}. \tag{1.2}$$

In this equation, the angular frequency is $\omega = 2\pi f$, and the wavenumber of the

modulation is $k = 2\pi/\lambda$. When considering this equation, it is important to recall that the angular frequency can be decomposed into a real and an imaginary component, $\omega = \omega_r + \omega_i$, and that it is the imaginary component of the angular frequency that determines the physical growth of the modulation. We refer to this as the growth rate coefficient, $\gamma = -i\omega_i$. We can thus rewrite Eq. 1.2 as

$$h(t) = h_o e^{i(kx-\omega_r t)+\gamma t}. \tag{1.3}$$

The growth rate coefficient, γ, can be determined from the dispersion relation (*Kundu and Cohen*, 2000):

$$\frac{\omega}{k} = \frac{U_2\rho_2 + U_1\rho_1}{\rho_2 + \rho_1} \pm \sqrt{\frac{g}{k}\frac{\rho_2 - \rho_1}{\rho_2 + \rho_1} - \rho_1\rho_2\frac{(U_1 - U_2)^2}{(\rho_2 + \rho_1)^2}}. \tag{1.4}$$

The density of each fluid is denoted by ρ, the velocity of each fluid is denoted by U, and the acceleration of fluid 1 (top) against fluid 2 (bottom) is g. This flow configuration can be seen in Fig. 1.4 (*Kundu and Cohen*, 2012). The condition for instability can thus be defined as:

$$g(\rho_2^2 - \rho_1^2) - k\rho_1\rho_2(U_1 - U_2)^2 < 0. \tag{1.5}$$

The second term in Eq. 1.4 (and the first term in the instability condition, Eq. 1.5) describes the response of the interface to a downward acceleration. One might recognize that this term is either a stabilizing effect when the bottom fluid is heavier than the top fluid ($\rho_2 > \rho_1$, or g > 0), or a destabilizing effect that will contribute to the growth of the KHI via the Rayleigh-Taylor instability (RTI) if the heavier fluid is on top ($\rho_2 < \rho_1$, or g < 0). A discussion on the Rayleigh-Taylor instability (RTI) and Richtmyer-Meshkov instability (RMI) can be found in Appendix A.

The third term in Eq. 1.4 (and the second term in the instability condition, Eq.

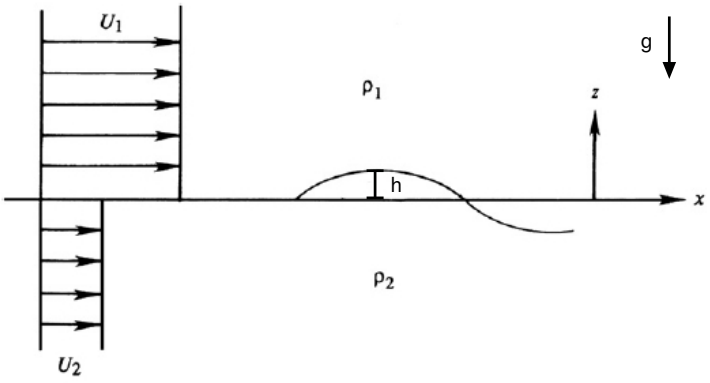

Figure 1.4: Basic flow configuration of the KHI. If $U_1 \neq U_2$, then perturbations along the interface will develop into intricate, vortical structures via the KHI. Figure adapted from Kundu and Cohen, *Fluid Mechanics 5e*, 2012

1.5) describes the effect of the velocity shear, and provides the classical instability condition for the KHI. For any $U_1 \neq U_2$, there exists a sufficiently large k (i.e. a small enough wavelenth) for the system to become unstable. (In various contexts, other stabilizing factors that were neglected from the derivation, such as viscosity and surface tension, can help to stabilize small-wavelength features, which is to say when k $\gg$ 1).

In our experiment ($\rho_2 > \rho_1$) the acceleration of the interface, g, is designed to be negligible (*Malamud et al.*, 2013b). Experimental timescales are too short for gravity as such to play a role in this experiment, and there is no measurable acceleration or deacceleration of the shocked interface (*Wan et al.*, 2017b). We can thus simplify Eq. 1.4 and rewrite the classical growth rate coefficient, γ, of the KHI in an incompressible flow (*Chandrasekhar*, 1961; *Drake*, 2006) as

$$\gamma_{ic} = \frac{k\Delta u}{2}\frac{\sqrt{\rho_1\rho_2}}{\rho_1+\rho_2} = \frac{k\Delta u}{2}\sqrt{1-A^2}. \tag{1.6}$$

In this equation, the relative velocity across the interface is Δu, and the Atwood number is $A = (\rho_2 - \rho_1)/(\rho_2 + \rho_1)$.

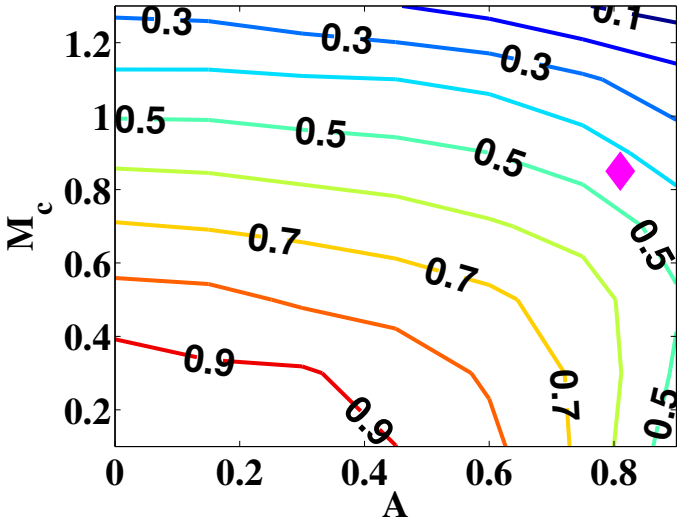

Figure 1.5: Contour plot of the ratio of the compressible to incompressible growth rate coefficients, γ/γ_{ic}, in the $M_c - A$ plane. The diamond at $M_c = 0.85$, $A = 0.81$ represents our experiment. Note that, because of the definition of M_c, the supersonic regime corresponds to $M_c > 0.5$. Originally published in Wan et al., *Physical Review Letters* 2015

1.2.3 Effects of compressibility

In a supersonic flow, effects of compressibility decrease the single-vortex growth rate coefficient (*Landau*, 1944; *Choudhury*, 1997), such that

$$\gamma = \gamma_{ic} \frac{\sqrt{-1 - M_c^2 + \sqrt{1 + 4M_c^2}}}{M_c}, \tag{1.7}$$

where the convective Mach number, M_c, is defined as $M_c = \Delta u/(c_1 + c_2)$, with c being the speed of sound in the respective materials. Because of this definition, the flow becomes supersonic at $M_c \gtrsim 0.5$ in the frame of reference of either fluid. One might notice that in the subsonic limit, $M_c \to 0$, we are left with our classical result, $\gamma = \gamma_{ic}$. In the highly supersonic limit, $M_c > \sqrt{2}$, the compressible growth rate turns imaginary; Eq. 1.7 therefore suggests that the KHI should be stabilized above a convective Mach number of $\sqrt{2}$, though in practice, higher-order non-linear terms become relevant in this regime. The following experiments (*Wan et al.*, 2015,

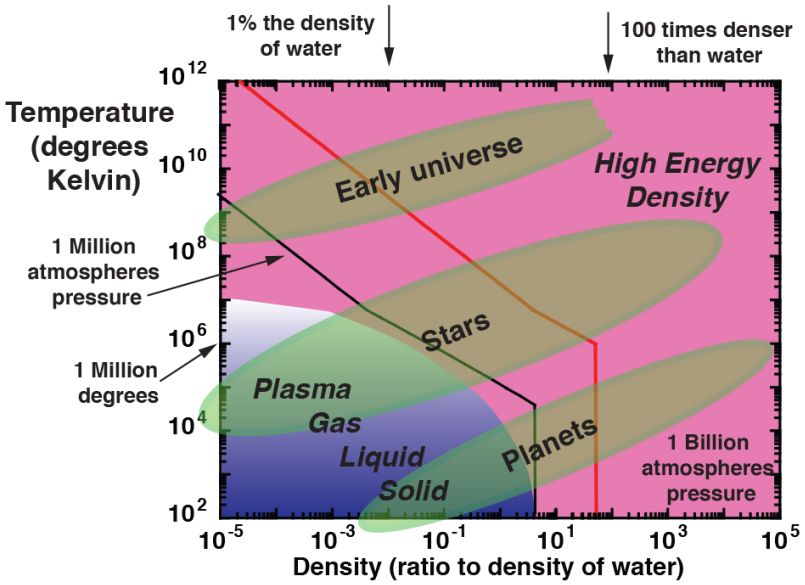

Figure 1.6: Regimes of high-energy-density physics. High-energy-density conditions are common in astrophysical systems. Figure adapted from R.P. Drake, *Physics Today* 2010.

2017b) are designed such that Mach number effects are expected to dominate KHI evolution (*Malamud et al.*, 2013b). Figure 1.5 plots the ratio between the compressible growth rate coefficient and the incompressible growth rate coefficient, γ/γ_{ic}, with the Atwood number, A, along the abscissa and the convective Mach number, M_c, along the ordinate. We can see that our experiment, which is denoted by the magenta diamond, has a convective Mach number $M_c \sim 0.85$ and an Atwood number of $A \sim 0.81$ such that the growth rate is reduced by a factor of $\sim$2. These experiments will be discussed further in Chapter II.

The two-vortex merger rate is more complicated, and there is no simple expression for the effects of compressibility on the two-vortex KHI merger rate. The net effect of compressibility that we will look for in the dual-mode experiment is an extended vortex merger time, which we will elaborate on in Chapter IV.

1.3 High-energy-density (HED) physics

Compressible flows can be studied in HED systems, which have been defined as systems at or above one MBar of pressure (*Drake*, 2006). To better understand the meaning of this, we can consider the bulk modulus, K. In everyday life, one ordinarily considers gases to be compressible, but liquids and solids to be of a fixed density. At a sufficient pressure, however, even solids can be compressed. We typically describe this using the equation:

$$\frac{\Delta P}{K} = \frac{\Delta V}{V}, \qquad \text{Bulk modulus} \tag{1.8}$$

where V is the volume, and P is the pressure (energy density). Here, we can see that the fractional change in volume is proportional to the exerted pressure divided by the material's characteristic bulk modulus. A naive reading of this equation, however, would suggest that applying pressures at or above the characteristic bulk modulus would result in the formation of a singularity. Since this is inconsistent with observations, we can infer that other physical considerations must become significant as one approaches a pressure that is comparable to the bulk modulus. This regime, where enough energy has been concentrated into a small enough space for materials to behave unexpectedly, is what we refer to as HED physics. Figure 1.6 (*Drake*, 2010) shows the HED regime, with temperature and density on the two axes. The conditions we encounter in daily life encompass only a very small subsection of the blue region in the lower-left corner of the map. One MBar is chosen as the threshold pressure for HED physics because it is a sufficient energy density for ordinary solid materials break down into an ionized plasma state that is too dense (sometimes reaching greater-than-solid densities) to be described by traditional plasma theories.

1.4 Selected examples of the KHI in a compressible flow

1.4.1 KHI in ICF experiments

It is important to test the fundamental theory behind hydrodynamic instabilities so that we can improve our ability to predict and mitigate their effect on engineering systems such as ICF experiments (*Pickworth et al.*, 2016; *Robey et al.*, 2016). When two hydrogen atoms are brought close together, the positive charges of their nuclei will attempt to push these particles apart (*Feynman et al.*, 1964). The goal of ICF experiments is to compress a large number of these hydrogen atoms into a small enough space for a long enough period of time such that a significant number of collisions occur in which the short range nuclear forces overcome the weaker but longer ranged repulsive electric forces (*Betti and Hurricane*, 2016; *Pfalzner*, 2006; *Gresh*, 2009). If this can be done efficiently, it will yield a net energy gain. In order to achieve this, the fusion fuel must be compressed at stagnation of a spherically symmetric implosion with little to no pathways for mass and momentum to be lost. In an ICF capsule, engineering components (such as the shell needed to contain the hydrogen gas) create unstable interfaces that result in unwanted mixing; this negatively impacts the temperature of the fusion hot spot and dilutes the fusion fuel, resulting in diminished energy yield.

Laser-driven ICF experiments can be categorized as having either a "direct-drive" or an "indirect-drive" configuration. In the direct-drive configuration, laser beams are directly incident upon the surface of the fusion capsule (*Craxton et al.*, 2015; *Molvig et al.*, 2016). Although this technique is popular around the world, imperfections in the laser optics and within the ICF capsule make the direct-drive configuration prone to asymmetric heating; this leads to an asymmetric radial acceleration, which in turn makes the system susceptible to the development of hydrodynamic instabilities. In the indirect-drive configuration, lasers are aimed at the inner walls of a cylindrical

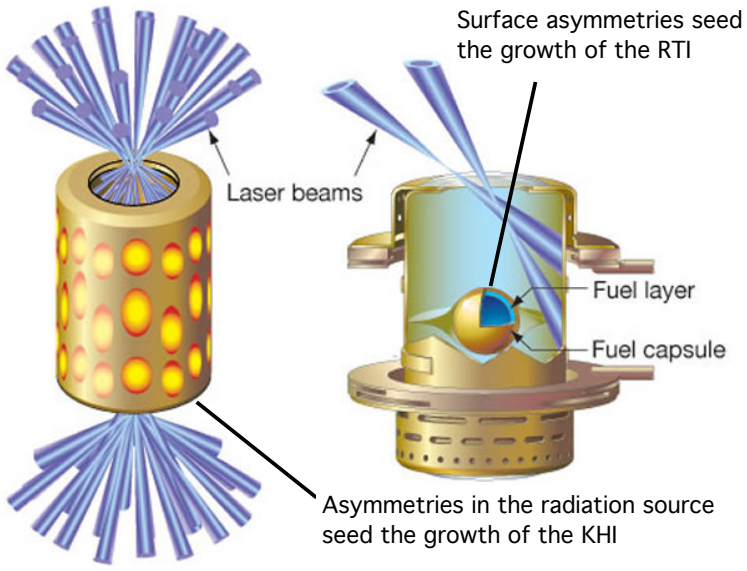

Figure 1.7: Schematic of a hohlraum used in indirect-drive ICF experiments. Image adapted from *Lawrence Livermore National Laboratory (LLNL)* facility documents.

metal tube, which we refer to as a "hohlraum," instead of the surface of the capsule. The irradiated inner walls would then emit x-rays, which produces a more symmetric radiation source. Although this technique diminishes the severity of hydrodynamic instabilities (*Lindl*, 1993; *Yamanaka*, 1999), they remain one of the most significant sources of performance degradation (*Pickworth et al.*, 2016; *Robey et al.*, 2016).

Three hydrodynamic instabilities that commonly contribute to this performance degradation are the RTI, the RMI, and the KHI. The RTI and the RMI are seeded by asymmetries along the surface of the capsule (*Smalyuk*, 2012; *Freeman et al.*, 1977). These asymmetries can be caused by capsule surface roughness (*Remington et al.*, 2016), imprinting from the thin ($\sim$15 nm) membrane that holds the capsule in place (*Nagel et al.*, 2015), or even the shadow of the fill tube (*MacPhee et al.*). A more detailed discussion of the RTI and RMI can be found in Appendix A.

The KHI, on the other hand, is driven by asymmetries in the radiation source. Although the use of hohlraums diminished the severity of surface asymmetries, these indirect-drive experiments must now contend with producing a spherically symmetric

radiation source within a cylindrical capsule, all while the capsule is deforming in response to the lasers ablating material off of the inner walls (*Li et al.*, 2012). The net result is a time-dependent radiation source, that often starts hotter at the poles but ends hotter around the equator (*Town et al.*, 2014; *Slutz et al.*, 2007). This introduces a significant, non-radial component to the velocity, that increases over time as the major-axis of the implosion shifts in response to the dynamic heating. This non-radial velocity can lead to the onset of the KHI, which increases unwanted mixing, while simultaneously decreasing the inward kinetic energy available to start a fusion reaction.

1.4.2 KHI at the magnetopause

Although it is difficult to study the KHI in unsteady systems, doing so can provide tremendous insight into both natural systems and the instability itself. One such example would be the dawn-dusk asymmetry of KHI signatures observed at the magnetospheric boundaries of planets such as Mercury, Saturn, and Jupiter, which defies the conventional understanding of the instability (*Paral and Rankin*, 2013; *Delamere et al.*, 2013; *Johnson et al.*, 2014). (Observations of this dawn-dusk asymmetry are inconclusive around Earth. Mercury lacks an ionosphere, allowing for stronger growth and easier observations of the KHI instability. Jupiter and Saturn have denser, co-rotating plasmas in their magnetospheres, contributing to a consistent dawn-dusk asymmetry in shear velocity. The previously cited papers discuss these conditions in greater detail.)

Around many planets, you have a co-rotating plasma that acts as an extension of the atmosphere (*Gombosi*, 1998). At the same time, you have plasma from the stellar wind bombarding this atmosphere, and wrapping around it. This system is illustrated in Fig. 1.8. Naively, one may assume from the classical description of the KHI (Eq. 1.6) that the shear instability ought to be stronger along the dawn side,

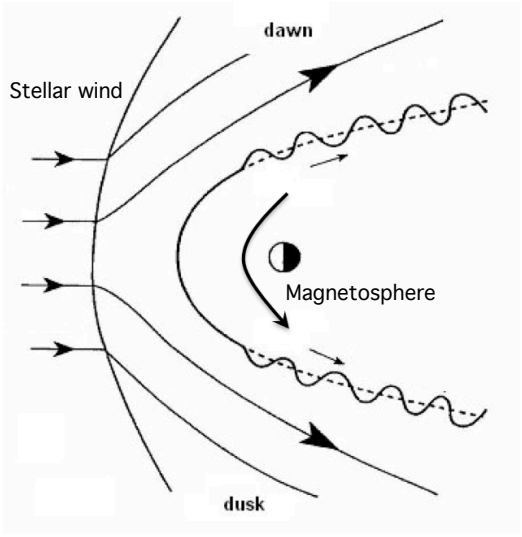

Figure 1.8: KHI at magnetospheric boundaries. The solar wind wraps around a planet's magnetosphere, resulting in a dawn-dusk asymmetry in shear velocities. Observations of the KHI suggest that the KHI is stronger along the dusk side, where the velocity shear is weaker. Image adapted from *Istituto Nazionale di Geofisica e Vulcanologia*.

where the two plasmas are moving in opposite directions, thus maximizing the relative velocity Δu. Observations instead suggest that KHI is consistently stronger on the dusk side, where the relative velocity is weaker.

The papers that reported these findings (*Paral and Rankin*, 2013; *Delamere et al.*, 2013) thoroughly discuss electromagnetic effects, but did not directly address the contributions of compressibility to magnetohydrodynamic (MHD) plasmas (*Miura and Pritchett*, 1982). This is perhaps because the full effects of compressibility are still poorly understood, especially in a MHD regime. An inhibition of the KHI is expected along the frequently supersonic dawn-side shear flow (Eq. 1.7), compared to the frequently subsonic dusk-side (Eq. 1.6), but it is unknown to what extent this behavior may change in a MHD system. Furthermore, since these are unsteady systems, the velocities are in constant flux. This re-emphasizes the point that many fascinating systems exist that can not be well-described by our current understanding of hydrodynamic instabilities, but also can not be thoroughly understood merely

from observations of unsteady, natural systems. To truly understand these systems, it is necessary to perform dedicated experiments that examine the contributions of individual parameters, such as the effects of compressibility, and then systematically determine how these individual contributions interact with one another.

1.5 History of hydrodynamic instability experiments

The experimental platform we developed combined the strengths of several major techniques previously used to study hydrodynamic instabilities. Shock-tubes, wind tunnels, and tilt tables have been used to study sustained, supersonic flows (§ 1.5.1), while HED experiments achieved well-characterized initial conditions (§ 1.5.2). Our experiment required both of these conditions to be met.

1.5.1 Shock-tubes, wind tunnels, and tilt tables

Shock-tubes, wind tunnels, and tilt tables were the primary tools for studying hydrodynamic instabilities in the 1900's. Each of these were capable of sustaining a relatively steady flow for an extended period of time, but could not produce a well-defined seed perturbation along the fluid interfaces. The basic premise of a shock tube is that it contains two or more chambers of pressurized gas that are separated by a thin diaphragm. The experiment begins when the diaphragm is ruptured and the gases are allowed to interact.

The first shock-tube was constructed in 1899 by the French scientist Paul Vieille, though the term "shock-tube" was not used in literature until the 1940's (*Vieille*, 1899; *Henshall*, 1957). Vieille's shock-tube was 22 mm in diameter, 20 feet long, and achieved gas pressures of 27 atm. With this setup, he was able to measure shock velocities of M $\sim$ 2. After a lull in shock-tube research, the design was revisited by Payman and Shepherd in 1946. Payman and Shepherd applied pressure to one chamber of their shock tube until it was sufficient to rupture a copper diaphragm

(*Payman and Shepherd*, 1946). Both of these early experiments were fairly simple, and studied the propagation of shock waves and blast waves through air. Although the pressure ratios and initial interfaces were poorly controlled, they set the standard for future shock-tube experiments.

It is of interesting historical note that the first shock-tube was created at around the same time as the first wind tunnel, and that they were generally considered to be early rivals. Wind tunnels could sustain a steady flow for a much longer duration than shock-tubes, but their early designs had a maximum airflow limit at Mach numbers approaching unity (*Kundu and Cohen*, 2000). Thus, while both have useful applications to the study of hydrodynamic instabilities, shock-tubes struggled to achieve low Mach number systems (*Griffith*, 1952), while wind tunnels struggled to achieve high Mach number systems (*Pope and Goin*, 1978). Wind tunnels were used in early experiments by Schubauer and Skramstad (*Schubauer and Skramstad*, 1947) to investigate the transition of a laminar flow into a turbulent flow, as well as early experiments by Liepmann and Laufer, who provided measurements of turbulent fluctuations and turbulent shear (*Liepmann and Laufer*, 1947). A variant of a wind-tunnel was also used by Freymuth, who obtained the first clear images of vortex-merger by photographing smoke that was introduced into a stream of air (*Freymuth*, 1966).

Shock-tubes and wind tunnels both became popular for hydrodynamic instability experiments around the 1970's. At the end of the 1960's, Meshkov used a shock-tube to perform an experimental verification of the RMI, which was the first major experiment to explicitly study hydrodynamic instabilities in decades, if not centuries (*Meshkov*, 1969). Meanwhile, three notable experiments expanded upon the wind-tunnel work by Liepmann and Laufer. Wygnanski and Fielder studied a 2D incompressible mixing layer in greater detail, by using anemometers and a conditional sampling technique to measure and define turbulent and non-turbulent zone averages (*Wygnanski and Fiedler*, 1970). Spencer and Jones measured the mixing layer be-

tween two streams at variable shear velocities (*Spencer and Jones*, 1971). Brown and Roshko's experiment is perhaps the most notable of these three, in that it emphasized and established the role of coherent (KHI) structures in a system's transition to turbulence (*Brown and Roshko*, 1974). Brown and Roshko created a new apparatus (*Papamoschou and Roshko*, 1988) based on the design of wind tunnels and shock-tubes that produced two pressurized streams of gas with variable flow velocities (*Papamoschou and Roshko*, 1988), as seen in Fig. 1.9. Although Brown and Roshko's experiments lacked a well-controlled interface, the data they produced continues, to this day, to contribute to statistical analyses of incompressible KHI vortex-merger models and the transition to turbulence (*Rikanati et al.*, 1998, 2003; *Shimony*, 2016). Brown and Roshko's facility was also used for Konrad's research into the Reynold's number effects on turbulent shear flows (*Konrad.*, 1977), which was later expanded upon by Dimotakis who studied the entrainment ratio and the growth of the turbulent mixing layers (*Dimotakis*, 1986).

Concurrent with the shock-tube and wind tunnel experiments of the 1970's was a tilt table experiment by Winant and Browand (*Winant and Browand*, 1974). Whereas the previous work had studied the behavior of gases, Winant and Browand studied the flow between two streams of water and produced large-scale vortical structures. Like Brown and Roshko (*Brown and Roshko*, 1974), Winant and Browand produced quantitative measurements of vortex merger, but they did so at much lower Reynolds numbers. The Reynolds number is a dimensionless ratio of inertial forces to viscous forces, and helps to predict the transition to a turbulent flow (*Kundu and Cohen*, 2000). It is defined as $Re = uL/\nu$, where u is the velocity of the fluid, L is the characteristic length scale, and ν is the kinematic viscosity of the fluid. While the shock-tube and wind tunnel experiments discussed above had Reynolds numbers of 10^3 to 10^6 (a regime in which viscosity is negligible), Winant and Browand's experiment had a Reynolds number between 45 (at the source) to 850 (50 cm away). (For

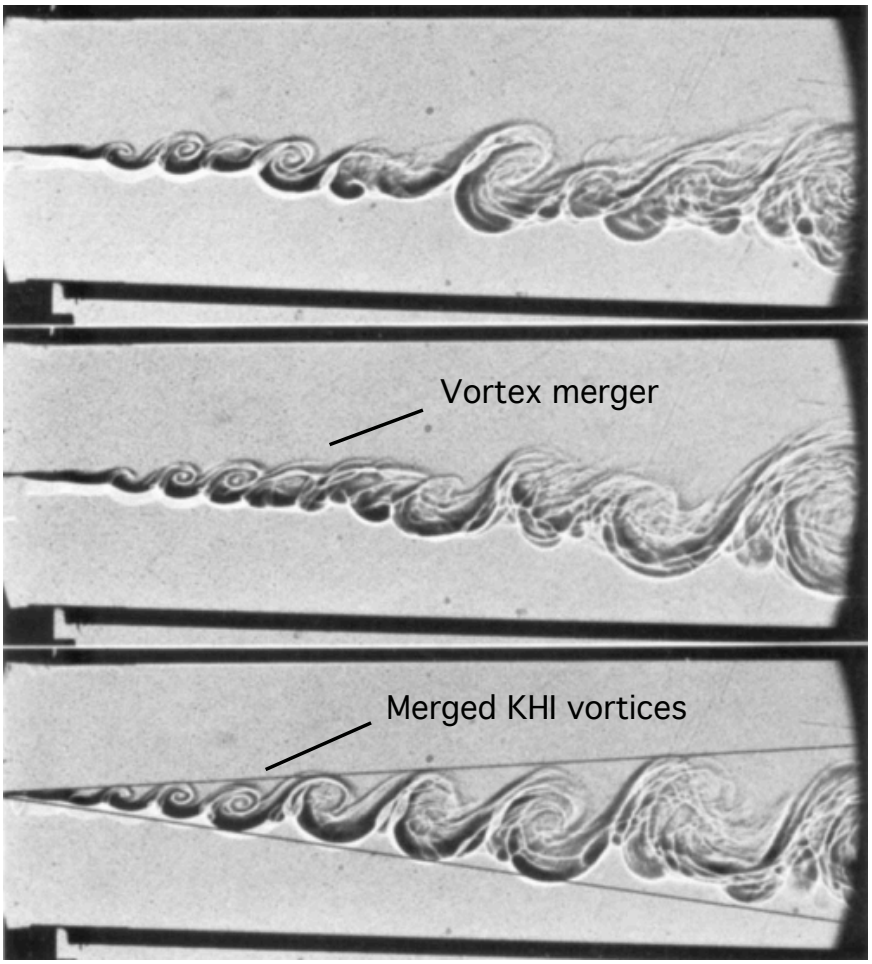

Figure 1.9: KHI vortices observed in the Brown and Roshko 1974 experiment. Shadowgraphs are taken at random times during experiment. The gases (Nitrogen and Helium) are introduced from the left. Over time, they merge into fewer but larger vortices. Figure adapted from Brown and Roshko, *Journal of Fluid Mechanics* 1974.

reference, our own experiment had a Reynolds number of $\sim 10^6$ (*Malamud et al.*, 2013b)). The experiments performed by Winant and Browand inspired a significant amount of computational and theoretical work, including studies of the instability and merger of isolated vortices (*Overman II and Zabusky*, 1982), the relaxation of elliptical vortices to an axisymmetric state (*Melander et al.*, 1987a,b), two-vortex merger (*Melander et al.*, 1988) (§ 1.2.1), and the stabilization of a vortex strip (*Dritschel*, 1989).

Over the next several decades, many groups continued to use tilt tables to study the KHI in a mid-to-low Reynolds number regime (in which viscosity is relevant). Some of the more notable among these experiments include Shyh and Munson's investigation into the stability of a high-viscosity oscillating shear layer (*Shyh and Munson*, 1985), Couder and Badevant's use of thin liquid films to study the vortex merger process in 2D flows (*Couder and Basdevant*, 1986), Thorpe and Holt's investigation into the influence of shallow upper and lower boundaries on the KHI (*Thorpe and Holt*, 1995; *Holt*, 1998), and Yoshikawa and Wesfreid's study of oscillatory behavior in a viscous shear flow (*Yoshikawa and Wesfreid*, 2011a,b). Although these papers contributed to our understanding of the KHI, their direct relevance to our experiment is limited, since our experiment is in a high-Reynolds number regime (negligible viscosity) and studies the evolution of a well-controlled seed interface.

At the turn of the millennium, Slessor expanded upon Brown and Roshko's work by using wind tunnels to study the evolution of the KHI in a compressible flow (*Slessor*, 1998; *Slessor et al.*, 2000). Slessor produced supersonic flows that merged over wedges, and observed an inhibition of the growth rate of the KHI, which was a significant milestone in the study of compressibility on the KHI. A commonality between this experiment and Brown and Roshko's, however, is that while wind-tunnel experiments proved effective for studying turbulent flows and the transition to turbulence, they still generated uncontrolled, multimode initial conditions.

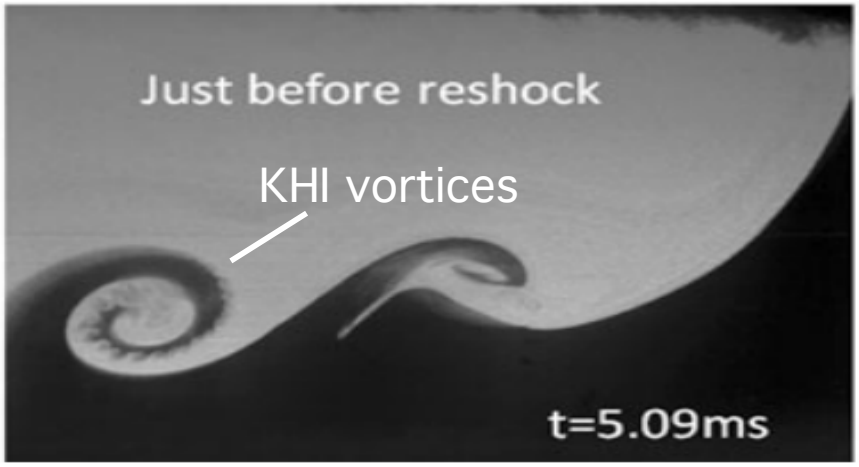

Figure 1.10: KHI vortices observed in the McFarland et. al 2013 experiment. The data was produced in an inclined shock-tube, with an unknown initial interface, to study the RMI in a reshocked system. Figure adapted from J. McFarland, *Experiments in Fluids* 2013.

Incremental progress has continued to be made on the KHI with shock-tube experiments, largely through secondary observations of the instability. These shock-tube experiments often focused on other instabilities such as the RMI and RTI, or on the evolution of highly turbulent systems (*McFarland et al.*, 2013; *Chapman and Jacobs*, 2006; *Bouzgarrou et al.*, 2012; *Titus et al.*, 2013), for which the geometry of shock tubes is well suited. The shock-tube platform developed a rudimentary capability to seed a perturbation by vibrating the diaphragm at a harmonic frequency, but this standing wave along the interface is imprecise, and the diaphragm that separates the fluids is prone to diffusion. The wind tunnel and shock-tube platforms were able to produce sustained, supersonic flows, but were never able to establish a technique for studying the evolution of well-characterized single-mode or dual-mode interfaces in a shear flow. In Fig. 1.10, we can see KHI vortices that were unintentionally produced during McFarland's 2013 shock tube experiment studying the effects of a reshock on the RMI (*McFarland et al.*, 2013). The shock-tube is inclined, reminiscent of tilt table experiments. The high-resolution diagnostics, long experimental timescales, and large-scale features allow us to resolve KHI vortices evolving along the surface of

larger KHI vortices, but the unknown and unsteady initial interface makes it difficult to perform a quantitative analysis of these structures.

1.5.2 High-energy-density (HED) experiments

One might consider the first demonstration of ICF to be the detonation of the hydrogen bomb in 1952, which was driven by several smaller fission reactions. Following this success, Edward Teller called a meeting in 1957 to review peaceful applications of nuclear detonations, such as excavation and construction (*Beck et al.*, 2011a,b,c). Collaborative discussions during this meeting inspired John Nuckolls to consider scaling down the fusion reaction to milligram scales in order to evaluate the feasibility of commercial fusion power (*Nuckolls*, 1998). Nuckolls played a prominent role in developing the simulations and theory capabilities of the United States' indirect-drive ICF program throughout the 1950's and 1960's (though his work was classified at the time (*Nuckolls et al.*, 1972)), while Ray Kidder worked on the development of the direct-drive approach (*Nuckolls*, 1998). The laser was invented in 1960 at Hughes Research Laboratories (*Hänsch*, 2010), and subsequently incorporated into the United States' ICF program in 1962 as a promising driver mechanism (*Nuckolls*, 1998). At the same time, Nikolai Basov of the USSR proposed the idea of achieving thermonuclear fusion by laser irradiation to the Presidium of the Soviet Academy of Sciences (*Velarde*, 2002), though again, much of this was classified.

Kip Siegel from the University of Michigan founded KMS Fusion in 1967 in order to investigate laser-driven ICF, and then performed the first successful demonstration of laser-driven ICF in 1974 (*Siegel*, 1974). Although KMS Fusion shut down shortly afterwards, these experiments contributed to the modern direct-drive and indirect-drive fusion efforts that are currently being pursued at institutions such as the Laboratory for Laser Energetics (LLE), Lawrence Livermore National Laboratory (LLNL) and Los Alamos National Laboratory (LANL). As discussed in (§ 1.4.1), hydrodynamic

instabilities greatly diminished the energy yield of these experiments, and provided motivation for a new era of hydrodynamic instability research.

The majority of recent HED hydrodynamic instability experiments have been performed at laser facilities (§ 1.5.2.1). Laser-driven experiments can deposit a large amount of energy onto initially solid targets with precision-machined seed interfaces. The tremendous energy densities (§ 1.3) allow solid materials to break down into an ionized plasma state, which can then be described by the equations of motion for a fluid (§ 1.2.2). This allows laser-driven hydrodynamic instability experiments to produce plasmas with well-characterized initial interfaces, which are not attainable in wind-tunnel, shock-tube, or tilt table experiments.

The first laser-driven hydrodynamic instability experiments were performed by Cole et al., who studied the growth of the RTI by irradiating aluminum foils at the Science and Engineering Research Council's Central Laser Facility (*Cole et al.*, 1982). This work was expanded upon in various direct-drive and indirect-drive configurations (*Whitlock et al.*, 1984; *Wark et al.*, 1986; *Grun et al.*, 1987; *Nishimura et al.*, 1988; *Desselberger et al.*, 1990; *Kilkenny*, 1990; *Remington et al.*, 1992; *Marinak et al.*, 1995; *Budil et al.*, 1996) to better understand the role of the RTI in fusion experiments (*Freeman et al.*, 1977). In 1997, Kane et al. used the Nova laser to perform the first hydrodynamic instability experiment that was specifically scaled to core-collapse supernovae (*Kane et al.*, 1997; *Remington et al.*, 1997; *Kane et al.*, 2000), following observations that implied that the RTI played a prominent role in the dynamics of SN 1987A (*Itoh et al.*, 1987; *Ebisuzaki et al.*, 1989). Around this time, Peyser et al. and Dimonte et al. also used the Nova laser to perform the first HED RMI experiments (*Peyser et al.*, 1995; *Dimonte et al.*, 1996; *Dimonte and Schneider*, 1997). Laser facilities continue to be extensively utilized for RTI and RMI experiments to this day, to improve our understanding of ICF implosions and astrophysical environments.

Laser-driven KHI experiments took longer to develop. The first of these exper-

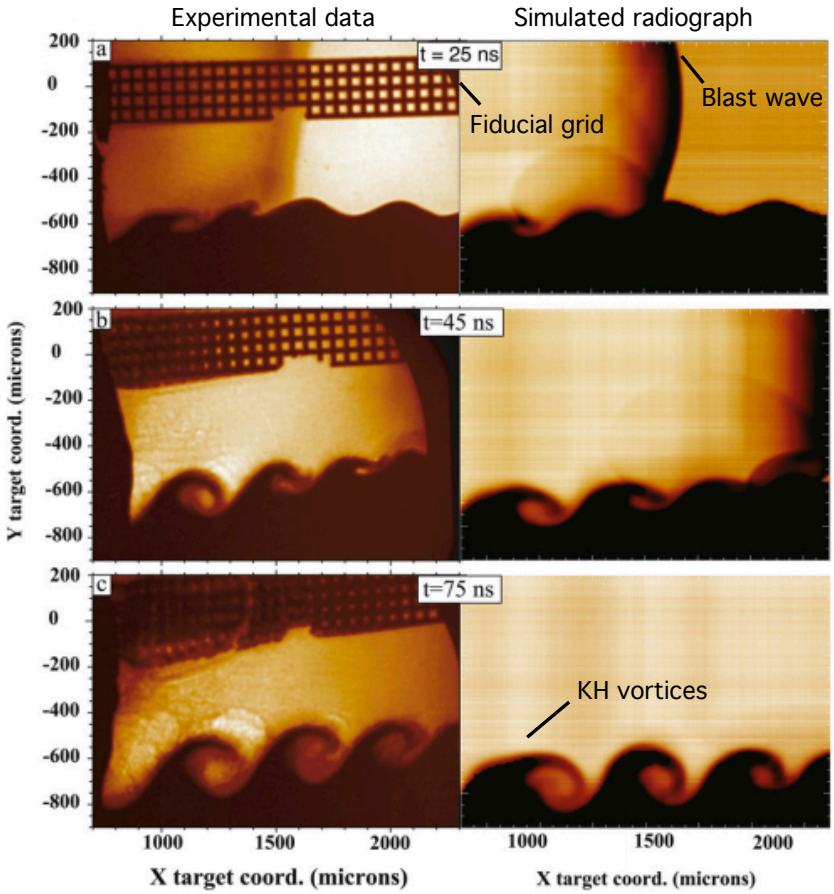

Figure 1.11: KHI vortices observed in the Harding et. al 2009 experiment. Data from the first HED KHI experiment (*Harding et al.*, 2009) are compared to 2D simulated radiographs. A laser-produced blast wave was driven over a 400 μm wavelength, 30 μm amplitude seed perturbation. Figure adapted from E.M. Rutter, *High Energy Density Physics*, 2013.

iments was performed by Hammel (*Hammel et al.*, 1994), but the data were inconclusive and KHI growth was not observed. Another inconclusive experiment was performed by Harding on the NIKE laser, which was intended to study the growth of the KHI from a well-characterized single-mode seed perturbation (*Harding et al.*, 2010a,b; *Harding*, 2010). Experimental timescales were insufficient to observe KHI structure, and the structures that were produced were disturbed by shockwaves within the system. It is also possible that effects of compressibility inhibited the growth of the instability.

Following this, Harding and Hurricane et al. used the OMEGA-60 facility to

produce the first definitive HED KHI experiment, and analyzed them against 2D and 3D simulations (*Harding et al.*, 2009; *Hurricane*, 2008; *Hurricane et al.*, 2009, 2010, 2011, 2012; *Raman et al.*, 2012; *Rutter et al.*, 2013). A comparison of their data to 2D simulated radiographs (*Rutter et al.*, 2013) produced by the CRASH code (*van der Holst et al.*, 2011) can be seen in Fig. 1.11. Unlike the experiments presented in this thesis, Harding and Hurricane's KHI experiment was driven by a blast wave. Blast waves are produced from unsustained depositions of energy, and rapidly decay to subsonic velocities (§ 1.5.2.2). Blast waves also drive the instability growth with a baroclinic deposition of vorticity (*Hurricane*, 2008), which is a different different mechanism than the classic shear-dominated KHI system featured in the experiments presented in this dissertation. The resulting plasma achieved a flow velocity that was initially higher than the experiments described in this dissertation, yet sustained for a much shorter period of time.

The Harding and Hurricane experiments were expanded upon by Smalyuk and Di Stefano, who used the propagation of subsonic blast waves over a roughened interface to produce the first quantitative measurements of turbulent mixing in a HED plasma (*Smalyuk et al.*, 2012, 2013; *Di Stefano et al.*, 2014; *Shimony et al.*, 2016a). Although this experiment was initially driven by a blast wave, the roughened (low-amplitude, multi-mode) interface meant that the features were of sufficiently small wavelength for the KHI growth to be dominated by steady subsonic shear instead of the baroclinic deposition of vorticity (*Di Stefano et al.*, 2014).

A series of experiments were performed concurrently with our own (*Welser-Sherrill et al.*, 2013; *Doss et al.*, 2013a,b, 2015, 2016; *Merritt et al.*, 2015; *Flippo et al.*, 2016) that sustained supersonic, counter-streaming flows over uncontrolled, multi-mode seed perturbations, in order to study the growth of a turbulent mixing layer. Although this supersonic, shear-flow platform had some similarities to our own (*Malamud et al.*, 2013b), these experiments had different initial conditions and studied

different physics.

Our experiments (*Wan et al.*, 2017a, 2015, 2017b; *Malamud et al.*, 2013b), which will be described in the following chapters, expand upon these laser-driven experiments by utilizing the unique capabilities of the OMEGA-EP facility (*Maywar et al.*, 2008) to sustain a steady, supersonic flow over a precision-machined interface for unprecedented durations. This platform was first tested by Di Stefano et al., who utilized a different geometry to study the evolution of the RMI (*Di Stefano et al.*, 2015b,a; *Malamud et al.*, 2013a). This platform combines the well-characterized seed perturbations used in the Harding and Hurricane experiment (*Harding et al.*, 2009; *Hurricane*, 2008), with the sustained, shockwave-driven, supersonic flows found in experiments by Doss et al. (*Doss et al.*, 2013b, 2016) and in shock-tube experiments.

Since the experiments performed in this dissertation, the experimental platform has also been fielded in different geometries. In these new geometries, an oblique shock is used to study the interaction between the KHI, RMI, and RTI. These results will be published by Kuranz et al. and Rasmus et al. in upcoming manuscripts. Currently in development is another experimental platform, related to our own, in which a steady shear flow will be generated by irradiating the inner walls of a hohlraum (§ 1.4.1) to create a long-lived source of x-rays (*Capelli et al.*, 2016).

Other HED experiments relevant to the KHI include Horton and Perez's measurements of vorticity in a magnetized plasma (*Horton et al.*, 2005), and investigations into a magnetized shear flow on the Nevada Terawatt Facility (*Martinez et al.*, 2009; *Wright et al.*, 2009). If this platform is developed further, it might be used to explore the effects of a magnetic field on the KHI, or perhaps measure self-generated fields.

1.5.2.1 HED facilities

Achieving HED conditions requires the use of special facilities. Many HED experiments are performed at laser facilities, which are capable of delivering large amounts

of energy into a small space over a short period of time. The most well-known of these laser facilities are the OMEGA-60 facility at the University of Rochester, and the National Ignition Facility (NIF) at LLNL. These two laser facilities are capable of delivering kJs (OMEGA-60) to MJs (NIF) of energy into mm-scale objects by splitting a single laser into multiple beams, and then irradiating a target from all directions. OMEGA-60 has 60 beams arranged in a near-spherical geometry, while the NIF has 192 beams arranged into four circular rings, optimized for use with cylindrical hohlraums (§ 1.4.1). The high laser energies and the geometry of the beams make the OMEGA-60 facility and the NIF ideal candidates for ICF experiments, but these facilities have also been used in different configurations for various hydrodynamic instability experiments (§ 1.5.2).

Other lasers, such as the Titan laser at the Jupiter Laser Facility or the Hercules laser at the University of Michigan, are smaller lasers that deliver less energy per shot (typically on the order of several hundred Js), but can achieve much higher power and intensity (by depositing the energy in a shorter period of time). These facilities can be used to study physics in a different regime, such as relativistic particle acceleration (*Ledingham and Galster*, 2010).

Our experiment, which requires a large deposition of energy and a sustained source of pressure, is currently only possible to achieve on the OMEGA-EP system, and potentially at the NIF (*Capelli et al.*, 2016). A schematic of the OMEGA-EP facility is shown in Fig. 1.12. Whereas OMEGA-60 and the NIF split a single laser into multiple beams, OMEGA-EP is unique for having four independent, highly-energetic lasers, that are arranged along one hemisphere of the chamber. This unique configuration allows OMEGA-EP to fire its beams sequentially to create a high-power, long-lived source of laser energy, thereby creating and sustaining supersonic, HED conditions for unprecedented durations. This facility, and the experimental platform we developed for it, will be discussed further in Chapter II.

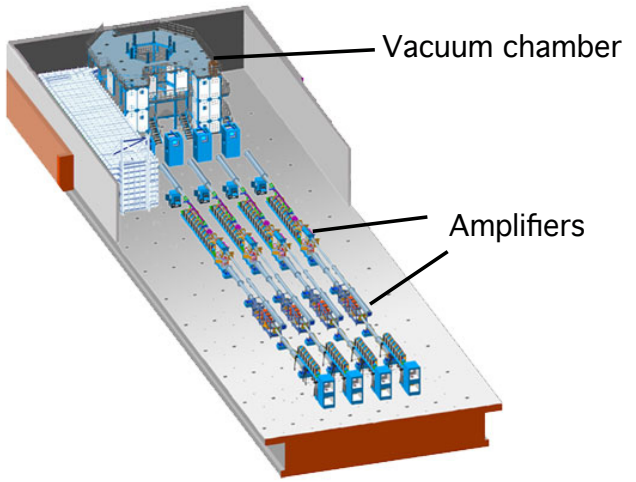

Figure 1.12: Schematic of the OMEGA-EP laser bay. Four independent lasers are amplified and then directed into the vacuum chamber, which contains the experimental target. Figure adapted from LLE facility documents.

1.5.2.2 Blast waves and shock waves

Our experiments are different from those of Harding and Di Stefano (§ 1.5.2) because they drive the growth of the KHI with a shock wave instead of a blast wave. In the context of these experiments, a shock wave is distinguished from a blast wave primarily by its velocity profile as a function of time. At a very basic level, a shock wave is an abrupt change in pressure, density, and temperature. It occurs when a fluid is forced to carry an energy density that exceeds the characteristic energy flux of the medium. The characteristic energy flux of a medium is determined by its characteristic sound speed, c_s. This limits the largest pressure modulation that a sound wave can carry to be of order ρc_s^2, and thus the limit of the energy flux of sound waves is of order ρc_s^3 (*Drake*, 2006). When a fluid carries a greater energy than this, the wave fronts begin to pile upon one another and a shock wave forms. A shock wave is considered to be steady and sustained until this pileup is solved. That is to say, in the frame of reference of the laboratory, the shock wave travels through the medium at a constant velocity.

A shock wave can be found at the leading edge of a blast wave, but a blast

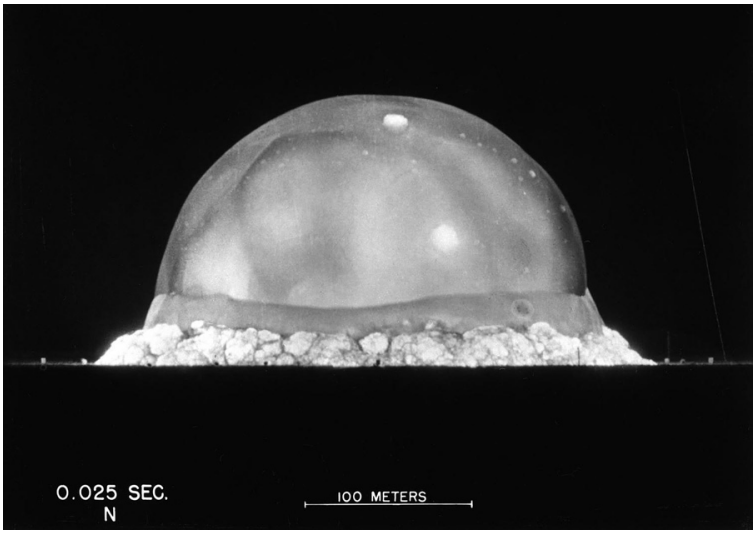

Figure 1.13: Photo of an expanding blast wave from the Trinity test explosion, taken 0.025 seconds after detonation. Image credit: U.S. Department of Defense, July 16, 1945.

wave is the result of an unsustained deposition of energy. As such, blast wave-driven hydrodynamic instability experiments can initially achieve similar conditions to our shock wave driven experiment, but these conditions are not maintained throughout the experiment. We can illustrate this difference with a historical example.

The first atomic bomb was detonated during the Trinity test in New Mexico in 1945, and can be seen in Fig. 1.13. Several years later, the U.S. government released a few photos of the test, each containing a timestamp and a spatial scale. From this, British physicist G. I. Taylor estimated the explosive yield of the bomb with sufficient accuracy to cause great concern over the potential leak of classified information. In truth, he used a rather simple estimate (*Taylor*, 1950b,c).

We can assume first that the blast wave is driven by a single, instantaneous deposition of energy, E. For simplicity, we can also assume that the blast wave expands outwards as a uniform, self-similar sphere. We are given radius of the blast wave, r_{bw}, and time, t, with which to work with, and we can also safely assume that the evolution of the explosion will in some way relate to the density, ρ, of the medium through which it propagates. Putting this all together gives us:

$$r(t)_{bw} \propto E^{\alpha}\rho^{\beta}t^{\gamma} \tag{1.9}$$

By applying the Buckingham-π theorem (*Buckingham*, 1914, 1915), we can see that the coefficients α, β, and γ needed to balance the units of this equation are $\alpha = 1/5$, $\beta =$ -1.5, and $\gamma = 2/5$. Thus, to a first order estimate:

$$r(t)_{bw} = \sqrt[5]{\frac{Et^2}{\rho}} \tag{1.10}$$

By extension, the velocity gives us:

$$v(t)_{bw} = \frac{2}{5}\sqrt[5]{\frac{E}{\rho t^3}} \tag{1.11}$$

This equation is technically incomplete, and breaks down at very early and very late times. However, it still provides a reasonable estimate for the velocity decay of a blast wave. The time-dependent nature of blast waves puts a comparatively low limit on the timescales of blast wave-driven hydrodynamic instability experiments, and complicates the analysis of the instability. A shock wave-driven experiment, meanwhile, allows instabilities to be studied under steady conditions, and makes it easier to draw meaningful conclusions about late-time observations.

In the context of HED experiments, the time scale over which a shock wave can be sustained is dependent upon the duration of the energy source. When the pressure source ends, a rarefaction (expansion) wave propagates forward and overtakes the initial shockwave, causing it to continuously decay as a blast wave. Thus, while a blast wave-driven hydrodynamic instability experiment can produce a supersonic

flow for short durations, it is necessary to continuously drive the system with a sustained pressure in order to study the effects of compressibility on the evolution of the instability.

1.6 Individual contributions

My role in this project was to lead the experiments. This meant that I was responsible for developing an experimental platform, with simulation and design support from G. Malamud and A. Shimony (*Malamud et al.*, 2013b; *Shimony et al.*, 2016b; *Shimony*, 2016), that was capable of sustaining a steady, supersonic flow over a well-characterized seed perturbation. These responsibilities included designing an experimental target that could be affordably and reliably reproduced by our target fabrication team, yet was still within the facility safety requirements, determining the appropriate diagnostics and diagnostic settings to optimize the quality of our data, establishing the orientation and alignment procedure of the target within the target chamber, performing pre-shot metrology to evaluate the quality of the targets after they have been built, diagnosing and addressing any undesired consequences of targets that are built out of specifications, and determining the priorities of the campaign to maximize the amount of useful data that we can obtain within a given day of experiments. Once the initial data were obtained, I was responsible for processing and analyzing these data by writing an image-processing algorithm, comparing the results to design simulations, creating my own simulations to diagnose any problems that may have occurred, designing new targets that could address these issues, and publishing the results of these experiments (*Wan et al.*, 2015, 2017a,b).

1.7 Summary of chapters

This introduction has provided a summary of the KHI, and how its behavior is expected to change in a supersonic flow. The summary begins with a qualitative overview of the hydrodynamic instability, and then discusses the growth rate coefficients of the instability during the initial, linear stage of its evolution. Following this, we describe some of the experiments that predated our own, and then highlight some of the factors that make our experiment unique. Finally, this chapter introduces the concept of HED physics, and gives an overview of some of the most notable facilities used to produce HED systems in the laboratory.

Chapter II provides more information about the experimental platform. It contains excerpts from "Impact of ablator thickness and laser drive duration on a platform for supersonic, shockwave-driven hydrodynamic instability experiments" (*Wan et al.*, 2017a), which has been published in *High Energy Density Physics*. This manuscript gives an overview of the laser drive conditions, primary diagnostic, and experimental target. The manuscript also discusses some design issues that I discovered and addressed during the development stage of the experimental platform. Most notable among these issues was the presence of an unanticipated secondary shockwave, which I refer to as a "reshock." I present the results of simulations I performed to diagnose the problem and improve the design (*Malamud et al.*, 2013b) of the experimental target.

Chapter III presents the results of our single-mode experiment. It contains excerpts from "Observation of single-mode, Kelvin-Helmholtz instability in a supersonic flow," which has been published in *Physical Review Letters* (*Wan et al.*, 2015). The single-mode experiment seeds the growth of the instability with a sinusoidal interface, in order to observe the effects of compressibility on the growth rate and structure of the instability. The results shown here are the first observations and measurements of the KHI evolving from well-characterized single-mode initial conditions in a super-

sonic flow. 2D simulations were calibrated with these data, and overlaid upon the images. The calibrated simulations agreed with data within the diagnostic resolution limit, and the data support the anticipated inhibition of the KHI's growth rate in a compressible flow.

Chapter IV presents the results of our dual-mode experiment. It contains excerpts from "Observation of dual-mode, Kelvin-Helmholtz instability vortex merger in a compressible flow," which is an invited article that has been published in *Physics of Plasmas* (*Wan et al.*, 2017b). The dual-mode experiment seeds the growth of the instability with an interface created by superimposing two sine waves with different wavelengths. The data supplements measurements of the inhibition of the instability's growth rate due to effects of compressibility (*Wan et al.*, 2015), and provides the first measurements of the instability's vortex merger rate. Again, we present a comparison of the data to 2D simulations, and demonstrate that the data and simulations agree within the diagnostic resolution limit.

In Chapter IV, I also present an unpublished figure that compares the vortex-merger data to simulations of the KHI evolving in a pure shear flow, similar to the analysis presented in Chapter III. Using this figure, we examine the reliability of measurements for both the dominant and consumed vortices that exist at the edge of the KH-relevant zone. We also examine local Mach number effects, and discuss their influence on the evolution of the system. This analysis provides a more thorough evaluation of the effects of compressibility on a dual-mode system, and better demonstrates that the calibrated simulations achieve good agreement with data until the system is disturbed.

Chapter V concludes the thesis. In this chapter, I summarize the content of the previous chapters and present ideas for future experiments. Following the conclusion, I have a series of appendices that expand upon various topics. In Appendix A, I discuss the RTI and RMI. These two instabilities are common in many of the systems

that motivated our research into the KHI, and will be discussed further in upcoming papers by Kuranz et. al and Rasmus et. al, who performed experiments with adaptations of the platform presented here. Additionally, the full data-sets produced from these experiments can be found in Appendices C, D, and E. Appendix F contains the Matlab script used to process the data with the contrast-enhancing unsharp mask algorithm.

Chapter II

Experimental platform and platform development

2.1 Introduction

In order to study the effects of compressibility on the KHI, we needed to establish an experimental platform capable of sustaining a steady, supersonic flow over a well-characterized seed perturbation. This manuscript, titled "Impact of ablator thickness and laser drive duration on a platform for supersonic, shockwave-driven hydrodynamic instability experiments," was published in *High Energy Density Physics* (*Wan et al.*, 2017a), and describes the experimental target, laser conditions, and some of the considerations that contributed to the final target design.

In our first experiment, we used a thinner "ablator" (explained below in § 2.2) and reserved one of the laser beams for a backup diagnostic. This configuration is believed to have generated an unintended secondary shockwave, which we refer to as a "reshock." This reshock disturbed the observed KHI structure and contributed to inconsistent results, which will be discussed further in section § 2.3. This explanation is supported by 1D simulations that I performed with the HYADES (*Larsen and Lane*, 1994) code. I addressed the reshock by reallocating the laser beam from the backup diagnostic, and using it to extend the laser-drive duration. This improved the quality and consistency of the results for the second experiment. This improved experimental design produced high-quality single-mode (Chapter III) and dual-mode

(Chapter IV data, and has provided a basis for additional experiments exploring the interaction between the Kelvin-Helmholtz instability (KHI) with the RTI and RMI.

2.2 Target design and methodology

This experimental platform utilized the OMEGA-EP facility to produce a steady, supersonic flow across a well-controlled and well-characterized seed perturbation. The OMEGA-EP facility is unique in the world for having four independently operated, highly energetic lasers (*Maywar et al.*, 2008). For the purpose of these experiments, the target is irradiated with two to three lasers at a wavelength of 351 nm. SG8 distributed phase plates (*Craxton*, 1995) were used to smooth their spatial profiles. Each of these beams contained ∼4 kJ of energy in a 10 ns square pulse, except for a 1 ns transitioning ramp as one laser pulse ends and another, overlapping pulse begins. This 1 ns transition period mitigates any potential problems from laser timing errors, and results in a nominally 19-28 ns square pulse (with a 300 ps rise time), over a 1.1 mm diameter spot size (at full-width, half-maximum), with an average intensity ∼ 4x10^{13} W/cm^2. Currently, OMEGA-EP and the NIF are the only facilities capable of producing this combination of high-energies and long pulse durations. The extended laser pulse maintains pressure on the drive surface in order to sustain a strong, steady shock through the system at maximum compression. This results in a system that can seed instability growth with tightly controlled initial perturbations in a nominally time-invariant supersonic flow.

Figure 2.1 shows a pre-experimental x-ray radiograph of a sample target. Starting from the left, we have a polycarbonate (PC) ($C_{16}H_{14}O_3$, $\rho = 1.1$ g/cm^3) ablator. The lasers are incident upon this layer, and generate the initial shockwave. In the original experiment, the ablator was 185 μm thick and irradiated with a 19 ns laser drive. In the subsequent experiment (*Wan et al.*, 2015), the ablator was increased to 500 μm and irradiated with a 28 ns drive. This change was made to address the possibility

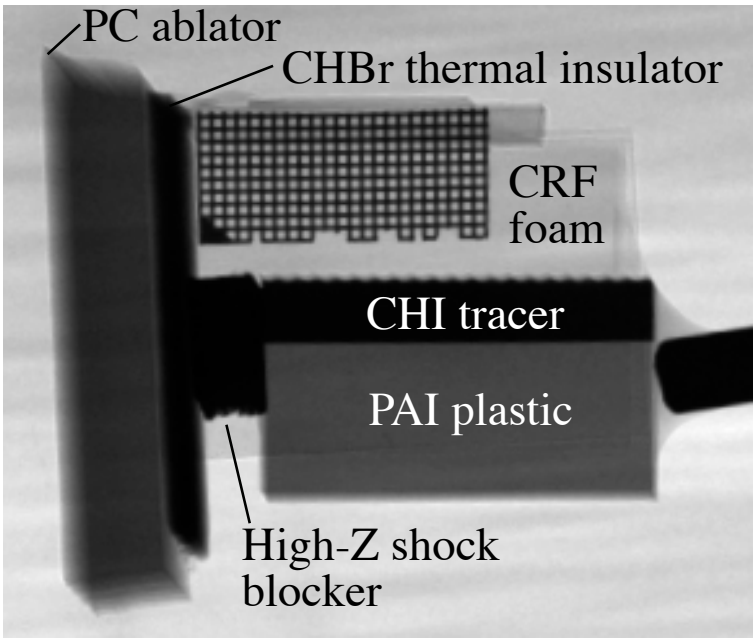

Figure 2.1: Radiograph by J. Cowan (LANL) showing the transmission of Cu x-rays through the different layers of the revised target. The thickness of the PC ablator has been increased from 185 μm to 500 μm.

of a reshock, which we will discuss shortly (§ 2.3). The PC ablator is followed by a 100 μm thick layer of brominated polystyrene (CHBr) ($C_{50}H_{48}Br_2$, $\rho = 1.2$ g/cm^3) thermal insulator, which acts as a heat shield to prevent preheating of the materials that follow. The remainder of the target can be described as the "physics package," and can be divided into a top half and a bottom half.

The top layer of the physics package is carbonized-resorcinol-formaldehyde (CRF) ($C_{1000}O_{48}H_{65}$, $\rho = 0.10$ g/cm^3), which acts as our low-density fluid. Beneath it is an iodinated polystyrene (CHI) ($C_{50}H_{47}I_3$, $\rho = 1.4$ g/cm^3) tracer strip embedded into a density-matched polyamide-imide (PAI) ($C_{22}H_{14}O_4N_2$,$\rho = 1.4$ g/cm^3), which together act as our high-density fluid. The iodinated plastic provides a narrow image plane that absorbs the majority of the Cu x-rays, while the surrounding polyamide-imide is highly transmissive to the Cu x-rays; this mitigates potential smearing of small-scale structure due to misalignment or edge effects. A 100 μm wavelength, 5 μm amplitude single-mode sinusoidal perturbation is machined into the surface of this

plastic. The ~ 0.63 Mbar pressure in the shocked foam drove a shock wave into this plastic material, converting it to plasma and deflecting the foam-plastic interface. We refer to the angle between the unshocked interface and the deflected interface as the deflection angle. Finally, a gold block rests between the thermal insulator and the heavier fluid, which slows down the lower half of the incoming shockwave such that it does not reach the plastic behind it on experimental timescales. This shock blocker maximizes our relative velocity and provides a clean start to the experiment, when the supersonic shear flow is first introduced over the machined perturbation.

The "physics-package" is 1100 μm thick in the span-wise dimension (along the diagnostic axis). In the initial experiment, the CHI tracer was 190 μm thick in the span-wise dimension; this was subsequently reduced to 100 μm in the experiments discussed in Chapter III and Chapter IV in order to improve contrast between the shocked and unshocked plastic, and to create a more narrow image plane. The "physics package" was encased in 200 μm thick beryllium walls, in order to provide additional structural support.

The system reaches an Atwood number of ~ 0.8 and a convective Mach number of ~ 0.85 (*Malamud et al.*, 2013b). The convective Mach number, M_c, is defined as $\Delta u/(c_1 + c_2)$, where Δu is the relative velocity, and c is the speed of sound. From this definition, in the frame of reference of either fluid, the flow is said to be supersonic at $M_c \gtrsim 0.5$. The pressure of the shocked foam was experimentally inferred to be 0.63 $\pm$ 0.08 Mbar (*Wan et al.*, 2015).

Figure 2.2 is a 2D design simulation of the anticipated system 40 ns after the laser drive begins (*Malamud et al.*, 2013b). This simulation was produced in DAFNA, a multi-material, Harten-Lax-van Leer-Contact (HLLC)-based Eulerian hydrodynamics code with interface tracking and Adaptive Mesh Refinement (AMR) capabilities. The simulation is initialized with a 1D Lagrangian radiation hydrodynamics code called HYADES (*Larsen and Lane*, 1994). The materials were treated as ideal gases with

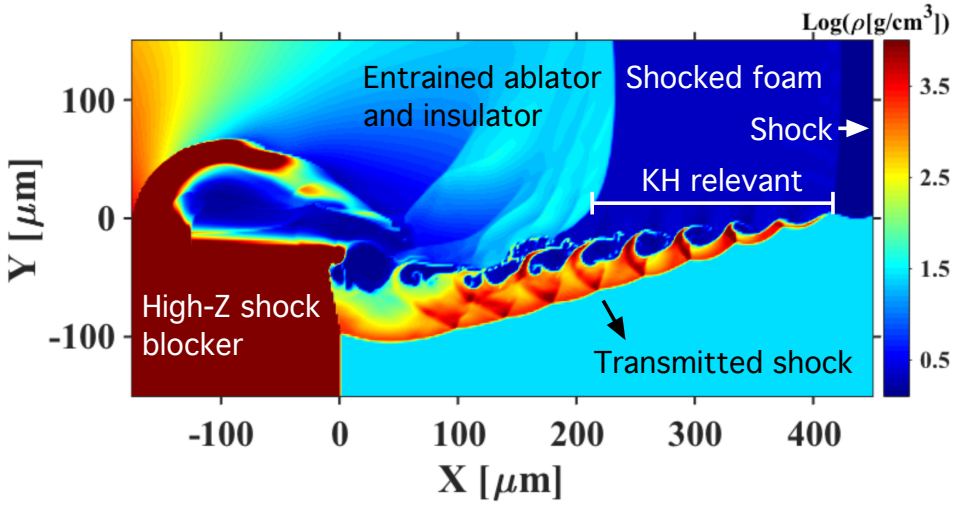

Figure 2.2: 2D DAFNA simulation showing a density map of the experimental system at $t = 40$ ns. A 20 ns laser pulse is incident on a 200 μm thick PC ablator and 100 μm thick CHBr thermal insulator. A shockwave is driven through the foam, producing a strong, supersonic shear over a sinusoidal foam-plastic interface.

an adjustable adiabatic index; in this simulation, the adiabatic index was 1.67 for the CRF foam, and 2.1 for the PC ablator, CHBr insulator, and PAI plastic.

In Fig. 2.2, the shock is moving from the left to the right. As the shock propagates through the foam, a transmitted shock deflects the foam-plastic interface downwards. Along this deflected interface, the modulations begin evolving after the initial shock passes, and the steady, supersonic conditions cease once the thermal insulator that is entrained in the flow disturbs them. As such, the Kelvin-Helmholtz relevant region is defined as the region that is downstream of the shockwave, yet upstream of the entrained material from the insulator and ablator. Modulations that are immediately behind the shock are in the early stages of evolution, whereas those at the downstream edge have been evolving for several times the characteristic evolutionary timescale of the instability (*Frisch*, 1995; *Malamud et al.*, 2013b).

One final laser beam is used to irradiate a 1 mm diameter, 20 μm thick copper foil with 850 J of 1053 nm wavelength laser light, focused to a 200 μm diameter spot size in a 10 ps pulse, to generate x-rays for a spherical crystal imager diagnostic. The spherical crystal imager was used as an x-ray radiography diagnostic; x-rays propagate

through the target to a bent crystal, designed to select out the transmission of Cu K_α radiation (8.0 keV) at a ∼10 to 15 μm spatial resolution (*Stoeckl et al.*, 2012), and are then imaged onto a Fuji^{TM} MS image plate.

2.3 Results and discussion

The platform successfully produced the first data of hydrodynamic instability evolution in a steady, supersonic flow from well-characterized initial conditions (*Wan et al.*, 2015). However, changes needed to be made to the initial target design to improve the quality and consistency of this data. Figure 2.3 provides an example of data taken from two different Kelvin-Helmholtz instability campaigns. The first campaign, shown on the left, had a 185 μm thick PC ablator and 19 ns laser drive, compared to the 500 μm thick PC ablator and 28 ns drive in the revised experiment on the right. The images on top are raw radiographs, and the cutouts are samples of the data after they have been processed through a contrast-enhancing unsharp mask algorithm (*Di Stefano et al.*, 2015a; *Malamud et al.*, 2013b; *Wan et al.*, 2015). This algorithm creates a copy of the image, smeared at the diagnostic spatial resolution, and then subtracts this blurred image from the original to locate edges. This information is then combined with the original image to enhance the visibility of those edge features.

One can see from Fig. 2.3a that while the amplitude of the modulations does change in the original campaign, the modulations do not develop the small-scale rollup structures characteristic to the Kelvin-Helmholtz instability, as seen in the simulation in Fig. 2 (*Malamud et al.*, 2013b). One contributing factor is that the Kelvin-Helmholtz relevant region was smaller than anticipated, resulting in modulations that were disturbed by the entrained insulator and ablator material before they had adequate time to fully develop. This could be due to the foam reaching a higher compression limit than anticipated; in the simulations, the adiabatic index is

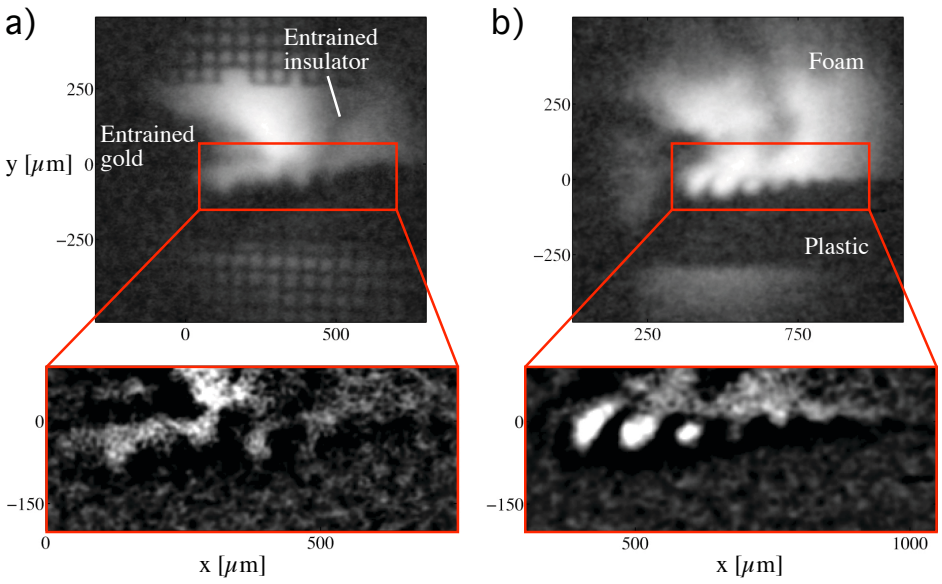

Figure 2.3: Data comparison between the original target and the revised target. **Left:** First experimental campaign with a 185 μm thick ablator and 19 ns drive. **Right:** Second experimental campaign with a 500 μm thick ablator and 28 ns drive. **Top:** Raw radiographic data. **Bottom:** Contrast-enhanced data.

assumed to be 1.67 for the CRF, resulting in a maximum of a 4x compression. First-order estimates of the experimentally observed foam compression, taken by dividing the distance the shock has traveled through the foam by the length of the Kelvin-Helmholtz relevant zone, suggests that the foam reached a compression of $\sim$5x $\pm$ 1.5 (*Wan et al.*, 2015).

The evolution may also have been disturbed by the presence of an unintended secondary shock, which we refer to as a reshock. When the shockwave passes from the thermal insulator into the lower density foam, a rarefaction wave is launched back towards the direction of the drive surface. If this expansion wave reaches the critical surface before the laser drive shuts off, then the large pressure gradient is enough to launch a secondary shockwave through the system that can overtake the initial shock and disturb the evolution of the modulations (*Drake*, 2006). This reshock can be mitigated or prevented by thickening the ablator package, so as to delay the returning rarefaction wave until the drive pressure has released. Figure 2.4 demonstrates this

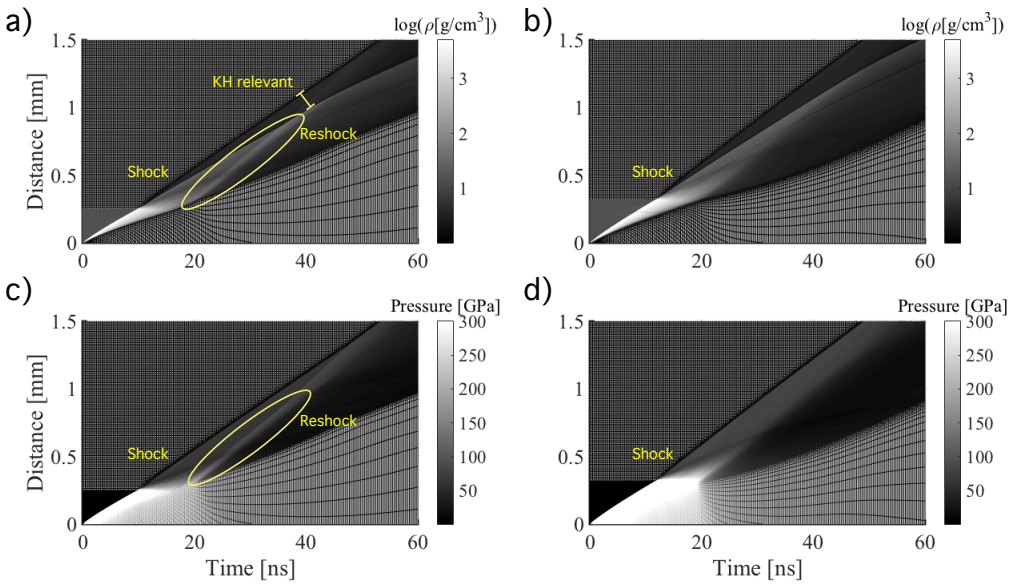

Figure 2.4: Density (a,c) and pressure (b,d) distance - time plots from 1D HYADES simulations. **Left:** 150 μm thick PC ablator. **Right:** 220 μm thick PC ablator.

with a pair of 1D radiation hydrodynamic simulations performed with the HYADES code. This code uses the same laser parameters as Fig. 2.2, but adjusts the initial thicknesses of the PC ablator. Additionally, the PC ablator and CHBr insulator now use polystyrene SESAME equation of state tables instead of an ideal gas model, and the foam uses a carbon foam equation of state table. Various other combinations of equation of state tables or ideal gas adiabatic indices, ranging from 1.4 to 1.75, were also explored.

Figure 2.4 shows density (Fig. 2.4a, 2.4c) and pressure (Fig. 2.4b, 2.4d) changing with time, with time along the abscissa and distance along the ordinate. In Fig. 2.4a and 2.4c, the initial thickness of the PC ablator is 150 μm (35 μm below the nominal experimental thickness (§ 2.2)), whereas in Fig. 2.4b and 2.4d, the initial thickness of the PC ablator is 220 μm (35 μm greater than the nominal experimental thickness). Both are followed by 100 μm of CHBr thermal insulator and 1500 μm of CRF foam, and have identical laser conditions. In Fig. 2.4a and 2.4c, we can observe the reshock overtaking the initial, driving shockwave, which has the potential

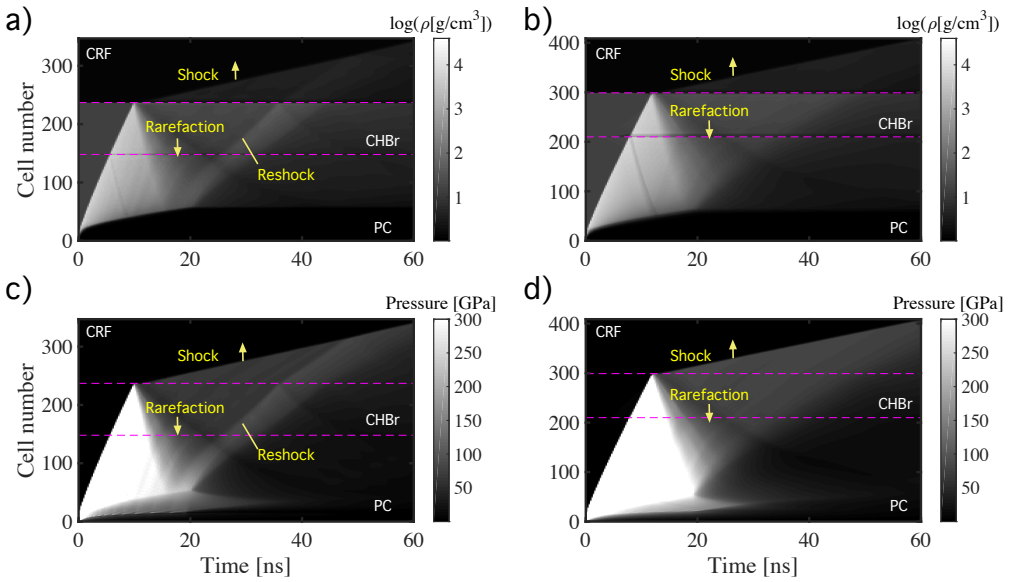

Figure 2.5: Density (a,c) and pressure (b,d) cell-number - time plots from 1D HYADES simulations. Each cell contains an equal mass of the specified material. **Left:** 150 μm thick PC ablator. **Right:** 220 μm thick PC ablator.

to disturb the evolution and fine structure of the shear instability. In Fig. 2.4b and 2.4d, the ablator is thick enough to mitigate this secondary shockwave.

The $\pm$ 35 μm uncertainty in Fig. 2.4 were chosen for two reasons. First and foremost, a reshock always occurred in these simulations when the ablator thickness was reduced to 35 μm below the nominal experimental thickness for all tested combinations of equation of state tables and adiabatic indices, while 35 μm above the nominal experimental thickness was always observed to be free of a reshock. As a secondary reason, the metrology station we used to perform our pre-experimental evaluation of our target had a $\sim \pm 35$ μm uncertainty.

Figure 2.5 presents an alternate view of the same data, with cell number instead of distance along the ordinate. Each cell represents an equivalent mass of the given material, and the transition between materials occurs at pre-defined cell numbers. Again, the reshock can be seen overtaking the original shockwave in Fig. 2.5a and 2.5c, but is not present in Fig. 2.5b and 2.5d.

Depending on which equation of state table or what value adiabatic index is chosen

for the various materials, the thickness of the original ablator package may or may not have reached the threshold thickness required to prevent this reshock. When we further factor in the variability of individual targets (each layer had a thickness tolerance of $\pm$ 15 μm), it is left ambiguous whether or not this reshock may have occurred within the original experiment, and if so, how much of an influence it would have had on the development of the instability.

Both concerns, the insufficient size of the Kelvin-Helmholtz relevant zone and the possibility of a reshock, were addressed in a subsequent campaign by thickening the ablator package and extending the laser pulse length from 19 ns to 28 ns. Extending the duration of the laser pulse extends the maximum duration of the experiment by increasing the length of time over which the shockwave is supported by ablation pressure. This, in turn, provides more time for the primary shockwave to outpace the material that has become entrained in the flow, increasing our instability-relevant region. The ablator thickness was increased to 500 μm to compensate for the longer drive duration; this was the thinnest piece that could be ordered from our supplier that still exceeded the threshold thickness needed to eliminate the reshock for all tested combinations of equation of state tables and adiabatic indices. After this change, data and simulation consistently achieved good agreement for large and medium-scale structures (*Wan et al.*, 2015).

Due to limitations in time and experimental resources, we were unable to perform an experiment in which we changed only the ablator thickness or the laser drive duration exclusively. This remains a topic of interest that can be explored in future experiments. This experiment could also explore the extent to which different types of hydrodynamic instabilities are affected by the reshock (e.g. whether the Rayleigh-Taylor and Kelvin-Helmholtz instabilities are affected to the same degree by the presence of a reshock).

2.4 Conclusion

An experimental platform was developed for OMEGA-EP to study the evolution of hydrodynamic instabilities in a steady, supersonic flow. An extended laser pulse was used to drive a shockwave over a well-characterized material interface. After analyzing the data from an initial Kelvin-Helmholtz instability experiment, it was determined that we needed more consistent results and a larger Kelvin-Helmholtz relevant zone. We achieved this by increasing the duration of the laser drive, and then taking our radiographic data at a later time. This change required a thicker ablator, which also addressed the possibility of a reshock that didn't come through in the design stage. This may have been due to the manner in which data was imported from a radiation-hydrodynamics code (HYADES) into a purely hydrodynamic code (DAFNA). When a laser deposits energy into a material, it produces a pressure-profile that is non-uniform with depth, and which changes in shape when the laser shuts off. The DAFNA code, which does not have a radiation package, may have incorrectly simulated the release of pressure due to the laser shutting off, which would affect the simulation's ability to model a reshock (*Malamud et al.*, 2013b).

After these changes, the quality and consistency of the experimental data was significantly improved, and the results were well-reproduced with 2D simulations (*Wan et al.*, 2015). The revised platform produced the first measurements of the growth rate and vortex merger rate of the Kelvin-Helmholtz instability in a supersonic flow from well-characterized seed perturbations. The results of the revised single-mode experiment as the subsequent dual-mode experiment will be discussed in Chapter III and Chapter IV respectively.

In future work, the data obtained from these experiments will contribute to the development of a comprehensive model for compressible Kelvin-Helmholtz instability (KHI) behavior. This model can be tested by applying a multi-mode seed perturbation to the revised experimental platform. Other researchers have recently used

adaptations of this experimental platform to explore other hydrodynamic instabilities (e.g. the Rayleigh-Taylor instability or the Richtmyer-Meshkov instability), or the interaction of these instabilities with the Kelvin-Helmholtz instability.

Chapter III

Single-mode experiment

3.1 Introduction

After establishing an experimental platform capable of sustaining a steady, supersonic flow over a well-characterized interface (Chapter II), I applied this platform to a single-vortex experiment to evaluate the effects of compressibility on the growth rate and structure of the KHI. This manuscript, titled "Observation of single-mode, Kelvin-Helmholtz instability in a supersonic flow," was published in *Physical Review Letters* (*Wan et al.*, 2015). In this experiment, we seeded the growth of the KHI with a single-mode sine wave that can be described by the equation: $0.05\lambda\ sin(\frac{2\pi}{\lambda}x)$, where $\lambda = 100\ \mu$m. (Several calibration shots were also taken using a nominally flat interface, to more easily infer parameters such as shock velocity or the deflection angle of the shocked interface). The data obtained from this experiment were the first observations and measurements of the KHI evolving from a single-mode seed perturbation in a steady, supersonic flow.

These data were processed with a contrast-enhancing unsharp mask algorithm (*Di Stefano et al.*, 2015a). The same processing method was then used on a simulated radiograph (*Malamud et al.*, 2013b) to extract a contour representing the unstable interface. The simulated interface was overlaid upon the data, and we find good agreement within the diagnostic resolution limit. The measurements support an in-

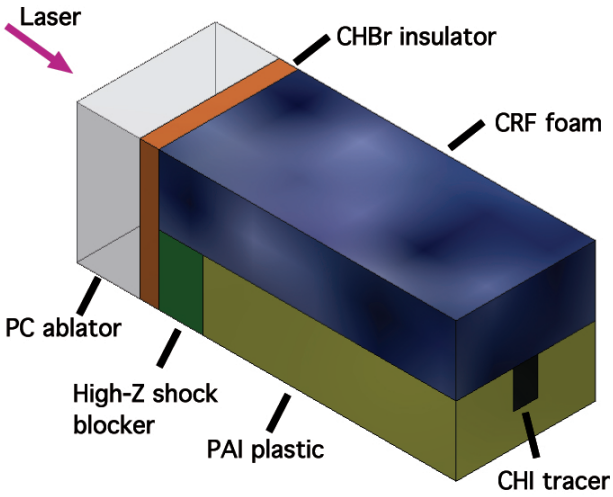

Figure 3.1: Schematic view of the single-mode target. The ablator is a 500 μm thick layer of polycarbonate (PC) ($C_{16}H_{14}O_3$, $\rho = 1.08\ g/cm^3$). The insulator is a 150 μm thick layer of brominated polystyrene (CHBr) ($C_{50}H_{48}Br_2$, $\rho = 1.17\ g/cm^3$). The low-density layer is carbonized-resorcinol-formaldehyde (CRF) ($C_{1000}O_{48}H_{65}$, $\rho = 0.10\ g/cm^3$) foam. The high-Z shock blocker is a 350 μm thick layer of Sn (7.3 g/cm^3). The plastic block consists of a high-density polyamide-imide (PAI) ($C_{22}H_{14}O_4N_2$, $\rho = 1.40\ g/cm^3$), containing a 190 μm wide iodinated polystyrene (CHI) ($C_{50}H_{47}I_3$, $\rho = 1.44\ g/cm^3$) tracer strip of nominally equal density.

hibition of instability's growth rate that matches or exceeds the inhibition predicted from simulations. Several parameters are measured and compared to predictions, including shock velocity and the spacing of the compressed modulations. The results of this experiment set the groundwork for the dual-mode experiment presented in the next chapter.

3.2 Experimental design

This experiment utilized the modified target design presented in Chapter II, and summarized in Fig. 3.1. The longer drive duration sustained drive pressure for ~70 ns, where $t = 0$ corresponds to the time of initiation of the first laser pulse. The thickness of the CHBr thermal insulator was increased from 100 μm (*Wan et al.*, 2017a) to 150 μm due to time and manufacturing constraints from our supplier. The increased thickness further mitigates the possibility of a reshock (Chapter II), at the

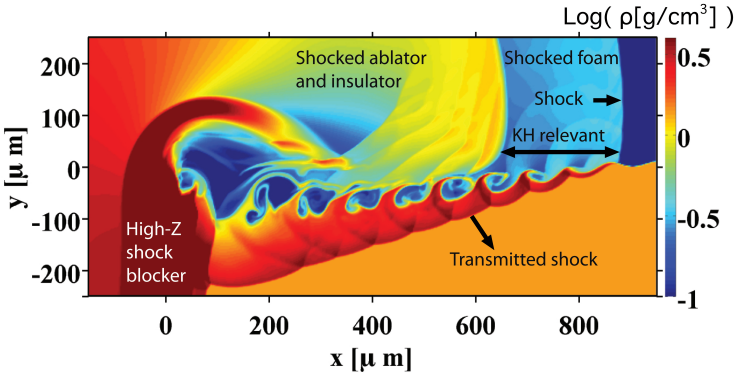

Figure 3.2: Re-calibrated 2D DAFNA simulation showing log(density[g/cm^3]) at t = 65 ns. The sustained drive pressure produces a steady post-shock velocity in the foam to drive KH growth. The part of the system relevant here is the shocked foam, where the ablator and insulator material do not interfere with the dynamics. The re-calibrated simulations suggest that data must be taken later in time to achieve a KH-relevant zone comparable to the one predicted in Fig. 2.2.

cost of slightly diminishing the length of time available to observe KHI growth.

Figure 3.2 shows the anticipated experimental system after the shock wave has propagated about 1 mm through the foam. The design simulations (*Malamud et al.*, 2013b) used the DAFNA code in 2D, initialized with a shock-Hugoniot condition based on 1D radiation hydrodynamic modeling using Hyades (*Larsen and Lane*, 1994) and treating the foam as an ideal gas with an adjustable adiabatic index. The experiment was designed so that the vorticity produced by baroclinic effects was small compared to that driven by the steady, shear flow. Unfortunately, this experimental approach does not enable one to vary M_c significantly.

3.3 Results and discussion

We measured the interface structure with x-ray radiography. The measurement used a spherical crystal imager (*Stoeckl et al.*, 2012) to image Cu K_α x-rays, produced by irradiating a 1 mm dia. Cu foil with 850 J of laser light of 1053 nm wavelength, focused to a 200 μm-dia. spot, in a 10 ps pulse, at a selected time of interest. These x-rays propagated through the target and to the crystal, which imaged them onto a

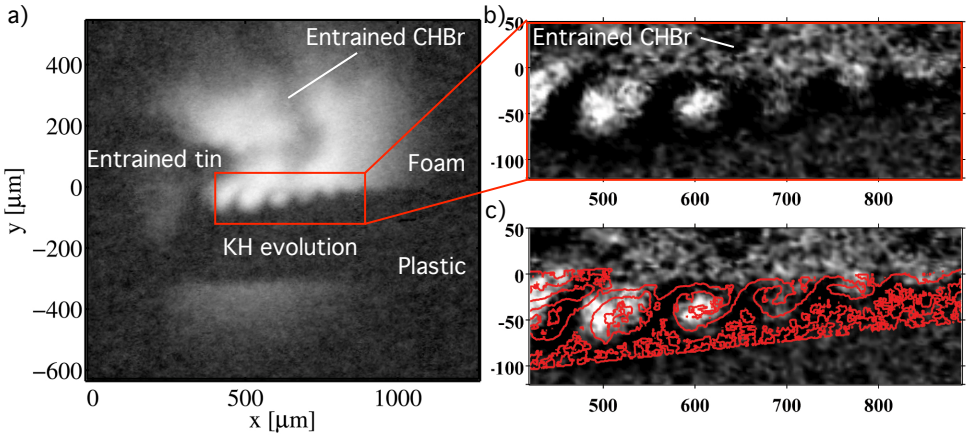

Figure 3.3: Single-mode radiographic data at $t = 65$ ns. (a) Raw radiographic image at $t = 65$ ns. (b) Contrast-enhanced data (c) Interface extracted from the DAFNA simulated radiograph (red lines) overlaid on the processed experimental data.

Fuji^{TM} MS image plate (*Maddox et al.*, 2011). The modulated plastic layer included the tracer strip shown in Figure 3.1, which localized the x-ray opacity in the central portion of the target so that the structure seen in the image is not complicated by effects from the edges of the target along the line of sight. We obtained images from 40 to 65 ns. Figure 3.3a shows an example of the resulting data, in which the growing modulations can be clearly seen.

We processed the radiographic data using an unsharp-mask algorithm (*Di Stefano et al.*, 2014; *Malamud et al.*, 2013b) to obtain the interface location, and analyzed the results to infer several quantities of interest, shown in Table 3.1. We determined the shock location for each radiograph by locating the position where the surface of the plastic was deflected downward, and inferred the shock velocity from these observations at various times. We obtained the compression by fitting the motion of the shock wave and the thermal insulator, and inferred the shear velocity using the basic shock equations. Note also that shock compression causes the spacing of the rollups to be smaller than the initial imposed wavelength (*Malamud et al.*, 2013b). In the table, we also show the same quantities from the simulation of Figure 3.2. The simulation used the actual experimental dimensions and was the result of fine-tuning

the Mach number and the adiabatic index of the foam, in order to match the observed shock timing and interface deflection. We can see that other parameters found by the calibrated simulation match those inferred from the data to within the experimental uncertainties. The calculations for these values are presented in Appendix B.

Parameter	Experiment	Simulation
Shock velocity u_s (μm/ns)	28 ± 2	29
Deflection angle (°)	7.7 ± 1.2	8.3
Foam compression	5.0 ± 1.5	4
Shocked foam pressure (Mbar)	0.63 ± 0.08	0.59
Shear velocity Δu (μm/ns)	22 ± 3	20
Rollup spacing λ (μm)	77 ± 6	80

Table 3.1: Experimentally inferred parameters are compared to their predicted values.

These parameters can be used to estimate the rate at which the system could transition to turbulence. The modulations curl into vortical structures with a characteristic large-eddy timescale for turbulent evolution given as $\tau = \lambda/\Delta u$ (*Frisch*, 1995). Classically, this value is used to approximate the time it takes for a modulation to curl around itself once in an incompressible shear flow with homogeneous turbulence. The parameters listed in Table 3.1 imply that the oldest undisturbed modulations have been allowed to evolve for two to three τ, long enough to have plausibly developed a turbulent interior, despite effects of compressibility and inhomogeneity (*Malamud et al.*, 2013b). Here, we define medium-scale structures to be on the order of 10 to 15 μm, which is at the edge of our diagnostic resolution (*Stoeckl et al.*, 2012). An example of medium-scale structure is the curled tip that arises as a modulation evolves, whereas the peak-to-valley amplitude of the vortices is an example of large-scale structure.

Figure 3.3c compares the results of DAFNA simulations with the data by overplotting the interface location found from a simulated radiograph (including realistic noise) upon the contrast-enhanced data of Figure 3.3b. One would expect the simulations to become less accurate at progressively smaller relative scales. One can see

that the code reproduces the large-scale structures very well, as one would expect. It reproduces the medium-scale structures fairly well, and one cannot readily determine whether the apparent differences reflect a real difference or just experimental uncertainty. One can also infer that differences in small-scale structure between the simulation and the experiment did not in this case affect the large-scale structures significantly. Improvements to the experiment, using the platform demonstrated here, could proceed to explore such scales including the mixing of material into the interior of the rollups.

In order to assess the importance of compressible effects on large-scale behavior, we also performed simulations of pure shear flow. The simulations used the experimental densities and shear velocities. One of them simulated a compressible case, using a pressure (and hence sound speed) taken from the DAFNA simulations so that $M_c = 0.85$ as in the experiment. The other simulated a nearly incompressible case, by using a higher pressure (and hence sound speed), so that $M_c = 0.1$. To interpret the results, it is helpful to recall that single vortices eventually reach a (full) saturated amplitude of 0.56 times their spacing, after which their amplitudes oscillate (*Rikanati et al.*, 2003; *Patnaik et al.*, 1976; *Pozrikidis and Higdon*, 1985). As a result, the impact of a smaller growth rate is to delay the growth but not ultimately to change the saturated amplitude. Figure 3.4 shows a comparison of the data and the simulations using pure shear flow. The abscissa is the dimensionless evolution time appropriate to shear-driven flow, $\Delta u t_s/\lambda$, where t_s is the time since the passage of the shock; i.e., the time for which the KH has been developing. In addition, the period before which the passage of the insulator material alters the dynamics extends to $\Delta u t_s/\lambda \sim 4$, so that data beyond this value may exhibit altered behavior.

Comparisons of the data and the simulations using pure shear flow support the conclusion that compressibility affects KH evolution. Figure 3.4 plots the modulation amplitude from the two simulations against the measured experimental amplitude.

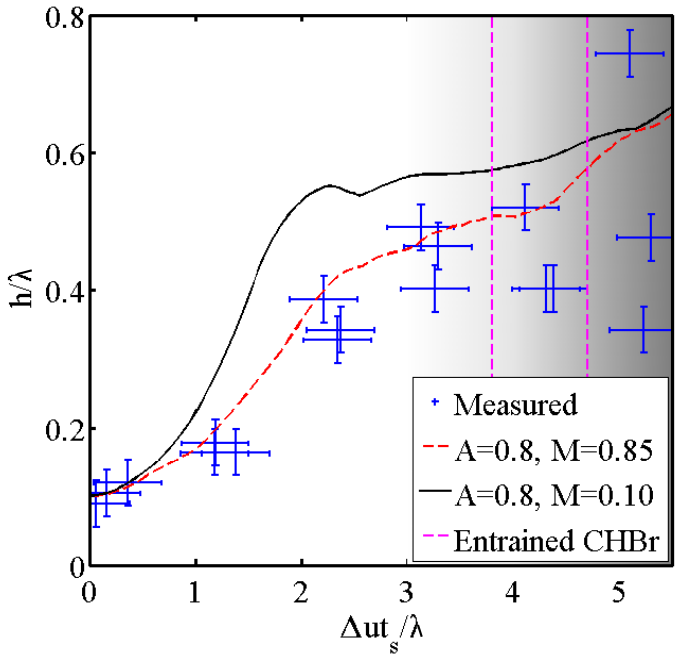

Figure 3.4: Normalized single-mode experimental data fit against theoretical predictions with (dashed red) and without (solid black) significant compression. The dashed magenta lines at $\Delta ut_s/\lambda \sim 4$ represent the location of the CHBr insulator layer, which disturbs the evolving modulations.

To do so, we found the experimental amplitude by rotating the image so that an interface deflected by 7.7 degrees (the measured average) would be horizontal, using the shock front to define $t_s = 0$. The height is calculated as the difference between how far a given central peak of the heavy fluid has penetrated into the lighter fluid, and the average of how far the lighter fluid has penetrated into the heavy fluid on either side of the central peak. The vertical error bars are determined from the resolution limit of the diagnostic. We found the corresponding amplitude from the simulations, with respect to the location of the interface in a simulation without a seed perturbation (*Malamud et al.*, 2013b). One sees that the dashed curve, from the simulation having $M_c = 0.85$, matches the growth of the modulations while the curve from the $M_c = 0.10$ simulation does not. We can see that across all the data, until $\Delta u t_s/\lambda \sim 4$, the amplitude from the simulation of the compressible case is reasonably consistent with the data and that, in contrast, the amplitude from simulation of the incompressible case is not, over most of the relevant period.

3.4 Conclusion

In summary, we have reported the first observations of the evolution of single-mode modulations under the influence of the Kelvin-Helmholtz instability in a supersonic flow. We obtained these data by using a novel experimental system to produce a steady shock wave of unprecedented duration, and using the shocked, flowing material to create a shear layer between two plasmas at high energy density. Our data can be used to benchmark hydrodynamic models or nonlinear theories. Future work can explore multimode behavior and ultimately the transition to turbulence.

Chapter IV

Dual-mode experiment

4.1 Introduction

The KHI has two core components to its behavior: single-vortex evolution, and two-vortex merger. The previous chapter provides the first observations of the first component, single-vortex evolution, from well-characterized single-mode initial conditions in a steady, supersonic flow. In this chapter, we present the first observations from dual-mode initial conditions, which provides the first measurements of KHI vortex merger from a well-defined seed interface, and supplements our measurements of the inhibition of the KHI growth rate in a compressible flow. This manuscript is titled "Observation of dual-mode, Kelvin-Helmholtz instability vortex merger in a compressible flow." It is an invited article that has been published in *Physics of Plasmas* (*Wan et al.*, 2017b).

Two-vortex merger describes the interaction between two vortices. One of the leading approaches for modeling multi-vortex KH evolution is the statistical model first introduced by Rikanati et al. (*Rikanati et al.*, 2003) following the works of Alon et al. (*Alon et al.*, 1994, 1995; *Oron et al.*, 1999; *Shvarts et al.*, 2000; *Oron et al.*, 2001; *Kartoon et al.*, 2003; *Rikanati et al.*, 1998), which yielded new scaling laws in the incompressible limit for the Rayleigh-Taylor (RT) and Richtmyer-Meshkov (RM) instabilities. In these models, small perturbations on the initial interface develop into

an array of bubbles and spikes (in the RT and RM cases) or vortices (in the KH case). The vortex front of hydrodynamically unstable systems is found to be dominated by the growth and competition of vortices, where large vortices evolve faster and overtake their smaller neighbors. The surviving vortices at the front continually grow in an inverse cascade process. This description was first pioneered for the RT case by Sharp and Wheeler (*Sharp*, 1984) and later on extended by Glimm and Sharp (*Glimm and Sharp*, 1990). These statistical models, which are based on single structure evolution and the 2-structure merger process, were verified experimentally for RT and RM in a 2D-RM shock tube experiment (*Sadot et al.*, 1998), 3D-RT laser driven experiment (*Sadot et al.*, 2005; *Smalyuk et al.*, 2009), by the analysis of 3D-RM shock-tube experiments (*Malamud et al.*, 2014), and by the analysis of 2D-KH experiments (*Brown and Roshko*, 1974; *Rikanati et al.*, 2003). The statistical model of Rikanati et al. (*Rikanati et al.*, 2003) was recently extended by Shimony et al. (*Shimony et al.*, 2016a; *Shimony*, 2016; *Shimony et al.*, 2016b) to account for the effect of compressibility and a general density ratio, but KHI vortex-merger is still poorly understood and does not have a simple analytic solution.

The two-vortex experiment followed the same basic setup as the single-vortex experiment described in the previous chapter. This time, however, the seed perturbation is described by the equation: $(0.10\lambda_1)sin(\frac{2\pi}{\lambda_1}x) + (0.05\lambda_2)sin(\frac{2\pi}{\lambda_2}x)$. The chosen wavelengths, discussed below, have a 1:2 wavelength ratio. The data and simulations are once again in good agreement within the diagnostic resolution limit (*Stoeckl et al.*, 2012). The larger vortex, which controls the vortex-merger process, demonstrates an inhibition in its growth rate that is in good agreement with simulations. The consumed vortex demonstrates an extended vortex-merger time, which we will discuss in the next chapter.

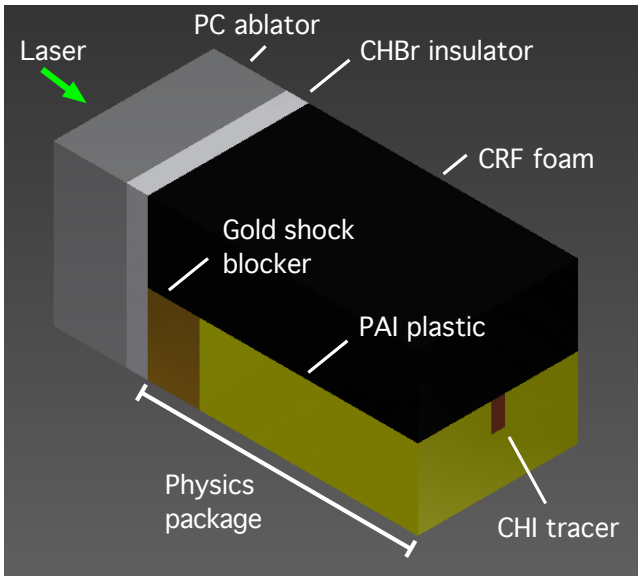

Figure 4.1: Schematic view of the dual-mode target. The lasers are incident upon the PC ablator, and generate a shockwave which propagates in the direction of the CRF foam and PAI plastic. One of several varieties of seeded interfaces, created by superimposing two predetermined sine waves, is machined into the surface of the PAI plastic and CHI tracer.

4.2 Experimental setup

This experiment used the target design described in the previous chapters (as summarized in Fig. 4.1), except that the thickness of the CHBr thermal insulator was further increased from 150 μm (*Wan et al.*, 2017a) to 170 μm due to time and manufacturing constraints from our supplier. Otherwise, the only notable change to the target design was that the seed perturbation was changed to:

$$(0.10\lambda_1)sin(\frac{2\pi}{\lambda_1}x) + (0.05\lambda_2)sin(\frac{2\pi}{\lambda_2}x). \tag{4.1}$$

In the data analyzed here, we utilized dual-mode seed perturbations such that $\lambda_2 = 2\lambda_1$. Two such varieties of initial conditions are discussed: $\lambda_1 = 60$ μm, $\lambda_2 = 120$ μm, which we refer to as 60:120, and $\lambda_1 = 70$ μm, $\lambda_2 = 140$ μm, which we refer to as 70:140. This gives us an initial amplitude of 10.6 μm and 2.2 μm for the larger and smaller modulations respectively in the 60:120 seed perturbation, and an initial

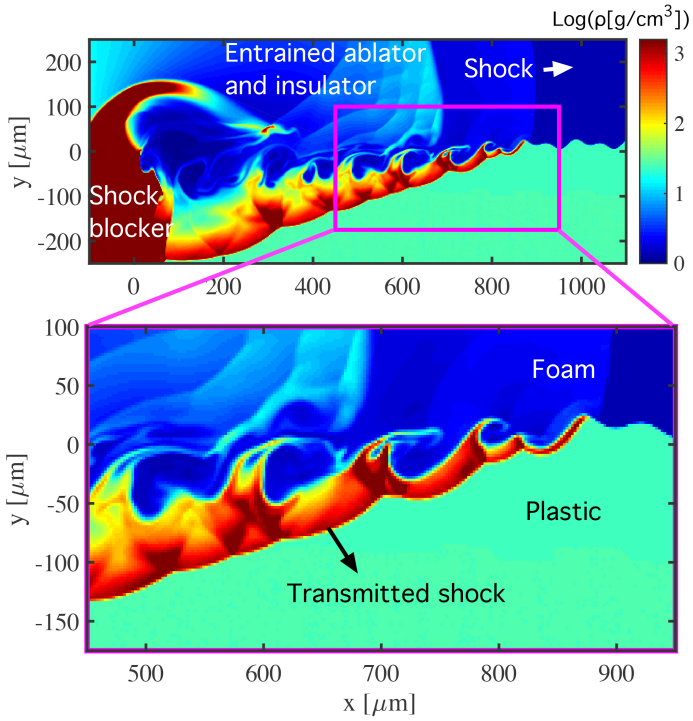

Figure 4.2: 2D DAFNA simulation at $t = 65$ ns, with the 60:120 initial perturbation from Eq. 4.1. The Kelvin-Helmholtz-relevant region is enlarged.

amplitude of 12.3 and 2.6 μm respectively for the 70:140 seed perturbation. These values were chosen such that the features would be large enough to be diagnosed throughout their evolution, yet small enough that multiple modulations could be observed at different stages of evolution and merger within each individual piece of data.

Figure 4.2 shows a 2D density map of a DAFNA simulation 65 ns after the laser has turned on, with a 60:120 seed perturbation. The simulations are described in Chapter II, and the design paper written by Malamud et al. (*Malamud et al.*, 2013b).

Figure 4.2 shows the shock, which moves from left to right. As the shock propagates over the foam-plastic interface, the base of the shock is transmitted downwards into the PAI plastic. Along this deflected interface, the modulations begin to evolve within a steady, supersonic, shear-dominated flow. This process continues until the modulations are disturbed by material from the ablator and insulator, which

have become entrained in the flow. This region, which is downstream of the initial shockwave yet upstream of the entrained ablator and insulator, is referred to as our Kelvin-Helmholtz relevant region. Modulations that are near the shockwave on the upstream edge of the Kelvin-Helmholtz relevant region are in the early stages of their evolution. Modulations near the downstream edge have been evolving for several times their characteristic evolutionary timescale (*Frisch*, 1995), and are in advanced stages of vortex merger.

At this point, it is worth returning to the dispersion relation (Eq. 1.4) to discuss the potential contribution of shallow-fluid effects. Eq. 1.4 is the dispersion relation of the Kelvin-Helmholtz instability for infinitely deep fluids. In a shallow fluid, the dispersion relation is modified into the following form (*Kundu and Cohen*, 2012):

$$\frac{\omega}{k} = \frac{U_1\rho_1 + U_2\rho_2 coth(kD)}{\rho_1 + \rho_2 coth(kD)} \pm \sqrt{\frac{g}{k}\frac{\rho_2 - \rho_1}{\rho_1 + \rho_2 coth(kD)} - \rho_1\rho_2\frac{(U_1 - U_2)^2 coth(kD)}{(\rho_1 + \rho_2 coth(kD))^2}}. \quad (4.2)$$

The inclusion of the hyperbolic cotangent represents the interaction between modulations at the density interface with an impenetrable, motionless boundary at depth D away from the bottom interface (subscript 2). In our experiment, the depth of the plastic is increasing with time. The boundary is thus neither the stationary wall described by Eq. 4.2, nor is it the infinitely deep fluid described by Eq. 1.4. Instead, the dispersion relation is non-trivial, and considered to be in between these two limiting cases.

From Fig. 4.2, we can see that the transmitted shock has penetrated roughly 70 μm into the unshocked plastic by the edge of the KH relevant zone, meaning that $D/\lambda \sim 0.5$ in our experiment. Recalling that the wavenumber, $k = 2\pi/\lambda$, we note that coth(kD) = coth$(2\pi D/\lambda) \sim 1.004$. Shallow-fluid effects are expected to introduce cumulative error of roughly 0.2%, and are thus considered to be negligible.

More complicated shallow-fluid effects might be found in the RM instability. The

RM instability occurs when vorticity is impulsively deposited upon a density interface, and may contribute to the growth of the KH instability as the transmitted shock passes over the perturbed interface and into the PAI plastic. The growth of the RM amplitude is described by (*Mikaelian*, 1994):

$$h(t) = h_o(1 + \Delta v k A t), \tag{4.3}$$

where Δv is the change in the vertical velocity due to an instantaneous acceleration. It is important to note here that the growth rate of the RM instability is linear in time, not exponential. This is because unlike the RT and KH instability, the RM instability does not have an energy source (e.g. gravity) to increase the rate of RM growth. The design of this experiment (*Malamud et al.*, 2013b) allows the exponential growth rate of the KH instability to rapidly overtake the linear growth rate of the RM instability, rendering the contributions of the RM instability to be negligible. Thus, though complex interactions may occur that further inhibit the RM instability in the proximity of a shock (*Glendinning et al.*, 2003), these are considered to be second-order effects that do not significantly impact our results. Future publications by Kuranz et al. and Rasmus et al. will discuss adaptations of this experimental platform (*Malamud et al.*, 2013b) in which the RM and RT instabilities play a significant role in the evolution of the interface.

The final laser beam at the facility is used to generate x-rays for a spherical crystal imager. This beam is incident upon a 1 mm diameter, 20 μm thick copper foil, delivering 850 J of 1053 nm laser light over a 10 ps pulse, focused to a 200 μm spot size. This generates Cu x-rays, which propagate through the target towards a spherically bent crystal. The crystal selectively images the Cu K_α radiation (8.0 keV) at a $\sim$ 10 to 15 μm spatial resolution (*Stoeckl et al.*, 2012), and directs it towards a Fuji^{TM} MS image plate to be recorded. Another research group independently

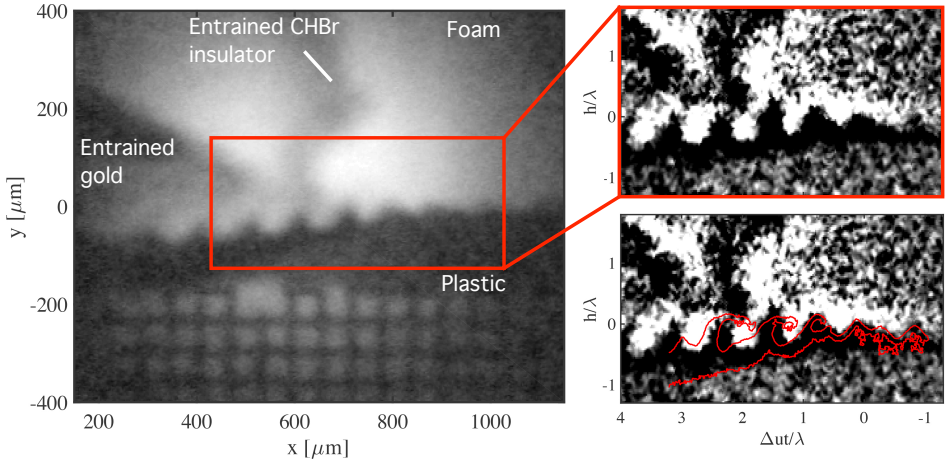

Figure 4.3: Dual-mode radiographic data at $t = 65$ ns. Left: Raw data. Top right: Contrast-enhanced data. Bottom right: Interface extracted from DAFNA simulated radiograph (red lines) overlaid upon the processed experimental data. The data is taken 65 ns after the start of the laser drive, with a 60:120 initial perturbation.

verified this resolution in unpublished data [J.D. Hager, personal communication, 21 May 2014]. Our fiducial grid, however, is located 300 μm outside of the image plane; the resulting spatial resolution of the fiducial grid featured in Fig. 4.3 is ∼20 to 25 μm, which is not indicative of the resolution of the vortices along the density interface. Further analysis of the diagnostic resolution would be beneficial, and will be possible in future experiments.

4.3 Experimental results

Figure 4.3 provides a sample of the data. These data were taken 65 ns after the start of the laser drive, with a 60:120 initial perturbation. The image on the left displays the raw x-ray radiograph. On the upper right, a section of the image has been processed with an contrast-enhancing unsharp mask algorithm (*Malamud et al.*, 2013b; *Wan et al.*, 2015; *Di Stefano et al.*, 2015a), cropped, then rotated such that the deflected interface is horizontal. On the lower right, a contour has been extracted from the 2D DAFNA simulated radiograph, including realistic smearing and noise,

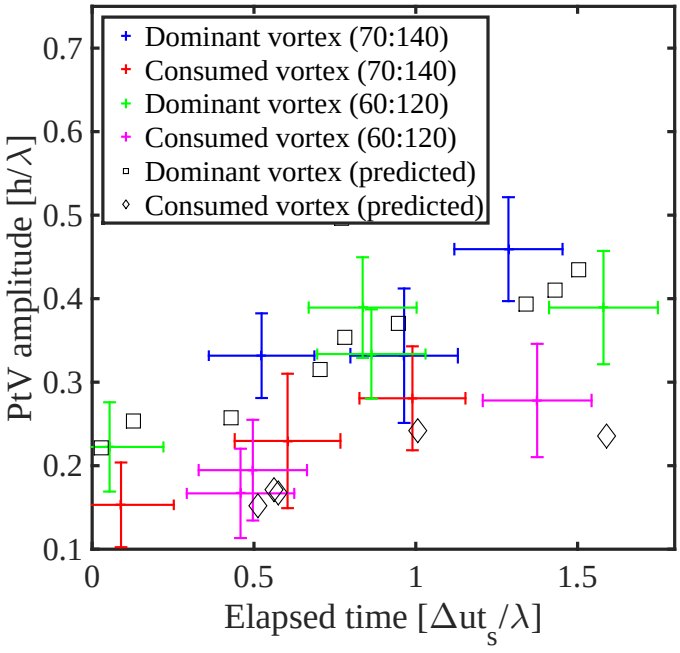

Figure 4.4: Normalized dual-mode experimental data fit against predictions from numerical simulations, with peak-to-valley amplitude on the ordinate and time on the abscissa. The blue and red data points represent the dominant and consumed vortices respectively evolving from a 70:140 initial perturbation. The green and magenta data points represent the dominant and consumed vortices respectively evolving from a 60:120 initial perturbation. The points representing predictions are described in the text.

and overlaid in red upon the data. One can see that the code does a good job of reproducing features above the diagnostic resolution limit of 10-15 μm.

Figure 4.4 plots the normalized peak-to-valley amplitude against the dimensionless evolution time for the numerical simulation predictions and experimental data. The ordinate is normalized by dividing the amplitude measurement by the compressed wavelength of the larger, dominant vortex λ (*Takaki and Kovasznay*, 1978). This value is defined as the averaged rollup spacing for the larger-wavelength vortex, and is consistent with measurements taken from earlier single-mode experiments $\lambda/\lambda_o = (77 \pm 6)/100$ (*Wan et al.*, 2015), where λ_o is the original, unshocked wavelength of the dominant vortex. The abscissa is the dimensionless evolution time, where t_s is

the time since the shock has passed over the modulation.

The black squares represent numerical simulation predictions taken from Fig. 4.2 of the larger, dominant vortex, while the black diamonds represent numerical simulation predictions of the smaller, consumed vortex.

The blue and green experimental data points represent the dominant vortices of the 70:140 and 60:120 initial conditions respectively. The red and magenta data points represent the consumed vortices of the 70:140 and 60:120 initial conditions respectively. These measurements of peak-to-valley amplitude are obtained by rotating the data such that the deflected interface would be horizontal, then taking the difference between how far the central peak of the heavy fluid has penetrated into the lighter fluid, then how far the lighter fluid has penetrated into the heavy fluid on either the downstream side for the dominant modulation, or the upstream side for the consumed modulation. This is in contrast to how the peak-to-valley amplitude was defined in the single-mode experiment, in which the distance the lighter fluid had penetrated into the heavier fluid was taken as the average of both the upstream and downstream values (*Wan et al.*, 2015). This difference in how the peak-to-valley amplitude is defined is to mitigate misleading measurements that result from the gap between the dominant and consumed vortex filling up with the heavier fluid during vortex merger, as seen in Fig. 4.2 and 4.3. Although this method has the potential to overestimate the peak-to-valley amplitude of the dominant modulations and underestimate the peak-to-valley amplitude of the consumed modulations, this error was below the diagnostic resolution limit (*Stoeckl et al.*, 2012), and typically small compared to other sources of uncertainty.

The uncertainty was taken to be the root mean square of a modulation-specific uncertainty and any procedural uncertainties (i.e. $\Delta x = \sqrt{(\Delta x_m)^2 + ((\Delta x_{p1})^2 + (\Delta x_{p2})^2 ... \overline{... + (\Delta x_{pn})^2)}}$, where Δx_m is the uncertainty of the individual measurement, and Δx_{pn} are uncertainties that arise from our techniques). The dominant procedural uncer-

tainty in time, on the abscissa, is derived from a spatial uncertainty of $\Delta x_{p1} = \pm$ 20 μm in locating the shock position, $t_s = 0$, from where the transmitted shock meets the unshocked interface. This was determined from the deflection angle and the uncertainty in zeroing the y-axis to $\pm$ one resolution element, which is of the same order as the initial amplitude of the minor vortex (i.e. $\Delta x_{p1} = 2.6$ μm / $\tan(7.7^\circ \pm 1.2^\circ)$ ~ 20 μm) (*Wan et al.*, 2015).

The dominant procedural uncertainty in the amplitude, on the ordinate, is taken to be $\Delta h_{p1} = \pm 5$ μm, which corresponds to the spatial resolution of our diagnostic (and, in turn, the radius used in our unsharp mask algorithm). The unsharp mask improves acutance without affecting the actual resolution. It does this by adding an overshoot to the start and end of a signal gradient in order to create a sharper gradient in between the overshoot regions (*Di Stefano et al.*, 2015a). This improves the visibility of the interface, without improving or diminishing the quality of the data.

In a compressible flow, the dominant vortex has an inhibited growth rate, and requires more time to reach its full, saturated amplitude. The consumed vortex begins growing at a similar rate, but the vortex merger process begins to dominate before the growth inhibition is distinguishable with our current diagnostic resolution limit. Instead, the consumed vortex ceases to significantly increase in amplitude by $\Delta u t_s/\lambda \sim 0.7$, and then merges completely with the dominant vortex by either $\Delta u t_s/\lambda \sim 1.1$ in the incompressible case, or $\Delta u t_s/\lambda \sim 1.6$ in the compressible case. The experimental data verifies both the anticipated growth inhibition and the prolonged vortex merger time of the compressible simulation. The initial perturbation has no noticeable effect on the normalized results. A future manuscript will explore this topic more thoroughly using simulations of pure, KH evolution in a steady, shear flow.

Figure 4.5 examines the behavior of vortices at the edge of the KH-relevant region.

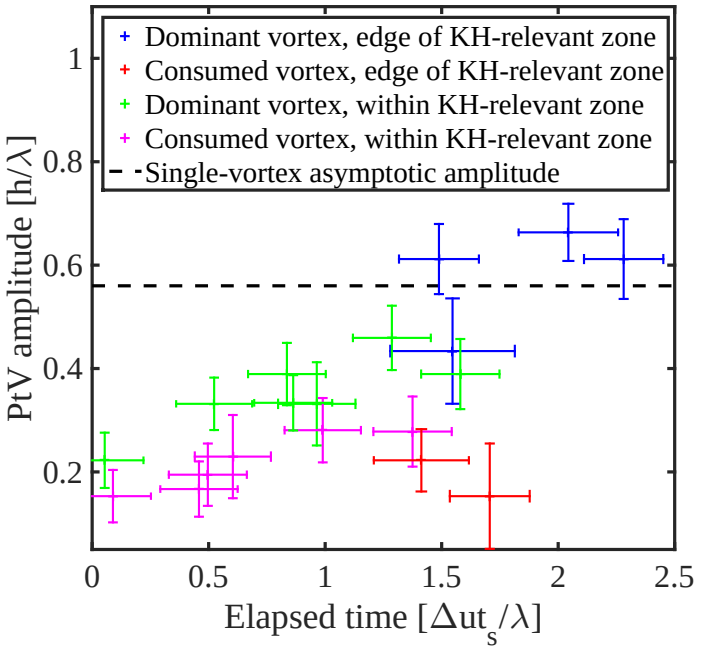

Figure 4.5: Long-term evolution of the peak-to-valley amplitude vs. time. The green and magenta data points are the measurements of the dominant and secondary vortices within the KH-relevant zone, and shown in Fig. 4.4. The blue and red data points are measurements of the dominant and secondary vortices at the downstream edge of the KH-relevant zone.

The green and magenta data points are the previously discussed measurements for the dominant and consumed vortices respectively within the KH-relevant zone, which were shown in Fig. 4.4. The blue and red data points are measurements of the dominant and consumed vortices respectively at the downstream edge of the KH-relevant zone. Entrained material from the passing thermal insulator has begun to disturb the vortices at the edge of the KH-relevant zone. The smaller, consumed vortices are minimally affected by the motion of the thermal insulator. These measurements support the extended vortex merger time expected of a compressible flow.

The dominant vortices are strongly affected by the entrained insulator, and thus may not be well-described by preliminary simulations of pure, KH evolution in a steady, shear flow (*Wan et al.*, 2015). Although these data points are less reliable, they can still contribute to observations of KH vortex merger. Several of these modulations exceed the predicted asymptotic amplitude of single-vortex KH evolution; when two KH vortices merge, they can achieve a new peak-to-valley asymptotic amplitude of $\sim 0.56\ (\lambda_1+\lambda_2)$ (*Rikanati et al.*, 2003). The increased amplitude of the dominant vortex, which coincides with the extinction of the consumed vortex, may be an observation of the secondary surge of growth that follows the merger of two independent vortices.

Figure 4.6 plots the separation distance for each pair of modulations. The separation distance is defined as the difference between the position of the dominant vortex and the position of the consumed vortex, using an averaged value of their dimensionless evolution time. One important distinction that must be made between the experimental measurements and the numerical simulation predictions is that while the predictions define separation distance as the distance between the center of the vortices, the experimental measurements calculate the separation distance from the position of the peaks measured for and defined in Figure 4.4. This value is easier to measure from the experimental data, but will not necessarily capture the small-scale contributions of angular momentum that result in the predicted fluctuations.

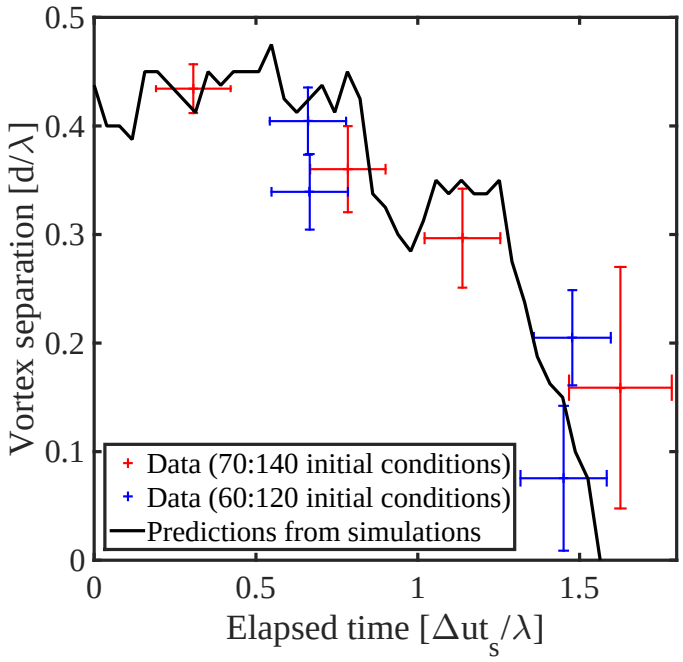

Figure 4.6: Normalized experimental data fit against numerical simulation predictions, with vortex separation distance on the ordinate and time on the abscissa. The red data points evolved from a 70:140 seed perturbation, while the blue data points evolved from a 60:120 seed perturbation. The solid black line is taken from a 2D hydrodynamic simulation performed in DAFNA of the instability evolving in a compressible shear flow.

The red and blue data points represent measurements taken from 70:140 and 60:120 initial conditions respectively. The solid black line represents numerical simulation predictions for the separation distance, taken from 2D DAFNA simulations of the initial perturbations evolving in steady, shear flow. Once again, the ordinate has been normalized with the compressed wavelength λ, while the abscissa represents the dimensionless evolution time. One can see that experimental observations and numerical simulation predictions are in reasonable agreement, and suggest a vortex merger time of $\Delta u t_s/\lambda \sim 1.6$ in a steady, supersonic flow with an Atwood number of A ~ 0.8 and a convective Mach number of $M_c \sim 0.85$.

4.4 Comparison to shear flow simulations, and a discussion of local Mach number effects

In this section, we will compare the data to shear-flow simulations, and we will briefly examine the complex nature of local Mach number effects. These results did not make it into the publication for the dual-mode experiment (*Wan et al.*, 2017b), but can be considered to be an expanded discussion of the data analysis presented earlier in this chapter. The dual-mode data were analyzed against simulations of the KHI evolving in a steady, shear flow, based on the techniques utilized in Chapter III (*Wan et al.*, 2015). The shear flow model is not a perfect representation of the system, as it lacks certain complexities found in the experiment (such as the disruptive effects of the entrained insulator and ablator materials). It does, however, allow us to adjust the pressure and hence sound speed of the materials, to control the convective Mach number of the system without changing the flow velocity (*Shimony*, 2016; *Wan et al.*, 2015). This effectively allows us to create a compressible and an incompressible comparison case.

Fig. 4.7 plots the normalized peak-to-valley amplitude against the dimension-

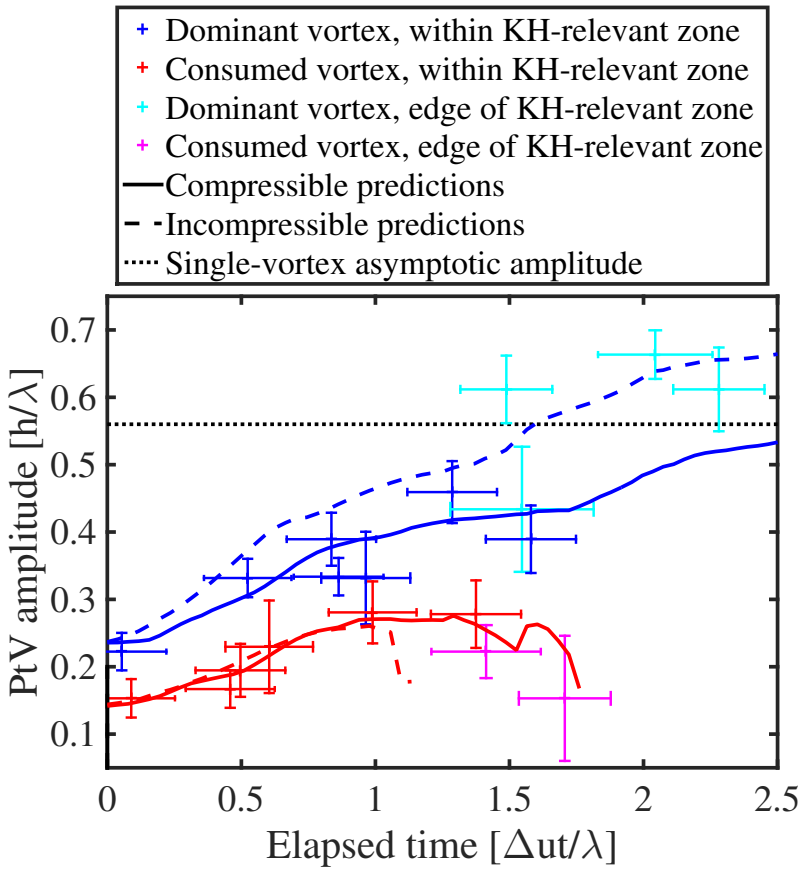

Figure 4.7: Normalized experimental data fit against predictions from a steady, shear flow model with (solid) and without (dashed) significant compression. The blue and red lines represent the dominant and consumed vortices respectively. The blue and red data points are measurements of the dominant and consumed vortices respectively. The cyan and magenta data points are measurements of the dominant and consumed vortices at the edge of the KH-relevant zone.

less evolution time for the theoretical predictions and experimental data, using the same data set as in Fig. 4.5,. The ordinate is normalized by dividing the amplitude measurement by the compressed wavelength of the larger, dominant mode λ (*Takaki and Kovasznay*, 1978). This value is defined as the averaged rollup spacing for the larger-wavelength vortex, and is consistent with measurements taken from earlier single-mode experiments $\lambda/\lambda_o = (77 \pm 6)/100$ (*Wan et al.*, 2015), where λ_o is the original, unshocked wavelength of the dominant mode. The abscissa is the dimensionless evolution time, where t_s is the time since the shock has passed over the modulation.

The solid lines are the theoretical predictions taken from the compressible case of the shear flow simulation (M_c= 0.85), while the dashed lines are the theoretical predictions taken from the nearly incompressible shear flow simulation (M_c= 0.10). The blue lines represent the dominant, larger wavelength vortex, while the red lines represent the secondary, shorter wavelength vortex.

The blue and red data points are the dominant and consumed vortex respectively, for modulations within the KH-relevant zone. The cyan and magenta data points are of the dominant and consumed vortex respectively for modulations at the edge of the KH-relevant zone.

One can see that in the compressible case, the dominant vortex has an inhibited growth rate, and requires more time to reach its full, saturated amplitude. The consumed vortex begins growing at a similar rate, but the vortex merger process begins to dominate before the growth inhibition is distinguishable with our current diagnostic resolution limit. Instead, the consumed vortex ceases to significantly increase in amplitude by $\Delta u t_s/\lambda \sim 0.7$, and then merges completely with the dominant vortex by either $\Delta u t_s/\lambda \sim 1.1$ in the incompressible case, or $\Delta u t_s/\lambda \sim 1.7$ in the compressible case. This is partly due to the complex nature of local Mach number effects.

As we may recall from (§ 1.2.1), the KHI draws kinetic energy out of the main

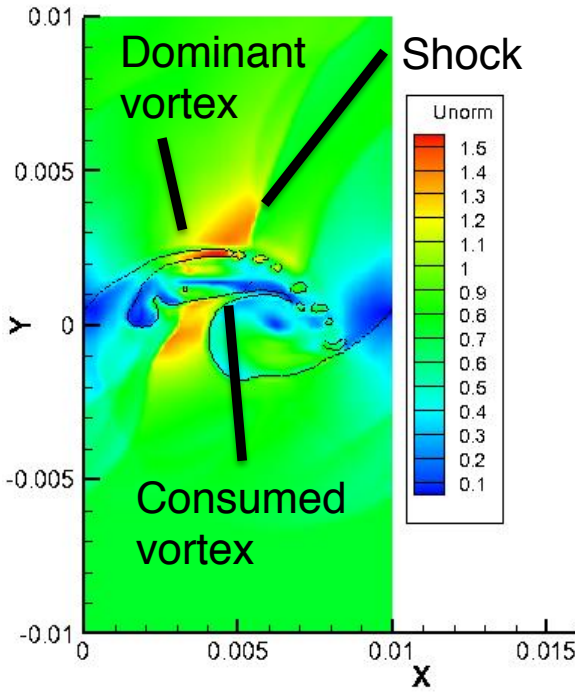

Figure 4.8: Velocity map showing the convective Mach number in a merging vortex-pair. Simulation performed by A. Shimony.

flow through the interaction between the velocity shear and the Reynold's stress (*Kundu and Cohen*, 2000) to feed the growth of the KHI's vortical structures. In a supersonic flow, this effect is very pronounced, and results in inconsistent regions of high or low local Mach numbers (*Shimony*, 2016; *Shimony et al.*, 2016b), as seen in Fig. 4.8. The tips of the consumed vortex consistently have a lower local Mach number than their surroundings, diminishing our ability to resolve an inhibition of the KHI growth rate for the consumed vortex. This system is further complicated by internal shockwaves, which impede the merger process. The full nuances and complexities of the compressible KHI vortex-merger process remain poorly understood and are beyond the scope of this thesis, but the net result is that we will be looking for an extended vortex-merger time instead of a significant inhibition of the growth rate to evaluate the effects of compressibility on the consumed vortex.

The experimental measurements of the dominant vortex agree with the predicted growth inhibition until they are disturbed by the entrained insulator at the edge of

the KH-relevant zone. Measurements of the dominant vortex at the edge of the KH-relevant zone can not be well-described by any of these models. They do, however, exhibit a second surge in growth beyond the single-vortex asymptotic amplitude that coincides with the extinction of the consumed vortex. This may, tenuously, be an observation of the secondary surge in growth that is expected after the merger of two independent vortices (*Rikanati et al.*, 2003).

The consumed vortex is partially sheltered by the dominant vortex, and thus remains undisturbed for a longer period of time. Measurements of the consumed vortex at the edge of the KH-relevant zone continue to support an extended vortex merger time.

4.5 Conclusion

We have presented the first experimental observations of the Kelvin-Helmholtz instability evolving from well-characterized dual-mode initial conditions in a steady, supersonic flow. The results were obtained by using a novel experimental platform to sustain a steady, supersonic shear flow over a precision-machined interface, producing a shear layer between two high-energy-density plasmas. The anticipated vortex merger rates, growth inhibition, and structure were reproduced with 2D hydrodynamic simulations, validating the simulations, and also confirming the theoretical understanding of compressibility effects. This result opens a route to a comprehensive model for compressible KH in the vortex-merger-dominated regime. Future work will explore broadband multimode behavior.

Chapter V

Conclusions and future directions

5.1 Conclusion

In this thesis, I have presented a series of experiments I led. Their purpose was to study the evolution of the Kelvin-Helmholtz instability from precision-machined, well-characterized single-mode and dual-mode seed perturbations in a steady, supersonic, shockwave-driven shear flow. This work is heavily motivated by engineering efforts such as ICF research. The KHI occurs in fusion capsules due to asymmetries in the radiation source and asymmetries along the surface of the fuel capsule. These asymmetries impart a non-radial component to the velocity that gives rise to the KHI. The KHI decreases the available inward kinetic energy and causes unwanted mixing that dilutes the fusion fuel. By studying the KHI, we can increase capability to anticipate, assess, and mitigate its effects in engineering.

Experimental studies into the KHI also further fundamental science. The KHI is commonly observed in all manner of terrestrial and astrophysical systems, including cloud formations, ocean dynamics, atmospheric mixing, and stellar plasmas. These systems are difficult to study through observations due to the uncertain initial conditions, and difficult to study through simulations due to the computationally demanding nature of the many nonlinear components of hydrodynamic instabilities. These KHI experiments provide a higher level of validation for predictions of small-scale

turbulent structures, and may provide improved insight into observations of natural systems.

In order to study the effects of compressibility on the KHI, we needed to establish a new experimental platform. Improvements needed to be made to the initial target design to eliminate the presence of an unanticipated reshock that disturbed the delicate KHI structures. I diagnosed and addressed these issues through the use of 1D simulations. The initial experiment also revealed that the carbon foam we used has a complicated EOS that is not well-described by assuming an adiabatic index of 5/3.

The single-mode experiment successfully produced the first measurements of a single-mode seed perturbation evolving in a steady, supersonic flow. Once the simulations were re-calibrated so as to accurately reproduce the large-scale hydrodynamics, good agreement was achieved between data and simulations. The data support an inhibition of the instability's growth rate due to effects of compressibility.

The dual-mode experiment successfully produced the first measurements of the KHI vortex-merger rate from well-characterized seed perturbations. These results demonstrate an inhibition of the vortex merger rate, and supplement our measurements of the ithe instability's reduced growth rate under supersonic conditions. The data and simulations are in good agreement until the evolution of the modulations is disturbed, as anticipated.

The data obtained from these single-mode and dual-mode experiments is an essential first step in developing a comprehensive model for the evolution of the compressible KHI in a regime dominated by vortex merger.

5.2 Future work

Hydrodynamic instabilities are already difficult to study computationally and analytically due to their highly nonlinear nature. Additional effects, such as those found in a compressible flow, quickly make the problem intractable. As such, it would be

a worthwhile goal for future students to continue studying the compressible case of the KHI once diagnostic resolution and machining precision have improved, in order to determine whether good agreement can still be found for small-scale features. The vortex-merger process has been particularly difficult to analyze and, despite the results of this thesis, remains poorly-understood.

The experimental platform could be significantly improved by increasing the size of the Kelvin-Helmholtz relevant zone. This would allow us to observe the modulations further into their evolutionary process, and thus allow us to study late-time structure and the transition to turbulence. The easiest way to achieve this is to extend the duration of the laser pulse, such that it maintains drive pressure for a longer duration. With some development, the OMEGA-EP facility could theoretically add these capabilities. The indirect-drive technique that's currently being designed for the NIF might also be able to achieve these conditions (*Capelli et al.*, 2016).

Adaptations of this experiment have recently been performed with different initial interfaces, and will be presented in future manuscripts. Among these campaigns was an experiment by Kuranz et. al that measured KHI growth from broadband, multi-mode initial conditions, which can be used to validate a statistical model (*Shimony*, 2016; *Shimony et al.*, 2016b) developed from the single-vortex growth and two-vortex-merger measurements produced from the experiments (*Wan et al.*, 2015, 2017b) presented in this dissertation. Other experiments by Kuranz et. al and Rasmus et. al changed the angle of the foam-plastic interface, in order to study the interaction between the KHI, RTI, and RMI.

Future experiments can repeat this work at different Mach numbers. The flow velocity has a weak relationship to the laser intensity, so a comparable system with a different Mach number cannot be easily achieved merely by adjusting the intensity of the laser. Instead, a method must be developed to change the speed of sound of the medium. An equivalent flow velocity in a higher temperature medium would

allow us to compare the effects of compressibility at different Mach numbers. Unfortunately, existing techniques for pre-heating the medium risks deformation of the seed perturbation.

If a technique can not be developed to significantly vary the Mach number in a laser-driven experiment, then an incompressible comparison case can be pursued with a shock-tube, wind tunnel, or tilt table experiment. To do this, a technique would need to be devised to seed a well-controlled perturbation along the interface, and care must be taken to produce an experiment with a similar Atwood number and Reynolds number in order to compare the data.

The compressible KHI could also be studied in a magnetic field, though we do not currently have the technological capability to impose a strong enough magnetic field, or to reliably diagnose the weak self-generated magnetic fields that may exist in such a system (studying these effects would require the development of a new diagnostic that could produce quantitative measurements at 10-15 μm resolution or better without interfering with the evolution of the system). The presence of a strong magnetic field can contribute to the stabilization or destabilization of the linear phase of the KHI, depending on the structure of the magnetic field (*Sharma and Srivastava*, 1968; *Keppens et al.*, 1999). These ideas can be pursued in the future once more advanced experimental techniques have been developed.

Obtaining these data was the first step towards producing a comprehensive statistical model for broadband, multi-vortex KHI evolution in a compressible flow. Additional experiments, paired with further theoretical analysis and improved diagnostic capabilities, will improve our ability to simulate fine-scale hydrodynamic instability structure and the transition to turbulence, better predict and model hydrodynamic instabilities in nature (e.g. at magnetospheric boundaries (§ 1.4.2), and help us develop techniques to mitigate their contributions to engineering systems (e.g. in ICF experiments (§ 1.4.1).

APPENDICES

APPENDIX A

The Rayleigh-Taylor instability (RTI) and Richtmyer-Meshkov instability (RMI)

In this appendix, we provide an overview of the Rayleigh-Taylor instability (RTI) and Richtmyer-Meshkov instability (RMI). The RTI and RMI arise when the direction of motion is perpendicular to a density interface, and are common in many of the systems that motivate our research into the KHI (*Freeman et al.*, 1977; *Ebisuzaki et al.*, 1989; *Oron et al.*, 1999; *Smalyuk*, 2012). The RMI and RTI have complicated interactions with the KHI (*Mikaelian*, 1994) that will be explored in future manuscripts by Kuranz et al. and Rasmus et al.

A.1 The Rayleigh-Taylor instability (RTI)

The Rayleigh-Taylor instability (RTI) (*Rayleigh*, 1882; *Taylor*, 1950a) is perhaps the most intuitive of the hydrodynamic instabilities. The RTI is driven by buoyancy, and occurs when a heavy fluid is accelerated against a lighter fluid. To picture this, one might consider a soap dispenser that has been topped off with a heavier soap, as seen in Fig. A.1. In this example, gravity provides a downward acceleration. Since this is a hydrodynamically unstable interface, any perturbation along the interface

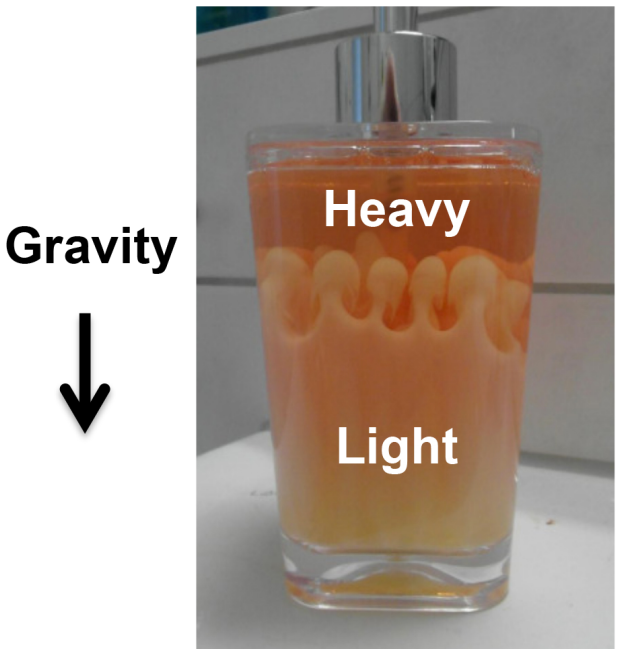

Figure A.1: Photo of Rayleigh-Taylor instability (RTI) structure in a soap dispenser. A soap dispenser has been refilled with a heavier soap. The heavier soap is in the process of settling to the bottom of the dispenser. RTI structures can be seen along the interface. Image adapted from a photo uploaded to Reddit by Thermoskanne.

will rapidly grow. Whereas the KHI results in the formation of vortical structures that resemble ocean waves breaking along a shallow beach, the RTI results in fingers of the heavier fluid penetrating into the lighter fluid, while bubbles of the lighter fluid rise to the top. If left undisturbed, the instability will allow the system of fluids to rearrange itself into a more stable state, with the heavier fluid eventually settling to the bottom.

From section § 1.2.2, Eq. 1.1, we recall that the Euler equations are given as:

$$\frac{\partial \rho}{\partial t} + \nabla \cdot \rho u = 0 \qquad \text{Continuity equation} \qquad \text{(A.1a)}$$

$$\rho(\frac{\partial u}{\partial t} + u \cdot \nabla u) = -\nabla p \qquad \text{Momentum equation} \qquad \text{(A.1b)}$$

$$\frac{\partial \rho}{\partial t} + u \cdot \nabla p = -\gamma p \nabla \cdot u \qquad \text{Energy equation} \qquad \text{(A.1c)}$$

The growth rate of the RTI is derived by linearizing and combining these flow

equations (*Chandrasekhar*, 1961; *Drake*, 2006; *Kundu and Cohen*, 2000), and results in exponential growth of small-amplitude perturbations,

$$h(t) = h_o e^{i(kx-\omega_r t)+\gamma t}. \tag{A.2}$$

Earlier, this method was used to obtain the dispersion relation featured in Eq. 1.4, which states:

$$\frac{\omega}{k} = \frac{U_2\rho_2 + U_1\rho_1}{\rho_2 + \rho_1} \pm \sqrt{\frac{g}{k}\frac{\rho_2 - \rho_1}{\rho_2 + \rho_1} - \rho_1\rho_2\frac{(U_1 - U_2)^2}{(\rho_2 + \rho_1)^2}}. \tag{A.3}$$

We can simplify this equation to obtain the two classic cases of both the KHI and the RTI. The simplest case of the KHI can be obtained by assuming the acceleration of the interface is negligible ($g = 0$), and results in Eq. 1.6 (discussed in § 1.2.2). The simplest case of the RTI can be obtained by assuming that the shear velocity is zero ($\Delta U = 0$), which gives us the following dispersion relation:

$$\frac{\omega}{k} = \pm\sqrt{\frac{g}{k}\frac{\rho_2 - \rho_1}{\rho_2 + \rho_1}}. \tag{A.4}$$

Recalling that the growth rate coefficient is obtained from the imaginary component of ω, such that $\gamma = -i\omega_i$, we can determine the growth rate coefficient to be:

$$\gamma = \sqrt{gk(\frac{\rho_2 - \rho_1}{\rho_2 + \rho_1})} = \sqrt{gkA}, \tag{A.5}$$

where the A is the Atwood number, defined as $A = (\rho_2 - \rho_1)/(\rho_2 + \rho_1)$.

We can consider the three elements of this dispersion relation. When the acceleration g, is increased, then the force acting upon the fluids is stronger, and the structures are able to grow more rapidly. The wavenumber, k, is inversely proportional to the size of the modulation. Based on the conservation of momentum, it takes more energy to accelerate large amounts of mass, so the instability grows more slowly

for modulations with a large wavelength (and thus, small k). The Atwood number, A, is a dimensionless expression of the density ratio. When the two fluids have very different densities ($A \to 1$), then the lighter fluid provides very little resistance, and the structures can grow relatively unimpeded. When the two fluids have the same densities ($A \to 0$), then the system is stable, the growth rate is zero, and modulations do not grow under the influence of the RTI. In the case that $\rho_2 > \rho_1$ (the heavier fluid is already resting on the bottom), then this mechanism helps keep the system stable (e.g. gravity keeps the heavier fluid on the bottom).

A.2 The Richtmyer-Meshkov instability (RMI)

Of the KHI, RTI, and RMI, the RMI is the most difficult to derive analytically, and generally the most poorly understood. The Richtmyer-Meshkov instability (RMI) (*Richtmyer*, 1960; *Meshkov*, 1969) was originally thought to be an impulsive limit to the RTI. To this end, the growth rate of the instability is often derived by using a Dirac delta function in the acceleration, and integrating over an infinitesimal time interval (*Mikaelian*, 1994; *Brouillette*, 2002). Unlike the RTI, however, the RMI can occur regardless of whether the heavier fluid is accelerated lighter fluid, or whether the lighter fluid is accelerated against the heavier fluid. Perhaps most importantly, the RMI is not considered to be a true hydrodynamic instability, as it lacks an energy source to create a feedback mechanism to support continued growth.

Whereas the KHI and RTI have exponential growth rates, the growth rate of the RMI is linear, and can be given as:

$$h(t) = h_o(1 + \Delta v k A t). \tag{A.6}$$

In this equation, Δv is the change in the vertical velocity due to an instantaneous acceleration. One can see that like the RTI, the RMI requires that the two fluids

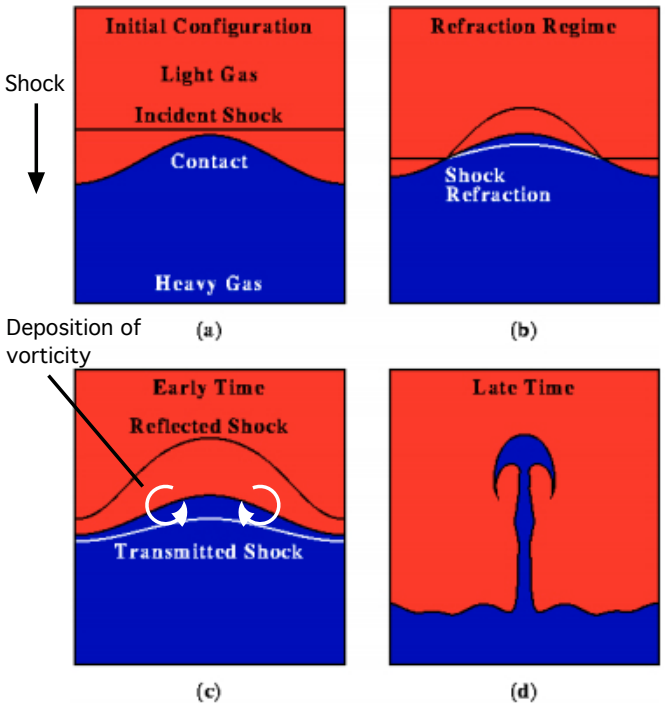

Figure A.2: Schematic of the Richtmyer-Meshkov instability (RMI) evolving along a shocked interface. (a) A shock approaches a non-planar interface. (b) The shock has partially entered the perturbed interface, resulting in a forward-propagating transmitted shock, and a backwards propagating reflected shock. The shock is subject to a localized change in velocity. (c) The deposition of vorticity causes the perturbation to grow. (d) Late time RMI structure. Figure adapted from J. Grove, *Los Alamos National Laboratory Report LA-UR 99-3985*, 1999.

have different densities, even if the direction (heavy to light vs. light to heavy) is irrelevant. To understand why this is important, we can consider a planar, impulsive acceleration (e.g. a shockwave) passing over a non-planar interface (e.g. a sinusoidal seed perturbation). This system can be seen in Fig. A.2 (*Grove*, 1999). As the shockwave crosses into the perturbed interface, the shockwave will temporarily exist in multiple mediums at the same time. The difference in densities at the interface results in differences in local velocity, which introduces torque and vorticity along the interface. This vorticity remains even after the shock has passed, and can result in the growth of spike and bubble structures, reminiscent of the RTI.

APPENDIX B

Key calculations

This appendix covers key calculations that went into the results presented in Table 3.1 of Chapter III. These calculations show how we calculated the foam compression, shocked foam pressure, and shear velocity.

B.1 Foam compression

The foam compression was calculated with a 1D estimate, where $\rho_{initial}/\rho_{compressed} \approx x_{shock}/x_{KH-relevant}$. In other words, we calculated the compression of the foam as the distance the shock has propagated into the foam divided by the KH relevant zone (the size of the compressed foam along the shock propagation axis). This was our largest source of uncertainty in subsequent calculations, and fails to take into account 3D effects such as the curvature of the shock. Our estimate suggests a foam compression of $\sim 5.0 \pm 1.5$.

B.2 Shocked foam pressure

The foam pressure can be estimated using the estimated foam compression, the measured shock velocity, and the Rankine-Hugoniot conditions.

B.2.1 Rankine-Hugoniot equation for the conservation of mass (lab frame)

$\rho_1 u_s = \rho_2(u_s - u_2)$

$u_2 = u_s(\frac{\rho_2-\rho_1}{\rho_2}) = u_s(1 - \frac{\rho_1}{\rho_2})$

$u_s = u_2(\frac{\rho_2}{\rho_2-\rho_1})$

B.2.2 Measured quantities

Foam calculations in the lab frame.

$u_s = 28\pm\ 2\ \mu$m/ns — shock velocity

$\rho_1 = 0.10\pm\ 0.00$ g/cm^3 — unshocked foam density

$\rho_2 = 0.50\pm\ 0.15$ g/cm^3 — shocked foam density

$u_2 = (28\pm\ 2\ \mu\text{m/ns})\ *\ (1 - \frac{1}{5.0\pm1.5}) = 22.4 \pm 1.7\ \mu$m/ns

$p_1 \sim 0$ Mbar... assume negligible initial pressure ($p_2 \gg p_1$)

B.2.3 Rankine-Hugoniot equation for the conservation of momentum

$p_2 - p_1 = \rho_1 u_s u_2$

$p_2 - p_1 = \rho_1 u_s^2(\frac{\rho_2-\rho_1}{\rho_2})$

$p_2 - p_1 = u_2^2(\frac{\rho_1\rho_2}{\rho_2-\rho_1})$

$p_2 = 0.63\pm\ 0.08$ Mbar

B.3 Shear velocity

The shear velocity is the most complicated calculation, and requires us to first calculate the velocity of the shocked foam and the shocked plastic from measurable quantities (such as the foam compression and the shock velocity). Multiple vectors are defined and multiple coordinate transformations are performed, as shown in Fig. B.1. Subscript **(a)** denotes the shocked foam, subscript **(b)** denotes the unshocked foam, subscript **(c)** denotes the unshocked plastic, and subscript **(d)** denotes the shocked

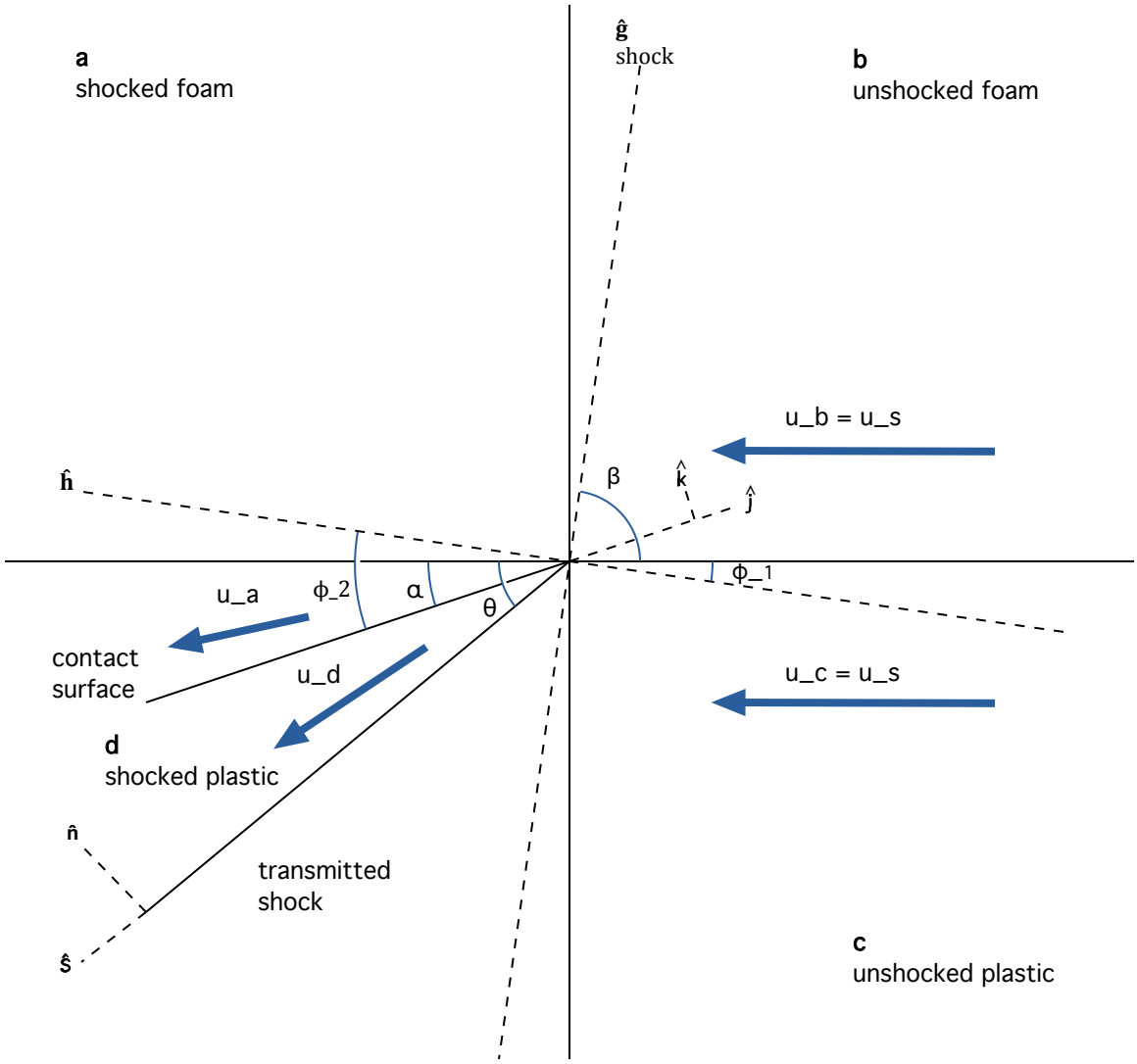

Figure B.1: Vector diagram for the velocity shear calculation. Subscript **(a)** denotes the shocked foam, subscript **(b)** denotes the unshocked foam, subscript **(c)** denotes the unshocked plastic, and subscript **(d)** denotes the shocked plastic.

plastic. The "contact surface" refers to the interface between the shocked foam and unshocked plastic.

B.4 Foam velocity

B.4.1 Oblique shock relations

$\rho_a u_{an} = \rho_b u_{bn}$

$u_{a\perp} = u_{b\perp}$

$tan(\phi_2) = \frac{u_{a\perp}}{u_n} = \frac{u_{b\perp}}{u_{bn}} \frac{\rho_a}{\rho_b} = \frac{\rho_a}{\rho_b} tan(\phi_1)$

B.4.2 Measured quantities

u_s = -(28 $\pm$ 2 μm/ns) $\hat{x}$ + 0 $\hat{y}$	shock velocity
$\frac{\rho_a}{\rho_b} = (5.0 \pm 1.5)$	foam compression
$\alpha = 8 \pm 2^\circ$	interface deflection angle

B.4.3 Calculations

$tan(\alpha + \phi_1) = \frac{\rho_a}{\rho_b} tan(\phi_1)$

$tan[\alpha + (90 - \beta)] = \frac{\rho_a}{\rho_b} tan[(90 - \beta)]$

$\beta = (88.0 \pm 1.3^\circ), \phi_1 = (2.0 \pm 1.3^\circ)$

B.4.4 Coordinate transform

$\hat{g} = cos(\beta)\hat{x} + sin(\beta)\hat{y}$

$\hat{h} = -sin(\beta)\hat{x} + cos(\beta)\hat{y}$

$u_a \cdot \hat{g} = u_b \cdot \hat{g} = u_s cos(\beta) = -(1.0 \pm 0.6)\mu m/ns$

$u_b \cdot \hat{h} = -u_s sin(\beta) = (28.0 \pm 2.0)\mu m/ns$

$u_a \cdot \hat{h} = \frac{\rho_b}{\rho_a} u_b \cdot \hat{h} = (5.6 \pm 1.7)\mu m/ns$

B.4.5 Lab coordinates

$u_b \cdot \hat{x} = -(28 \pm 2)\mu m/ns$

$u_b \cdot \hat{y} = -(0)\mu m/ns$

$u_a \cdot \hat{x} = -(5.6 \pm 1.7)\mu m/ns$

$u_a \cdot \hat{y} = -(0.8 \pm 0.6)\mu m/ns$

B.5 Plastic velocity

B.5.1 Measured quantities

$u_c = u_b = (28 \pm 2)\hat{x} + 0\hat{y}$

B.5.2 Coordinate transform

$u_d \cdot \hat{x} = u_d cos(\alpha)$

$u_d \cdot \hat{y} = u_d sin(\alpha)$

$\hat{n} = -sin(\theta)\hat{x} + cos(\theta)\hat{y}$

$\hat{s} = -cos(\theta)\hat{x} - sin(\theta)\hat{y}$

B.5.3 Calculations

$u_c \cdot \hat{s} = -(u_c \cdot \hat{x})cos(\theta)$

$u_d \cdot \hat{s} = u_d[-cos(\alpha)cos(\theta) - sin(\alpha)sin(\theta)]$

$u_d \cdot \hat{n} = \frac{\rho_c}{\rho_d}(u_c \cdot \hat{x})sin(\theta)$

$u_d \cdot \hat{n} = u_d[-cos(\alpha)sin(\theta) + sin(\alpha)cos(\theta)]$

$u_s \cdot \hat{x} = u_d[\frac{-cos(\alpha)cos(\theta) - sin(\alpha)sin(\theta)}{-cos(\theta)}]$

$u_s \cdot \hat{x} = u_d(\frac{\rho_d}{\rho_c})[\frac{-cos(\alpha)sin(\theta) + sin(\alpha)cos(\theta)}{-sin(\theta)}]$

$\theta = 10.7 \pm 2.7^\circ$

$u_d = -27.5 \pm 2.0\mu m/ns$

$u_d \cdot \hat{x} = u_d cos(\alpha) = -27.3 \pm 2.0\mu m/ns$

$$u_d \cdot \hat{y} = u_d sin(\alpha) = -3.8 \pm 1.0 \mu m/s$$

B.6 Shear velocity

B.6.1 Calculated values

$$u_a = (-5.6 \pm 1.7)\hat{x} + (-0.8 \pm 0.6)\hat{y}$$

$$u_b = u_c = (-28 \pm 2)\hat{x} + 0\hat{y}$$

$$u_d = (-27.1 \pm 2.0)\hat{x} + (-3.8 \pm 1.0)\hat{y}$$

B.6.2 Coordinate transformation

$$\hat{j} = cos(\alpha)\hat{x} + sin(\alpha)\hat{y}$$

$$\hat{k} = -sin(\alpha)\hat{x} + cos(\alpha)\hat{y}$$

$$u_n \cdot \hat{j} = (u_n \cdot \hat{x})cos(\alpha) + (u_n \cdot \hat{y})sin(\alpha)$$

$$u_n \cdot \hat{k} = (u_n \cdot \hat{x})(-sin(\alpha)) + (u_n \cdot \hat{y})cos(\alpha)$$

$$u_a = (-5.7 \pm 1.7)\hat{j} + (0.0 \pm 0.7)\hat{k}$$

$$u_b = u_c = (-27.7 \pm 2.0)\hat{j} + (3.9 \pm 1.0)\hat{k}$$

B.6.3 Foam velocity, lab frame

$$u_a \cdot \hat{j} - u_b \cdot \hat{j} = 22.0 \pm 2.6 \mu m/ns$$

B.6.4 Shear velocity

$$\Delta u = u_a \cdot \hat{j} - u_d \cdot \hat{j} = 21.9 \pm 2.6 \mu m/ns$$

APPENDIX C

Target development data

In this appendix, I present the x-ray radiographic images obtained from the first experiment, discussed in Chapter II. The behavior of the shockwave and ablator was inconsistent throughout this experiment, due to the presence of an unanticipated reshock (*Wan et al.*, 2017a). The foam was also determined to reach a higher compression than what was predicted from simulations. This experiment had a 19 ns laser drive, with a 185 μm thick ablator, detailed in Chapter II. The seed perturbation is described by the equation: $0.05\lambda\ sin(\frac{2\pi}{\lambda}x)$, where λ is either 50 μm or 100 μm. One target was also fielded with a nominally flat interface.

Also included is a table containing the facility's shot number for each piece of data, the shot request form (SRF) RID number (which can be used to look up the experimental setup and data for each shot), the time (after the start of the first laser) at which the radiographic image was taken, measurements of the thickness of the PC ablator, CHBr insulator, and high-Z block in the direction of the flow, and the total laser energy delivered to the target.

Table C.1: Shot log for the first experiment (platform development).

Shot number	Facility shot number	SRF RID	Time [ns]	PC width [μm]	CHBr width [μm]	Au width [μm]	Total energy [kJ]
1	15947	44172	35	185	101	353	8.77
2	15948	45105	35	183	103	349	8.53
3	15950	45125	35	177	107	354	8.53
4	15952	45126	35	186	112	348	8.98
5	15953	45127	35	174	108	362	8.97
6	15956	45128	40	183	103	364	8.97
7	15957	45129	40	173	117	349	8.73

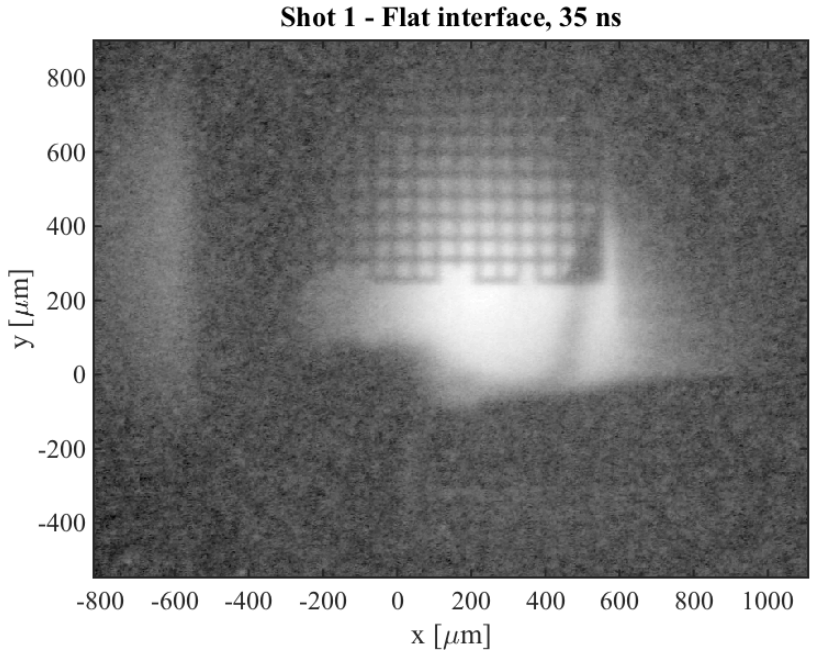

Figure C.1: Experiment 1, shot 1. x-ray radiograph taken at $t = 35$ ns with a flat initial interface. Backlighter at half energy. The blast shield (filter) in front of the image plate consisted of 50 μm of aluminized mylar.

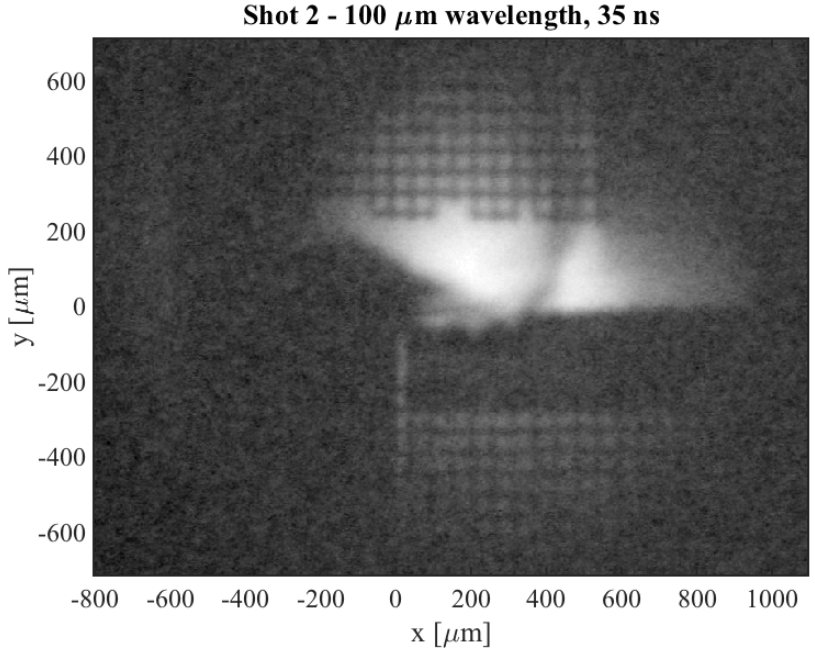

Figure C.2: [Experiment 1, shot 2. x-ray radiograph taken at $t = 35$ ns with a 100 μm wavelength seed perturbation. The blast shield (filter) in front of the image plate consisted of 50 μm of aluminized mylar.

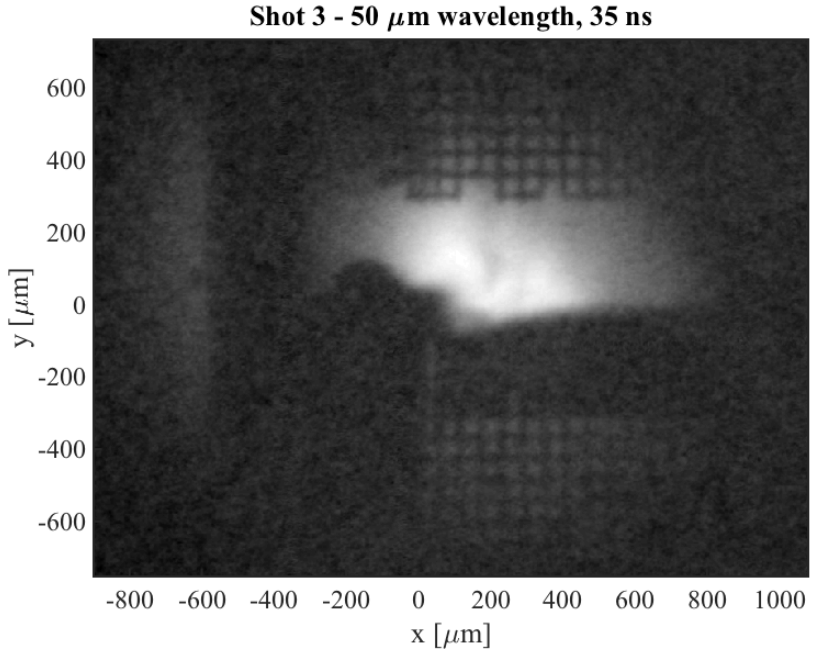

Figure C.3: Experiment 1, shot 3. x-ray radiograph taken at $t = 35$ ns with a 50 μm wavelength seed perturbation. The blast shield (filter) in front of the image plate consisted of 50 μm of aluminized mylar.

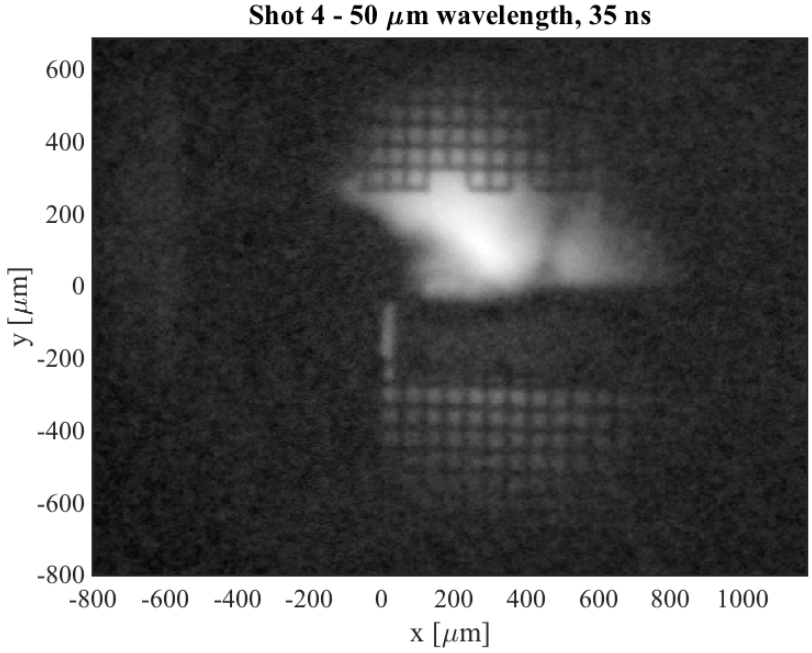

Figure C.4: Experiment 1, shot 4. x-ray radiograph taken at $t = 35$ ns with a 50 μm wavelength seed perturbation. The blast shield (filter) in front of the image plate consisted of 50 μm of aluminized mylar.

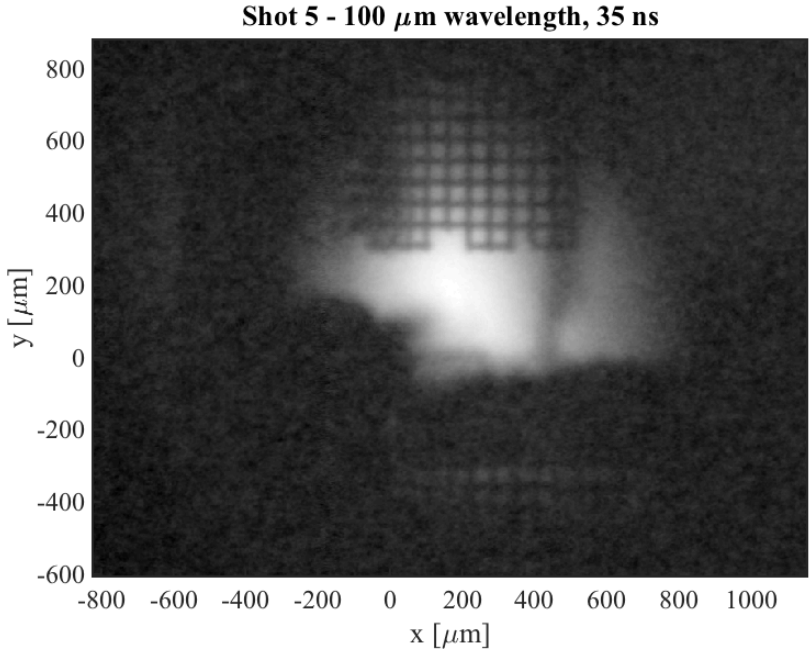

Figure C.5: Experiment 1, shot 5. x-ray radiograph taken at $t = 35$ ns with a 100 μm wavelength seed perturbation. The blast shield (filter) in front of the image plate consisted of 50 μm of aluminized mylar.

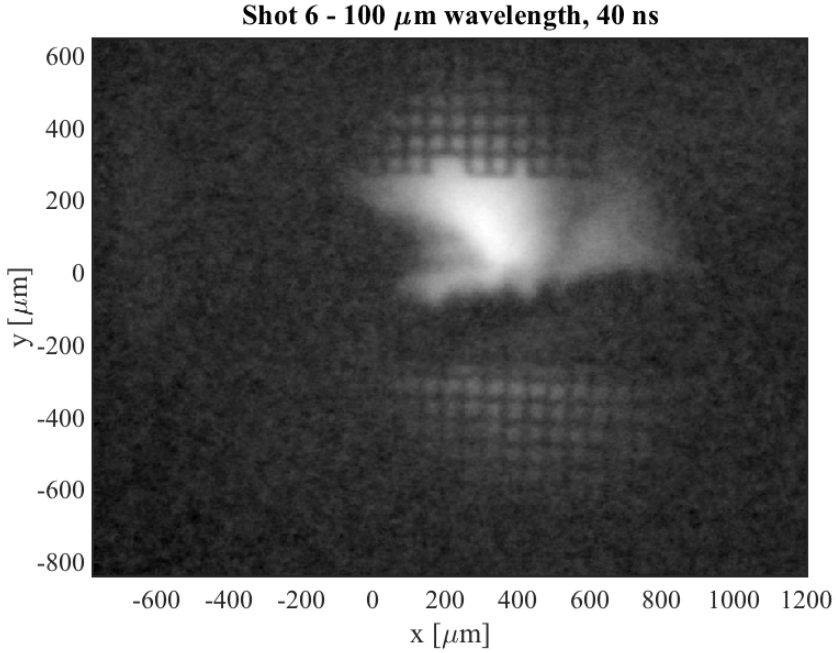

Figure C.6: Experiment 1, shot 6. x-ray radiograph taken at $t = 40$ ns with a 100 μm wavelength seed perturbation. The blast shield (filter) in front of the image plate consisted of 50 μm of aluminized mylar.

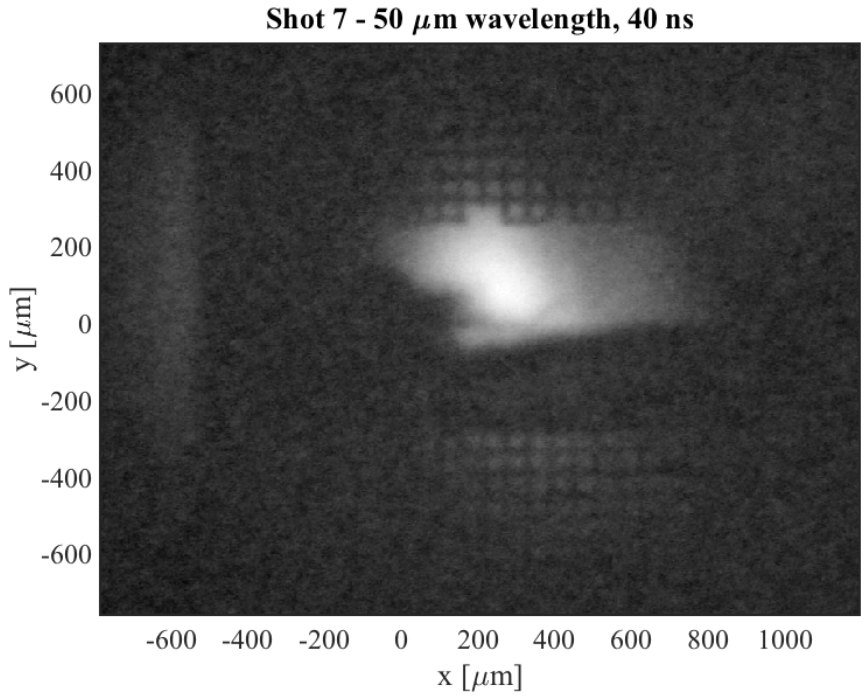

Figure C.7: Experiment 1, shot 7. x-ray radiograph taken at $t = 40$ ns with a 50 μm wavelength seed perturbation. The blast shield (filter) in front of the image plate consisted of 50 μm of aluminized mylar.

APPENDIX D

Single-mode data

In this appendix, I present the x-ray radiographic images obtained from the single-mode experiment, discussed in Chapter III. The quality and consistency of the data was significantly improved (*Wan et al.*, 2015) by increasing the laser drive duration and the ablator thickness (*Wan et al.*, 2017a; *Malamud et al.*, 2013b). We successfully produced the first observations of the KHI evolving from single-mode initial conditions in a steady, supersonic flow. This was achieved, in part, by extending the laser drive duration to 28 ns and increasing the ablator thickness to 500 μm, as detailed in Chapter III. In this data, all modulations evolved from a 100 μm wavelength, 5 μm amplitude sinusoidal seed perturbation, as discussed in Chapter III.

Also included is a table containing the facility's shot number for each piece of data, the shot request form (SRF) RID number (which can be used to look up the experimental setup and data for each shot), the time (after the start of the first laser) at which the radiographic image was taken, measurements of the thickness of the PC ablator, CHBr insulator, and high-Z block in the direction of the flow, and the total laser energy delivered to the target.

Table D.1: Shot log for the second experiment (single-mode).

Shot number	Facility shot number	SRF RID	Time [ns]	PC width [μm]	CHBr width [μm]	Au width [μm]	Total energy [kJ]
1	17399	46650	45	510	138	359	11.15
2	17400	47209	45	509	128	359	11.85
3	17401	47210	50	511	156	342	12.34
4	17402	47211	40	508	147	349	12.52
5	17403	47218	60	510	130	367	12.65
6	17405	47220	65	514	150	371	12.36
7	17406	47219	65	501	145	337	12.46

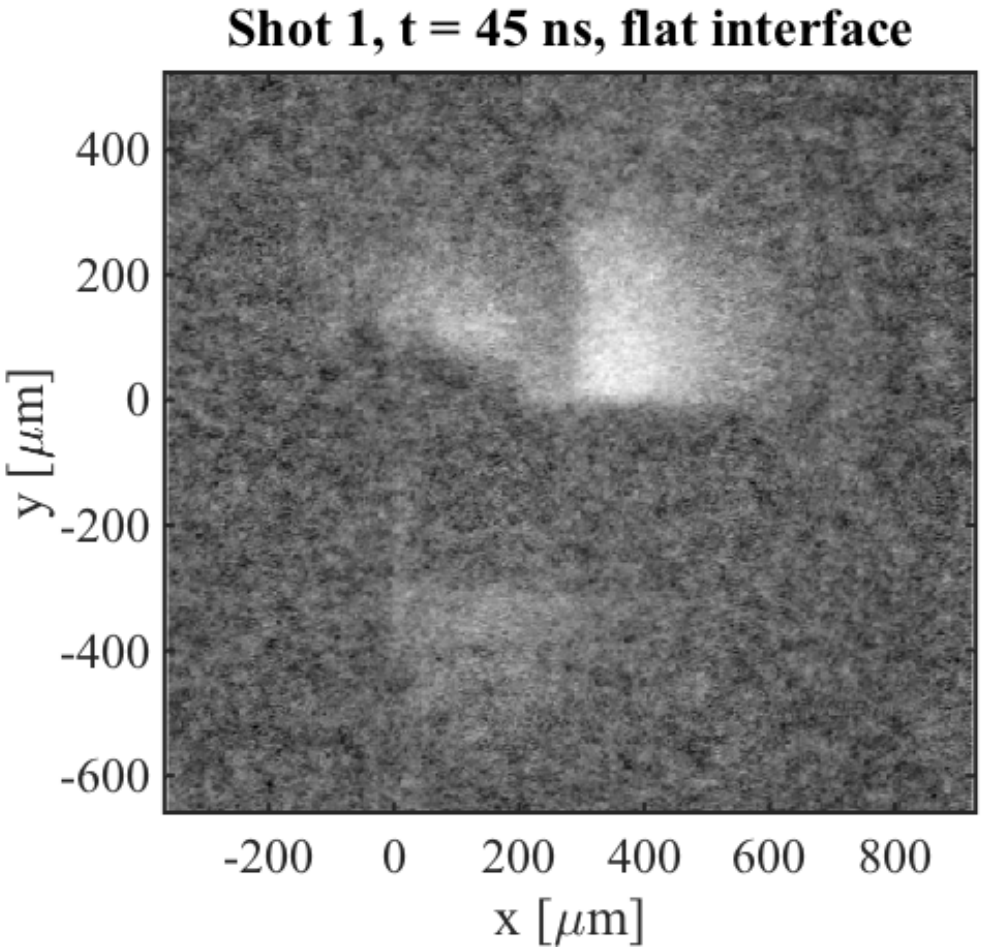

Figure D.1: Experiment 2, shot 1. x-ray radiograph taken at $t = 45$ ns. Backlighter at half energy. The blast shield (filter) in front of the image plate consisted of a stainless steel mesh and 40 mil of Be.

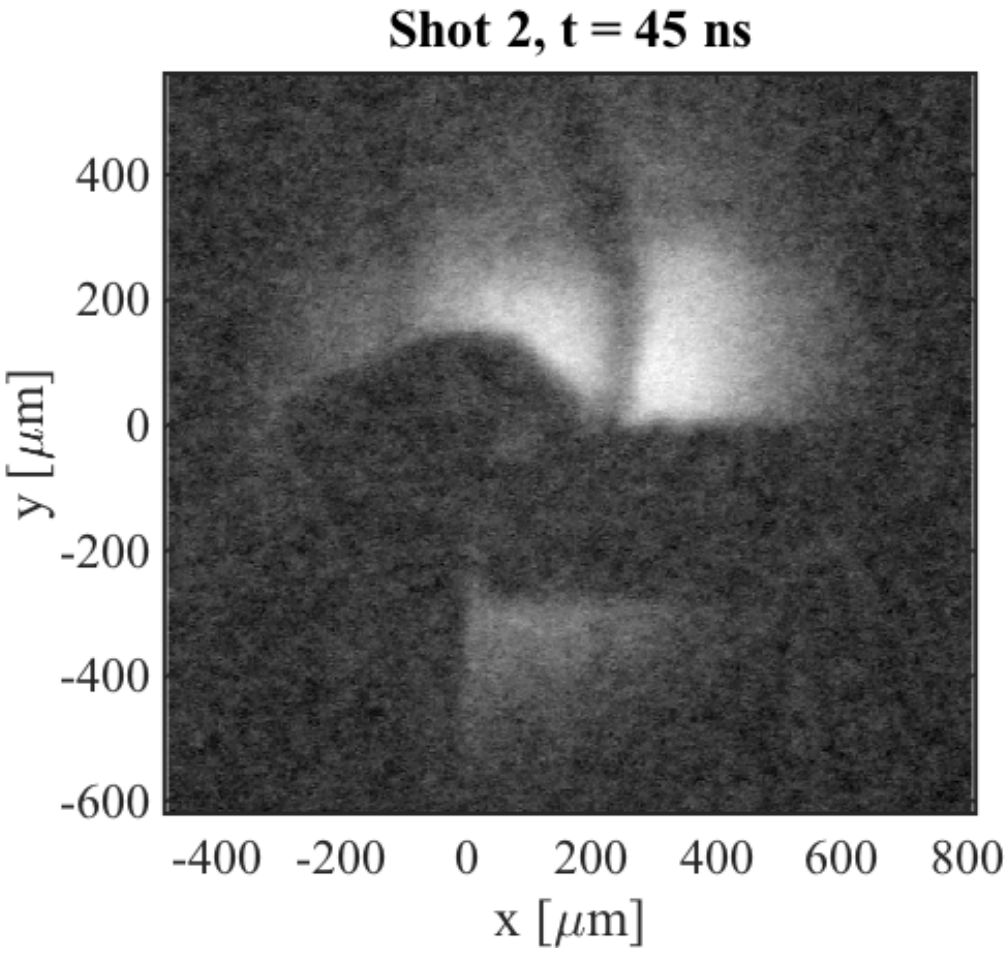

Figure D.2: Experiment 2, shot 2. x-ray radiograph taken at $t = 45$ ns. The blast shield (filter) in front of the image plate consisted of 40 mil of Be.

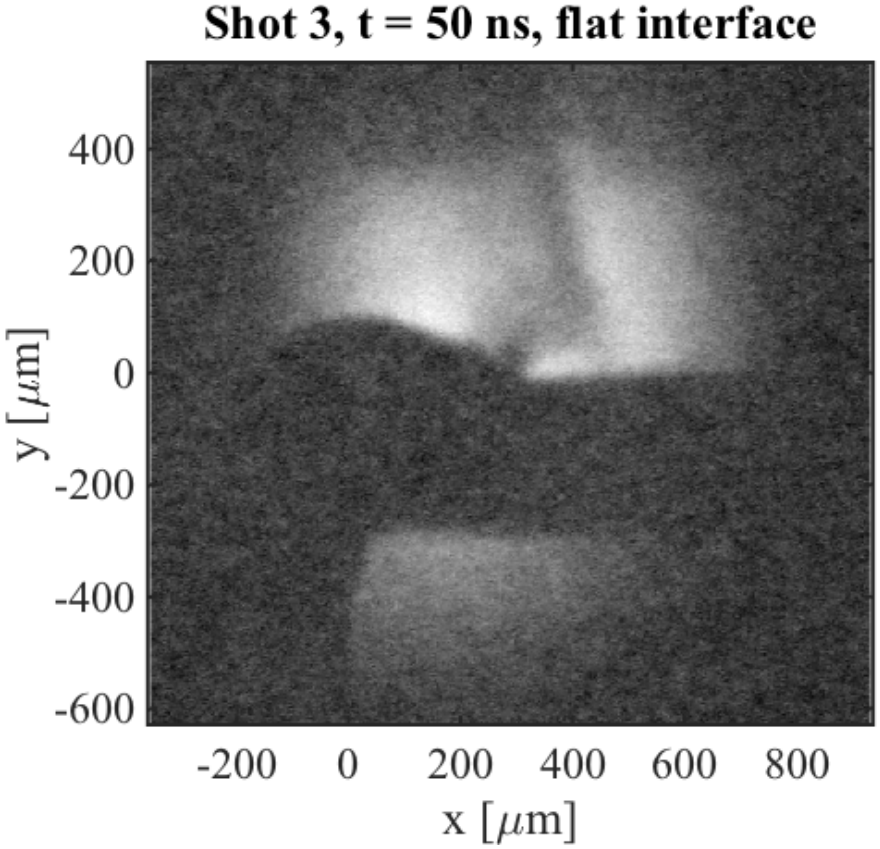

Figure D.3: Experiment 2, shot 3. x-ray radiograph taken at $t = 50$ ns. The blast shield (filter) in front of the image plate consisted of 40 mil of Be.

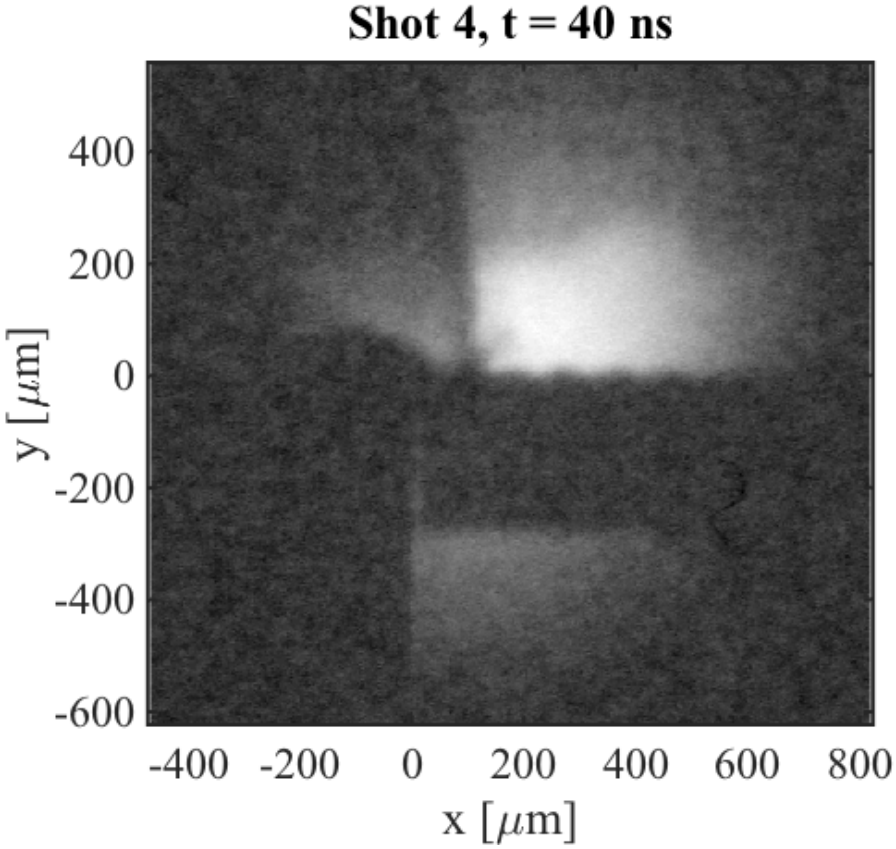

Figure D.4: Experiment 2, shot 4. x-ray radiograph taken at $t = 40$ ns. The blast shield (filter) in front of the image plate consisted of 30 mil of Be.

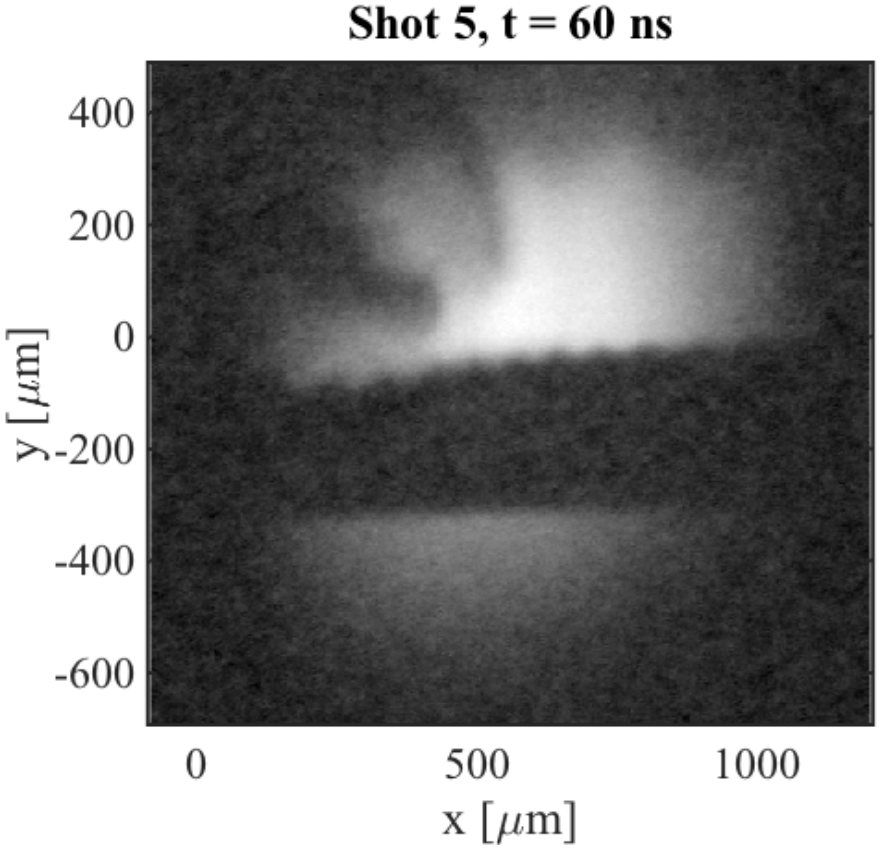

Figure D.5: Experiment 2, shot 5. x-ray radiograph taken at $t = 60$ ns. The blast shield (filter) in front of the image plate consisted of 30 mil of Be.

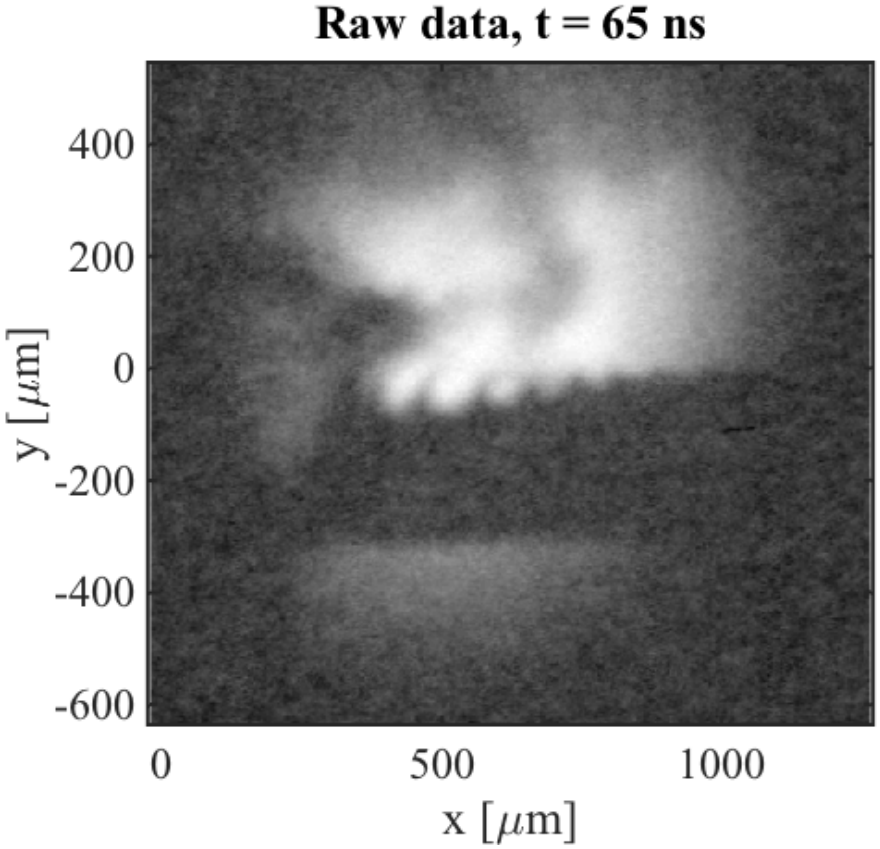

Figure D.6: Experiment 2, shot 6. x-ray radiograph taken at $t = 65$ ns. The blast shield (filter) in front of the image plate consisted of 30 mil of Be.

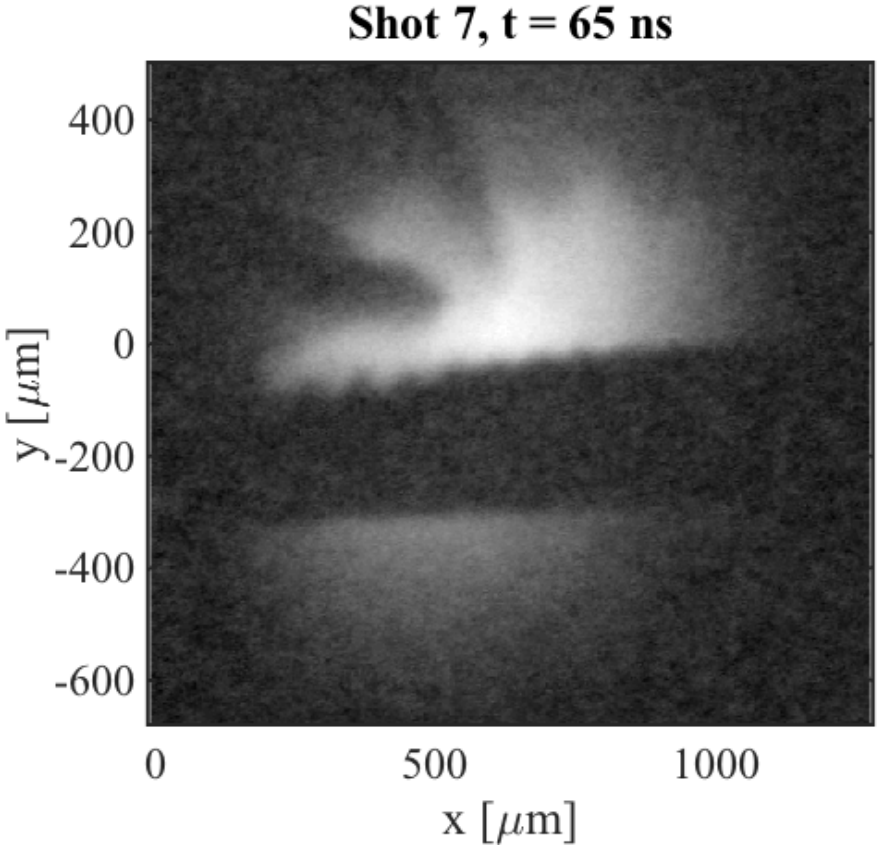

Figure D.7: Experiment 2, shot 7. x-ray radiograph taken at $t = 65$ ns. The blast shield (filter) in front of the image plate consisted of 30 mil of Be.

APPENDIX E

Dual-mode data

In this appendix, I present the x-ray radiographic images obtained from the vortex-merger experiment, discussed in Chapter IV. The are three perturbation styles, as described by Eq. 4.1. The first two perturbation styles, which we refer to as 60:120 ($\lambda_1 = 60$ μm, $\lambda_2 = 120$ μm) and 70:140 ($\lambda_1 = 70$ μm, $\lambda_2 = 140$ μm), produced the first observations for KHI vortex merger from well-characterized dual-mode initial conditions. The remaining perturbation style, referred to as 80:120 ($\lambda_1 = 80$ μm, $\lambda_2 = 120$ μm), can be considered a three-mode perturbation that produced inconclusive results. This perturbation style can be re-examined one diagnostic capabilities have been improved.

Also included is a table containing the facility's shot number for each piece of data, the shot request form (SRF) RID number (which can be used to look up the experimental setup and data for each shot), the time (after the start of the first laser) at which the radiographic image was taken, measurements of the thickness of the PC ablator, CHBr insulator, and high-Z block in the direction of the flow, and the total laser energy delivered to the target.

Table E.1: Shot log for the third experiment (dual-mode).

Shot number	Facility shot number	SRF RID	Time [ns]	PC width [μm]	CHBr width [μm]	Au width [μm]	Total energy [kJ]
1	21062	51548	45	511	186	343	12.55
2	21063	53437	65	516	183	347	13.03
3	21064	53438	65	520	174	350	12.56
4	21065	53439	65	510	165	329	13.00
5	21066	53440	68	509	158	350	12.62
6	21067	53441	68	510	158	359	12.67
7	21068	53442	68	512	176	345	12.51
8	21069	53489	68	506	182	338	12.50

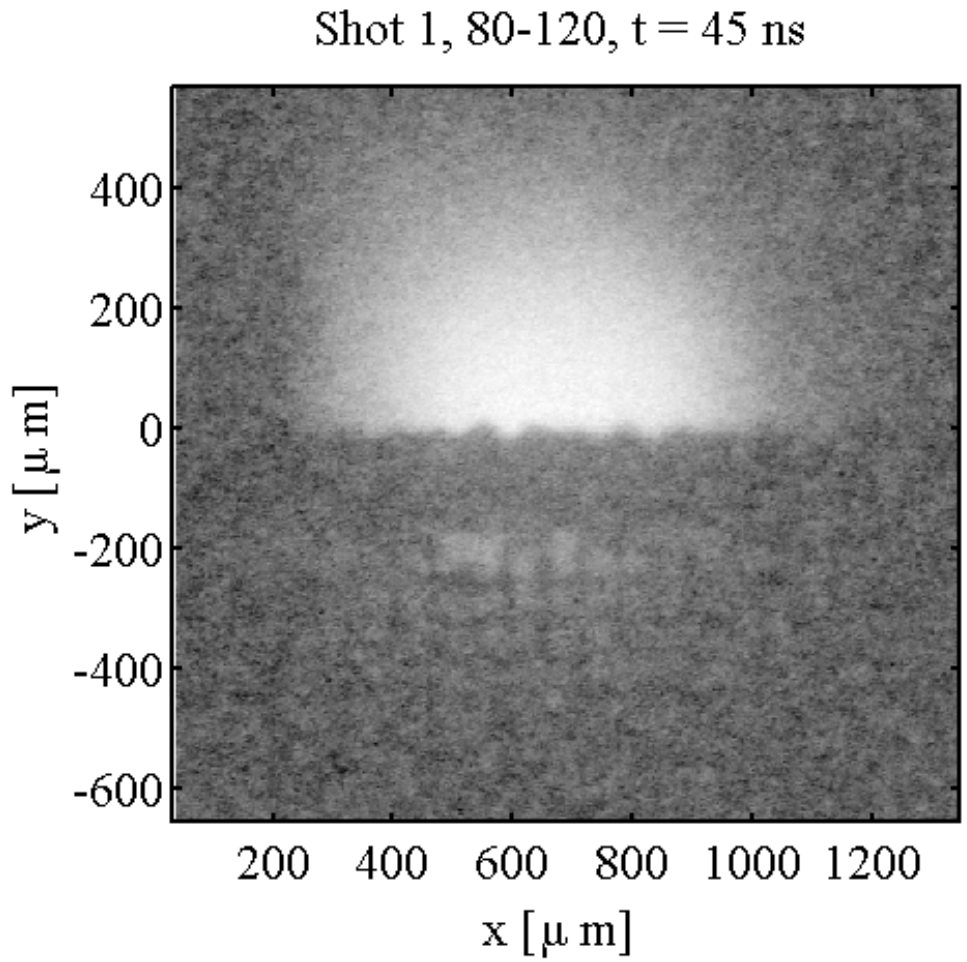

Figure E.1: Experiment 3, shot 1. x-ray radiograph taken at $t = 45$ ns with an 80:120 seed perturbation. Backlighter at half energy. The blast shield (filter) in front of the image plate consisted of a stainless steel mesh and 40 mil of Be.

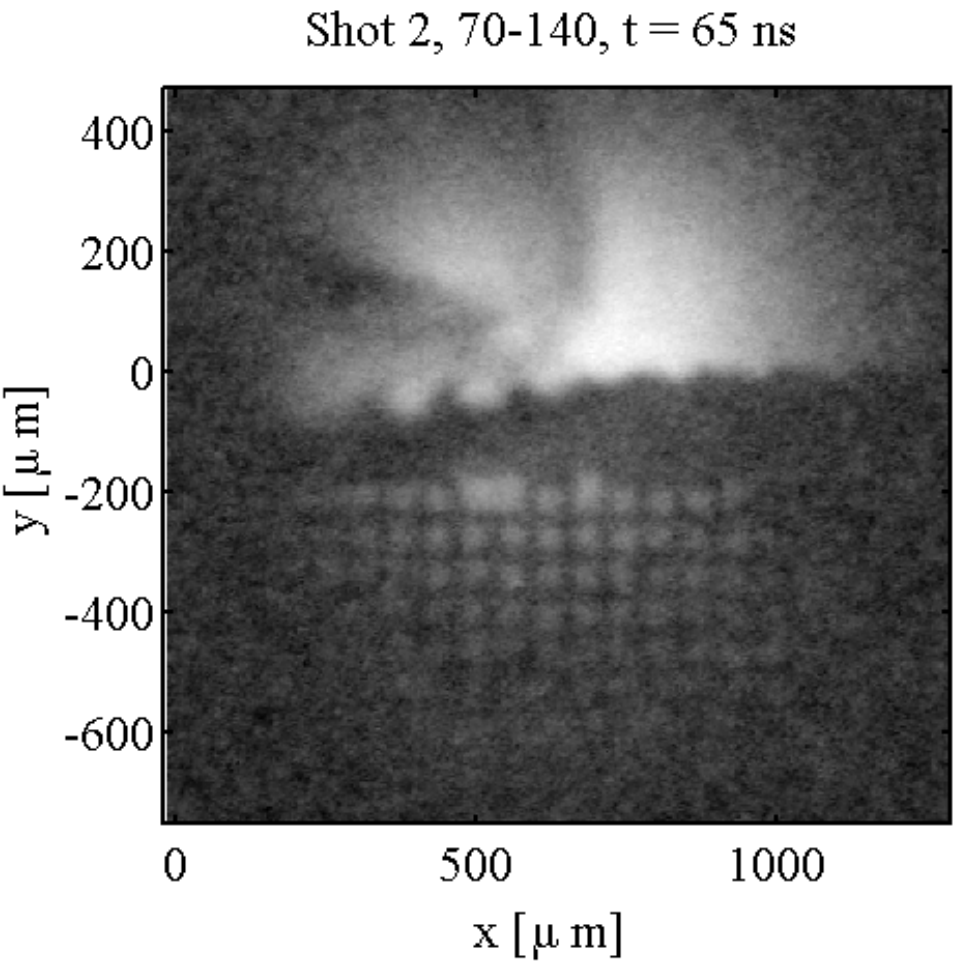

Figure E.2: Experiment 3, shot 2. x-ray radiograph taken at $t = 65$ ns with an 70:140 seed perturbation. The blast shield (filter) in front of the image plate consisted of a stainless steel mesh and 30 mil of Be.

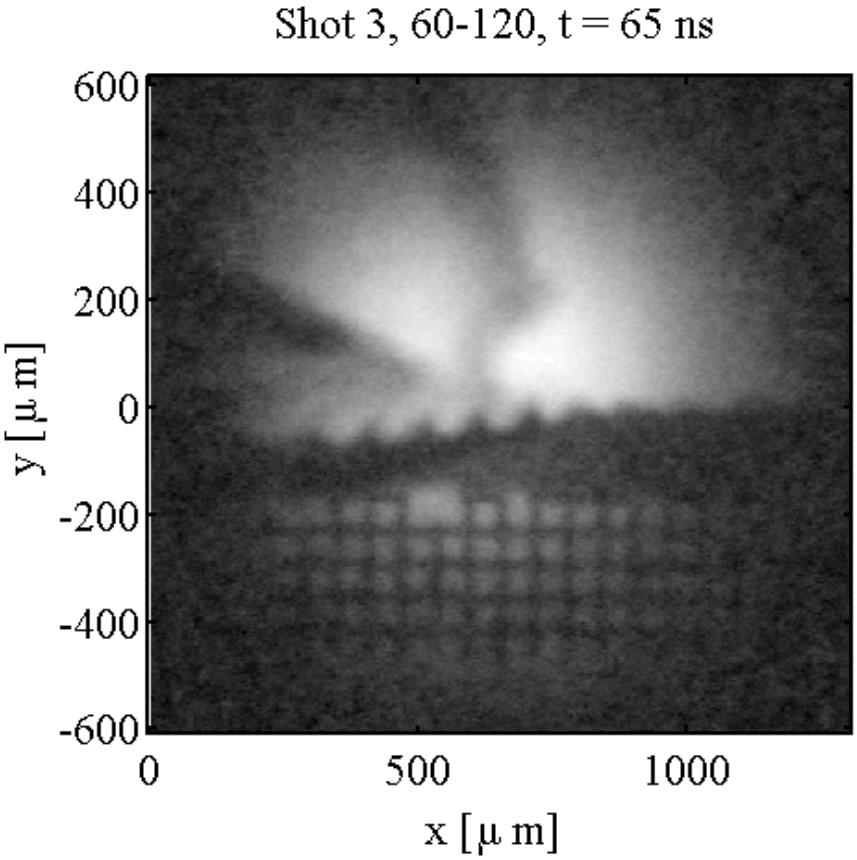

Figure E.3: Experiment 3, shot 3. x-ray radiograph taken at $t = 65$ ns with an 60:120 seed perturbation. The blast shield (filter) in front of the image plate consisted of 30 mil of Be.

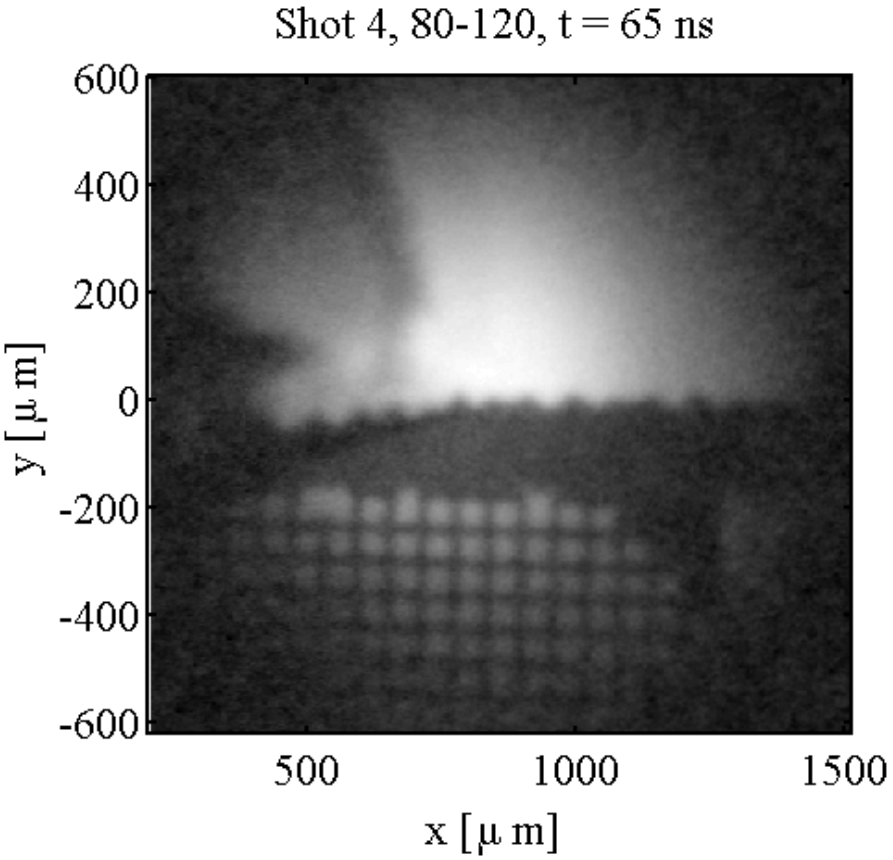

Figure E.4: Experiment 3, shot 4. x-ray radiograph taken at $t = 65$ ns with an 80:120 seed perturbation. The blast shield (filter) in front of the image plate consisted of 30 mil of Be.

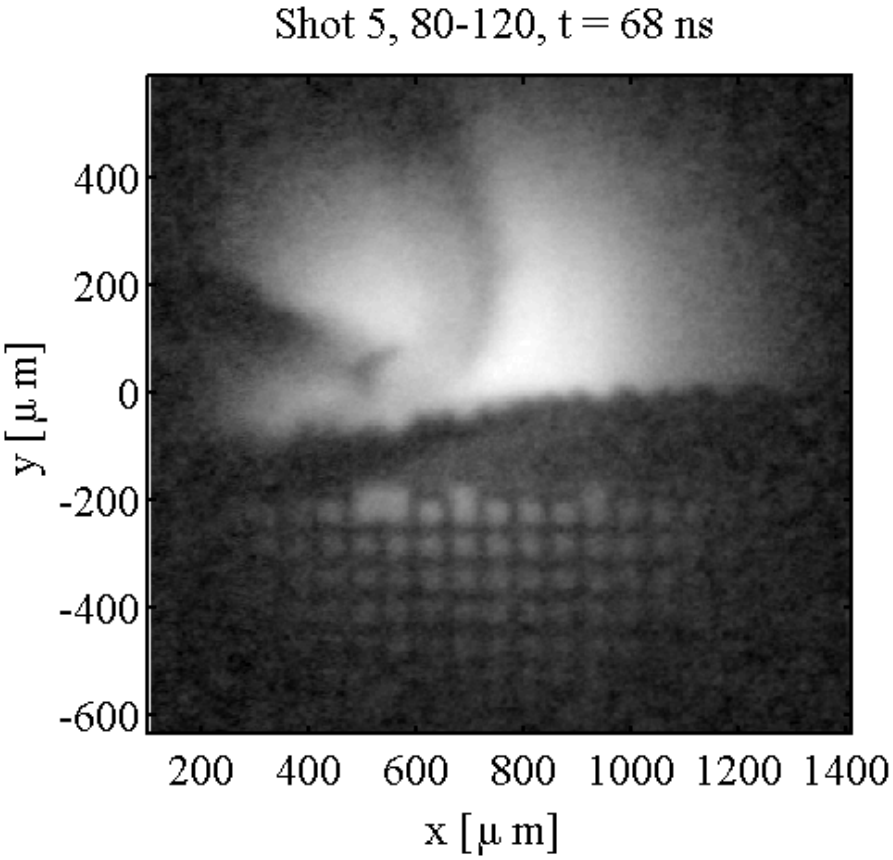

Figure E.5: Experiment 3, shot 5. x-ray radiograph taken at $t = 68$ ns with an 80:120 seed perturbation. The blast shield (filter) in front of the image plate consisted of 30 mil of Be.

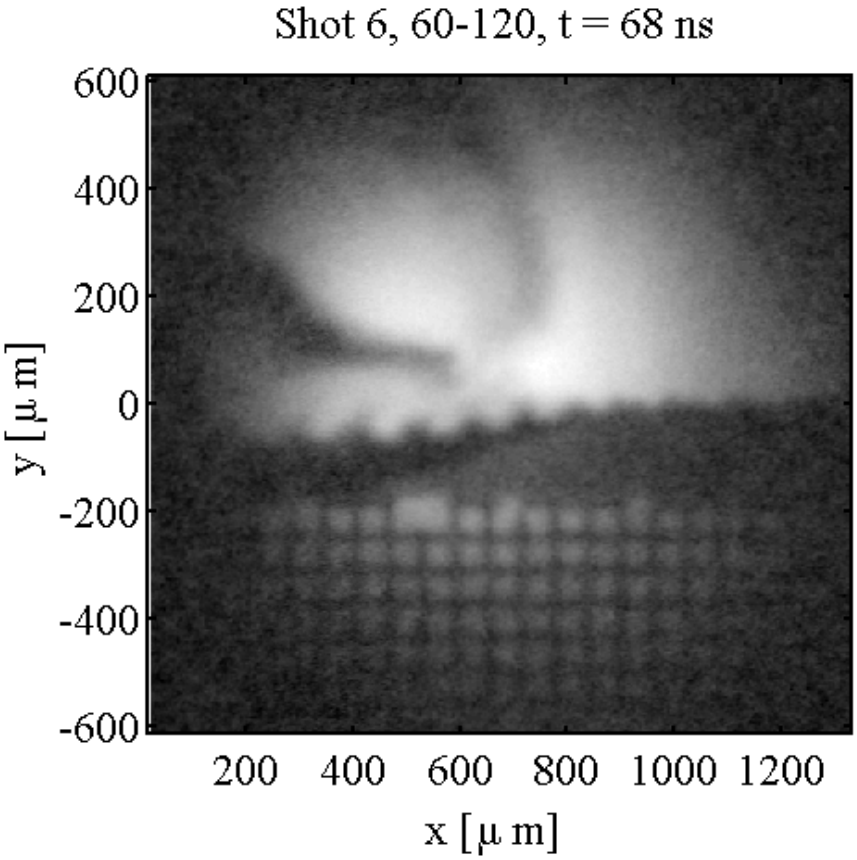

Figure E.6: Experiment 3, shot 6. x-ray radiograph taken at $t = 68$ ns with an 60:120 seed perturbation. The blast shield (filter) in front of the image plate consisted of 30 mil of Be.

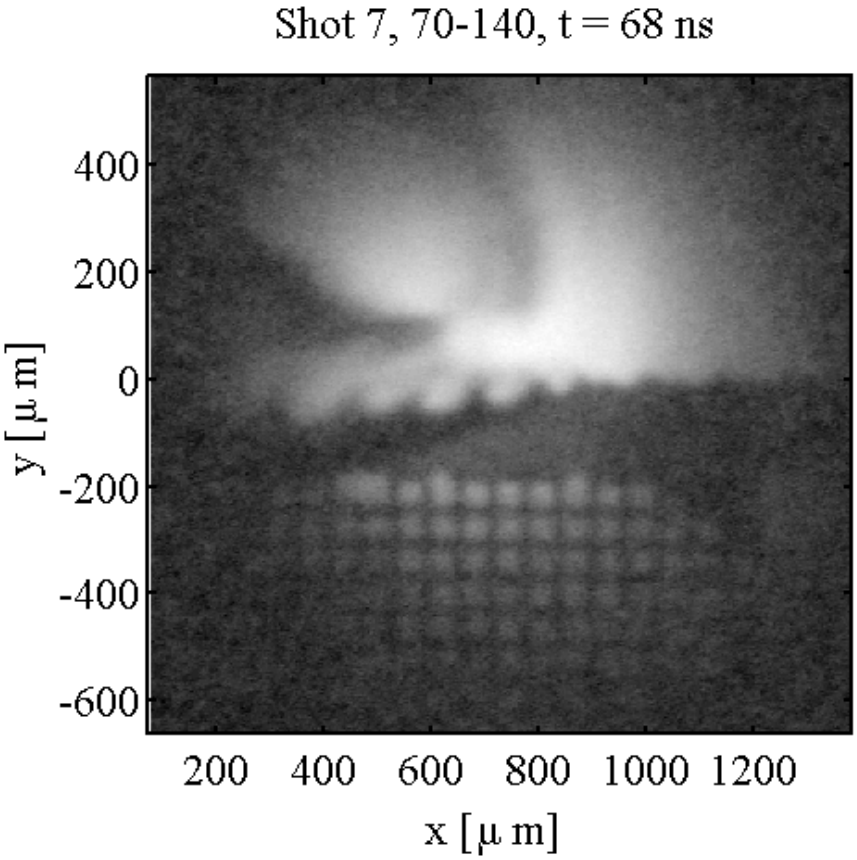

Figure E.7: Experiment 3, shot 7. x-ray radiograph taken at $t = 68$ ns with an 70:140 seed perturbation. The blast shield (filter) in front of the image plate consisted of 30 mil of Be.

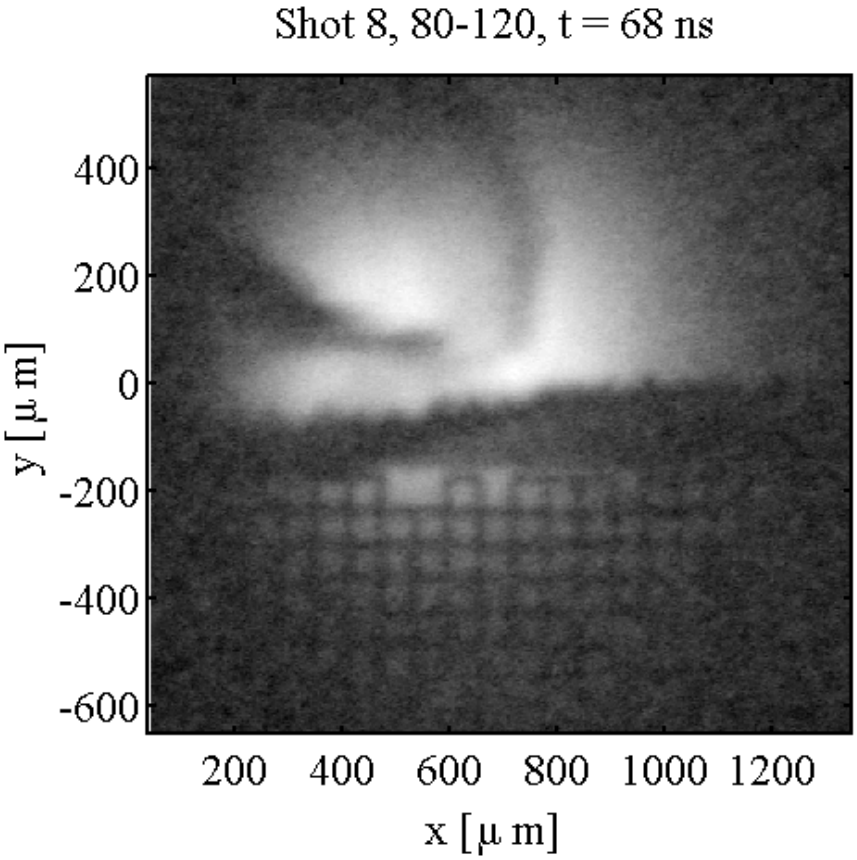

Figure E.8: Experiment 3, shot 8. x-ray radiograph taken at $t = 68$ ns with an 80:120 seed perturbation. The blast shield (filter) in front of the image plate consisted of 30 mil of Be.

APPENDIX F

Unsharp mask algorithm

This appendix contains the unsharp mask algorithm. The script was written for Matlab, and is used to enhance the contrast of our data.

```
function[sUN]=Unsharp(data,kernel,dx,stdev)

%s = data to manipulate
%kernel = kernel size in pixels to blur out
%dx = gaussian parameter, see equation
%stdev = gaussian parameter, see equation

kernel = fspecial('average', 3);    %feature size to blur out, in pixels
N = imfilter(data,kernel);
```

```
dy = dx;        %one of the Gaussian coefficients... symmetric in 2D
ConvE = 0;      %boolean for whether or not we've converged
NPix = 25;      %the function loops until we converge on ~1.  This affects
                %how quickly the size of the matrix grows.  Larger will
                %make the function converge quicker, but
hh = 0;         %index



%This uses a boolean to check whether or not there are any values in the
%matrix that are not a number, and displays an error message if there is.
ii=find(isnan(N)==1);
if (isempty(ii)==0)
  error('found nan');
end;



%This creates an appropriately sized gaussian kernel for convolution
while (ConvE==0)% & NPix<200)
    %Loops until the kernel size is sufficiently close to converging, or
    %until the kernel size is too large
    hh=hh+1;            %This increments each time the kernel size increases
  NPix=NPix+25;         %Every time this loops, we increase the size
   %of the kernel
  icen=NPix;            %Determines the size of the kernel.  The matrix is of
                        %size 1+2(icen), centered around zero, and counting up
```

```
                        %by 1.  i.e. if icen = 2, then aa = [2 1 0 1 2]
jcen=NPix;              %Same as icen for a square kernel

aa=abs([icen:-1:-icen]);  %Creates a temporary vector that acts as the
                          %initial column of the first temporary matrix
bb=aa'*ones(1,length(aa));
                          %Copies aa to each subsequent column.
                          %i.e. if aa = [1 0 1], then bb =    1 1 1
                          %                                   0 0 0
                          %                                   1 1 1
ggi=(bb*dx).^2;           %If dx = 1, then squares components of bb.

cc=abs([jcen:-1:-jcen]);   %Functionally the same as aa, if icen = jcen
                               % (square kernel)
dd=ones(length(cc),1)*cc; %Copies cc downwards as rows
                          %i.e. if cc = [1 0 1], then dd =    1 0 1
                          %                                   1 0 1
                          %                                   1 0 1
ggj=(dd*dy).^2;           %If dy = dx (square kernel), then this squares
                          %the components of temporary matrix dd

gg=1/stdev/stdev/pi*dx*dy*exp(-(ggi+ggj)/stdev/stdev);    %Combines gg1
                                %and gg2 into a gaussian

if (abs(sum(sum(gg)))-1<1e-11)    %boolean: If the gaussian is sufficiently
  ConvE=1;                        %close to 1, then set ConvE = 1 and end.
end                               %If not, then increase size and try again
```

```
if (NPix>200)                    %If the gaussian requires too large of a kernel
  error('not converging');       %before converging, then end w/error message
end
sConv=conv2(N,gg,'same');        %perform a 2D convolution using
                                 % the Gaussian we created

sUN = N-sConv;                   %Subtract out convolution

end
```

BIBLIOGRAPHY

BIBLIOGRAPHY

Alon, U., J. Hecht, D. Mukamel, and D. Shvarts (1994), Scale invariant mixing rates of hydrodynamically unstable interfaces, *Phys. Rev. Lett.*, *72*, 2867–2870, doi:10.1103/PhysRevLett.72.2867.

Alon, U., J. Hecht, D. Ofer, and D. Shvarts (1995), Power laws and similarity of rayleigh-taylor and richtmyer-meshkov mixing fronts at all density ratios, *Phys. Rev. Lett.*, *74*, 534–537, doi:10.1103/PhysRevLett.74.534.

Beck, C., S. Edwards, and M. King (2011a), The off-site plowshare and vela uniform programs - assessing potential environmental liabilities through an examination of proposed nuclear projects, high explosive experiments, and high explosive construction activities, vol i.

Beck, C., S. Edwards, and M. King (2011b), The off-site plowshare and vela uniform programs - assessing potential environmental liabilities through an examination of proposed nuclear projects, high explosive experiments, and high explosive construction activities, vol ii.

Beck, C., S. Edwards, and M. King (2011c), The off-site plowshare and vela uniform programs - assessing potential environmental liabilities through an examination of proposed nuclear projects, high explosive experiments, and high explosive construction activities, vol iii.

Betti, R., and O. Hurricane (2016), Inertial-confinement fusion with lasers, *Nature*, *12*, 435–448, doi:10.1038/nphys3736.

Betti, R., et al. (2006), Progress in hydrodynamics theory and experiments for direct-drive and fast ignition inertial confinement fusion, *Plasma Physics and Controlled Fusion*, *48*(12B), B153.

Bouzgarrou, G., Y. Bury, S. Jamme, J. F. Haas, D. Counilh, and J. B. Cazalbou (2012), *Experimental Characterization of Turbulence Produced in a Shock Tube: A Preliminary Work for the Study of the Turbulent Gaseous Mixing Induced by the Richtmyer-Meshkov Instability*, pp. 389–394, Springer Berlin Heidelberg, Berlin, Heidelberg, doi:10.1007/978-3-642-25685-1_59.

Brouillette, M. (2002), The richtmyer-meshkov instability, *Annual Review of Fluid Mechanics*, *34*, 445–468, doi:10.1146/annurev.fluid.34.090101.162238.

Brown, G. L., and A. Roshko (1974), On density effects and large structure in turbulent mixing layers, *Journal of Fluid Mechanics*, *64*(4), 775–816, doi:10.1017/S002211207400190X.

Buckingham, E. (1914), On physically similar systems; illustrations of the use of dimensional equations, *Phys. Rev.*, *4*, 345–376, doi:10.1103/PhysRev.4.345.

Buckingham, E. (1915), The principle of similitude, *Nature*, *96*, 396–397, doi:10.1038/096396d0.

Budil, K. S., B. A. Remington, T. A. Peyser, K. O. Mikaelian, P. L. Miller, N. C. Woolsey, W. M. Wood-Vasey, and A. M. Rubenchik (1996), Experimental comparison of classical versus ablative rayleigh-taylor instability, *Phys. Rev. Lett.*, *76*, 4536–4539, doi:10.1103/PhysRevLett.76.4536.

Capelli, D., et al. (2016), Development of indirectly driven shock tube targets for counter-propagating shear-driven kelvin-helmholtz experiments on the national ignition facility, *Fusion Science and Technology*, *70*(2), 316–323, doi:http://dx.doi.org/10.13182/FST15-229.

Chandrasekhar, S. (1961), Hydrodynamic and hydromagnetic stability, in *International Series of Monographs on Physics*, Oxford: Clarendon.

Chapman, P. R., and J. W. Jacobs (2006), Experiments on the three-dimensional incompressible richtmyer-meshkov instability, *Physics of Fluids*, *18*(7), 074101, doi:http://dx.doi.org/10.1063/1.2214647.

Choudhury, S. (1997), Nonlinear evolution of the kelvin-helmholtz instability of supersonic tangential velocity discontinuities, *Journal of Mathematical Analysis and Applications*, *214*(2), 561 – 586, doi:http://dx.doi.org/10.1006/jmaa.1997.5594.

Cole, A., J. Kilkenny, P. Rumsby, R. Evans, C. Hooker, and M. Key (1982), Measurement of rayleigh-taylor instability in a laser-accelerated target, *Nature*, *229*, 329–331, doi:10.1038/299329a0.

Couder, Y., and C. Basdevant (1986), Experimental and numerical study of vortex couples in two-dimensional flows, *Journal of Fluid Mechanics*, *173*, 225–251.

Craxton, R. (1995), Distributed phase plates for super-gaussian focal-plane irradiance profiles.

Craxton, R. S., et al. (2015), Direct-drive inertial confinement fusion: A review, *Physics of Plasmas*, *22*(11), 110,501, doi:10.1063/1.4934714.

Delamere, P. A., R. J. Wilson, S. Eriksson, and F. Bagenal (2013), Magnetic signatures of kelvin-helmholtz vortices on saturn's magnetopause: Global survey, *Journal of Geophysical Research*, *118*, 303–404, doi:http://dx.doi.org/10.1029/2012JA018197.

Desselberger, M., O. Willi, M. Savage, and M. J. Lamb (1990), Measurement of the rayleigh-taylor instability in targets driven by optically smoothed laser beams, *Phys. Rev. Lett.*, *65*, 2997–3000, doi:10.1103/PhysRevLett.65.2997.

Di Stefano, C., G. Malamud, C. Kuranz, S. Klein, and R. Drake (2015a), Measurement of richtmyer-meshkov mode coupling under steady shock conditions and at high energy density, *High Energy Density Physics*, *17, Part B*, 263 – 269, doi:http://dx.doi.org/10.1016/j.hedp.2015.09.001.

Di Stefano, C. A., G. Malamud, C. C. Kuranz, S. R. Klein, C. Stoeckl, and R. P. Drake (2015b), Richtmyer-meshkov evolution under steady shock conditions in the high-energy-density regime, *Applied Physics Letters*, *106*(11), 114103, doi:http://dx.doi.org/10.1063/1.4915303.

Di Stefano, C. A., et al. (2014), Observation and modeling of mixing-layer development in high-energy-density, blast-wave-driven shear flow), *Physics of Plasmas (1994-present)*, *21*(5), 056306, doi:http://dx.doi.org/10.1063/1.4872223.

Dimonte, G., and M. Schneider (1997), Turbulent richtmyer-meshkov instability experiments with strong radiatively driven shocks, *Physics of Plasmas*, *4*(12), 4347–4357, doi:10.1063/1.872597.

Dimonte, G., C. E. Frerking, M. Schneider, and B. Remington (1996), Richtmyer-meshkov instability with strong radiatively driven shocks, *Physics of Plasmas*, *3*(2), 614–630, doi:10.1063/1.871889.

Dimotakis, P. (1986), Two-dimensional shear-layer entrainment, *American Institute of Aeronautics and Astronautics (AIAA) Journal*, *24*(11), 1791–1796, doi:http://dx.doi.org/10.2514/3.9525.

Doss, F. W., J. R. Fincke, E. N. Loomis, L. Welser-Sherrill, and K. A. Flippo (2013a), The high-energy-density counterpropagating shear experiment and turbulent self-heating, *Physics of Plasmas*, *20*(12), 122,704, doi:10.1063/1.4839115.

Doss, F. W., E. N. Loomis, L. Welser-Sherrill, J. R. Fincke, K. A. Flippo, and P. A. Keiter (2013b), Instability, mixing, and transition to turbulence in a laser-driven counterflowing shear experiment, *Physics of Plasmas (1994-present)*, *20*(1), 012707, doi:http://dx.doi.org/10.1063/1.4789618.

Doss, F. W., K. A. Flippo, and E. C. Merritt (2016), Observation and analysis of emergent coherent structures in a high-energy-density shock-driven planar mixing layer experiment, *Phys. Rev. E*, *94*, 023,101, doi:10.1103/PhysRevE.94.023101.

Doss, F. W., et al. (2015), The shock/shear platform for planar radiation-hydrodynamics experiments on the national ignition facility, *Physics of Plasmas*, *22*(5), 056,303, doi:10.1063/1.4918354.

Drake, R. (2006), Hydrodynamic instabilities, in *High-Energy-Density Physics*, edited by Y. H. L. Davison, Springer, New York.

Drake, R. P. (2010), High-energy-density physics, *Physics Today*, *63*(6), 28–33, doi: 10.1063/1.3455249.

Dritschel, D. G. (1989), On the stabilization of a two-dimensional vortex strip by adverse shear, *Journal of Fluid Mechanics*, *206*, 193–221.

Ebisuzaki, T., T. Shigeyama, and K. Nomoto (1989), Rayleigh-Taylor instability and mixing in SN 1987A, *Astrophysical Journal*, *344*, L65–L68, doi:10.1086/185532.

Edwards, M. J., et al. (2013), Progress towards ignition on the national ignition facility, *Physics of Plasmas*, *20*(7), 070,501, doi:10.1063/1.4816115.

Feng, L., B. Inhester, and W. Q. Gan (2013), Kelvin-Helmholtz instability of a coronal streamer, *Astrophysical Journal Letters*, *774*(2), 141, doi:10.1088/2041-8205/729/1/L8.

Feynman, R., R. Leighton, and M. Sands (1964), Electromagnetism, in *The Feynman Lectures on Physics, Volume. II*, Addison-Wesley Publishing Company, Reading, Massachusetts.

Flippo, K. A., et al. (2016), Late-time mixing sensitivity to initial broadband surface roughness in high-energy-density shear layers, *Phys. Rev. Lett.*, *117*, 225,001, doi: 10.1103/PhysRevLett.117.225001.

Freeman, J., M. Clauser, and S. Thompson (1977), Rayleigh-taylor instabilities in inertial-confinement fusion targets, *Nuclear Fusion*, *17*(2), 223.

Freymuth, P. (1966), On transition in a separated laminar boundary layer, *Journal of Fluid Mechanics*, *25*(4), 683–704.

Frisch, U. (1995), Phenomenology of turbulence in the sense of kolmogorov 1941, in *Turbulence: the legacy of A.N. Kolmogorov.*, Cambridge University Press., Cambridge.

Fromang, S., J. Leconte, and K. Heng (2016), Shear-driven instabilities and shocks in the atmospheres of hot jupiters, *Astronomy & Astrophysics*, *591*, A144, doi: 10.1051/0004-6361/201527600.

Gardner, C. L., and S. J. Dwyer (2009), Numerical simulation of the {XZ} tauri supersonic astrophysical jet, *Acta Mathematica Scientia*, *29*(6), 1677 – 1683, doi: http://dx.doi.org/10.1016/S0252-9602(10)60010-0.

Glendinning, S. G., et al. (2003), Effect of shock proximity on richtmyer-meshkov growth, *Physics of Plasmas*, *10*(5), 1931–1936, doi:http://dx.doi.org/10.1063/1.1562165.

Glimm, J., and D. H. Sharp (1990), Chaotic mixing as a renormalization-group fixed point, *Phys. Rev. Lett.*, *64*, 2137–2139, doi:10.1103/PhysRevLett.64.2137.

Gombosi, T. I. (1998), *Physics of the Space Environment*, 339 pp., Cambridge University Press, Cambridge, UK.

Gresh, L. (2009), Nuclear fusion 201, in *Inertial Confinement Fusion: An Introduction - The Energy of the Stars*, edited by L. Gresh, University of Rochester, Rochester, New York.

Griffith, W. (1952), Shock-tube studies of transonic flow over wedge profiles, *Journal of Aeronautical Sciences*, *19*, 249–257.

Grove, J. (1999), Frontier: A compressible hydrodynamics front tracking code. A short course in front tracking. Los Alamos National Laboratory Report LA-UR 99-3985.

Grun, J., et al. (1987), Rayleigh-taylor instability growth rates in targets accelerated with a laser beam smoothed by induced spatial incoherence, *Phys. Rev. Lett.*, *58*, 2672–2675, doi:10.1103/PhysRevLett.58.2672.

Guzman, J., and T. Plewa (2009), Non-spherical core-collapse supernovae: evolution towards homologous expansion, *Nonlinearity*, *22*(11), 2775.

Hammel, B. A., J. D. Kilkenny, D. Munro, B. A. Remington, H. N. Kornblum, T. S. Perry, D. W. Phillion, and R. J. Wallace (1994), X-ay radiographic imaging of hydrodynamic phenomena in radiation-driven materials shock propagation, material compression, and shear flow*, *Physics of Plasmas*, *1*(5), 1662–1668, doi:10.1063/1.870668.

Hänsch, T. W. (2010), 50 years of laser. celebrating an invention that changed our lives, *Laser & Photonics Reviews*, *4*(1), A5–A6, doi:10.1002/lpor.201000502.

Harding, E. (2010), Observations of shear flows in high-energy-density plasmas, Ph.D. thesis, University of Michigan.

Harding, E., R. Drake, Y. Aglitskiy, R. Gillespie, M. Grosskopf, J. Weaver, A. Velikovich, A. Visco, and J. Ditmar (2010a), Experimental design to generate strong shear layers in a high-energy-density plasma, *High Energy Density Physics*, *6*(2), 179 – 184, doi:http://dx.doi.org/10.1016/j.hedp.2010.01.013, {ICHED} 2009 - 2nd International Conference on High Energy Density Physics.

Harding, E. C., et al. (2009), Observation of a kelvin-helmholtz instability in a high-energy-density plasma on the omega laser, *Phys. Rev. Lett.*, *103*, 045,005, doi:10.1103/PhysRevLett.103.045005.

Harding, E. C., et al. (2010b), Laser driven supersonic flow over a compressible foam surface on the nike laser, *Physics of Plasmas*, *17*(5), 056,310, doi:10.1063/1.3314335.

Helmholtz, H. (1868), Über discontinuierliche flüssigkeits-bewegungen (on the discontinuous movements of fluids), *Monatsberichte der Koniglichen Preussiche Akademie der Wissenschaften zu Berlin [Monthly Reports of the Royal Prussian Academy of Philosophy in Berlin], Philosophical Magazine Series 4*, *36*(244), 337–346, doi:10.1080/14786446808640073.

Henshall, B. (1957), On some aspects of the use of shock tubes in aerodynamic research, *Aeronautical Research Council Reports and Memoranda*, *3044*.

Holt, J. (1998), Experiments on kelvin-helmholtz billows influenced by boundaries, *Geophysical & Astrophysical Fluid Dynamics*, *89*(3-4), 205–233, doi:10.1080/03091929808203686.

Horton, W., J. C. Perez, T. Carter, and R. Bengtson (2005), Vorticity probes and the characterization of vortices in the kelvin-helmholtz instability in the large plasma device experiment, *Physics of Plasmas*, *12*(2), 022,303, doi:10.1063/1.1830489.

Hurricane, O. (2008), Design for a high energy density kelvin-helmholtz experiment, *High Energy Density Physics*, *4*(3-4), 97 – 102, doi:http://dx.doi.org/10.1016/j.hedp.2008.02.002.

Hurricane, O. A., J. F. Hansen, H. F. Robey, B. A. Remington, M. J. Bono, E. C. Harding, R. P. Drake, and C. C. Kuranz (2009), A high energy density shock driven kelvin-helmholtz shear layer experiment, *Physics of Plasmas*, *16*(5), 056,305, doi:10.1063/1.3096790.

Hurricane, O. A., et al. (2010), Understanding the implications of the data from recent high-energy-density kelvin-helmholtz shear layer experiments, *Journal of Physics: Conference Series*, *244*(4), 042,007.

Hurricane, O. A., et al. (2011), Blast-wave driven kelvin-helmholtz shear layers in a laser driven high-energy-density plasma, *Astrophysics and Space Science*, *336*(1), 139–143, doi:10.1007/s10509-010-0571-z.

Hurricane, O. A., et al. (2012), Validation of a turbulent kelvin-helmholtz shear layer model using a high-energy-density omega laser experiment, *Phys. Rev. Lett.*, *109*, 155,004, doi:10.1103/PhysRevLett.109.155004.

Itoh, M., S. Kumagai, T. Shigeyama, K. Nomoto, and J. Nishimura (1987), X-rays expected from supernova 1987A compared with the source discovered by the GINGA satellite, *Nature*, *330*, 233–235, doi:10.1038/330233a0.

Johnson, J. R., S. Wing, and P. A. Delamere (2014), Kelvin helmholtz instability in planetary magnetospheres, *Space Science Reviews*, *184*(1), 1–31, doi:10.1007/s11214-014-0085-z.

Kane, J., D. Arnett, B. A. Remington, S. G. Glendinning, J. Castor, R. Wallace, A. Rubenchik, and B. A. Fryxell (1997), Supernova-relevant hydrodynamic instability experiments on the nova laser, *The Astrophysical Journal Letters*, *478*(2), L75.

Kane, J., D. Arnett, B. A. Remington, S. G. Glendinning, G. Bazan, R. P. Drake, and B. A. Fryxell (2000), Supernova experiments on the nova laser, *The Astrophysical Journal Supplement Series*, *127*(2), 365.

Kartoon, D., D. Oron, L. Arazi, and D. Shvarts (2003), Three-dimensional multimode rayleigh-taylor and richtmyer-meshkov instabilities at all density ratios, *Laser and Particle Beams*, *21*(3), 327–334, doi:10.1017/S0263034603213069.

Kelvin, W. T. L. (1871), Hydrokinetic solutions and observations, *The London, Edinburgh, and Dublin Philosophical Magazine and Journal of Science, Philosophical Magazine Series 4*, *42*(281), 362–377, doi:10.1080/14786447108640585.

Keppens, R., G. Tóth, R. Westermann, and J. Goedbloed (1999), Growth and saturation of the kelvin-helmholtz instability with parallel and antiparallel magnetic fields, *Journal of Plasma Physics*, *61*(1), 119, doi:10.1017/S0022377898007223.

Kilkenny, J. D. (1990), Experimental results on hydrodynamic instabilities in laser-accelerated planar packages, *Physics of Fluids B: Plasma Physics*, *2*(6), 1400–1404, doi:10.1063/1.859563.

Konrad., J. (1977), An experimental investigation of mixing in two-dimensional turbulent shear flows with applications to diffusion-limited chemical reactions, Ph.D. thesis, California Institute of Technology.

Kundu, P., and I. Cohen (2000), Chapter 12 - Instability, in *Fluid Mechanics, 4th ed.*, Elsevier Inc.

Kundu, P., and I. Cohen (2012), Chapter 11 - Instability, in *Fluid Mechanics, 5th ed.*, Elsevier Inc.

Landau, L. (1944), Stability of a tangential discontinuity in a compressible liquid, *Dokl. Akad. Nauk SSSR*, *44*(4), 151–153.

Larsen, J. T., and S. M. Lane (1994), Hyades – plasma hydrodynamics code for dense plasma studies, *Journal of Quantitative Spectroscopy and Radiative Transfer*, *51*(1-2), 179 – 186, doi:http://dx.doi.org/10.1016/0022-4073(94)90078-7, special Issue Radiative Properties of Hot Dense Matter.

Ledingham, K. W. D., and W. Galster (2010), Laser-driven particle and photon beams and some applications, *New Journal of Physics*, *12*(4), 045,005.

Li, C. K., et al. (2012), Impeding hohlraum plasma stagnation in inertial-confinement fusion, *Phys. Rev. Lett.*, *108*, 025,001, doi:10.1103/PhysRevLett.108.025001.

Liepmann, H., and J. Laufer (1947), Investigations of free turbulent mixing, *National Advisory Committee for Aeronautics - Technical Note*, *1257*.

Lindl, J. (1993), The edward teller medal lecture: The evolution toward indirect drive and two decades of progress toward icf ignition and burn.

MacPhee, A. G., et al. (), X-ray shadow imprint of hydrodynamic instabilities on the surface of inertial-confinement-fusion capsules by the fuel fill tube, *Physical Review E, accepted for publication*.

Maddox, B. R., et al. (2011), High-energy x-ray backlighter spectrum measurements using calibrated image plates, *Review of Scientific Instruments*, *82*(2), 023111, doi: http://dx.doi.org/10.1063/1.3531979.

Malamud, G., C. Di Stefano, Y. Elbaz, C. Huntington, C. Kuranz, P. Keiter, and R. Drake (2013a), A design of a two-dimensional, multimode {RM} experiment on omega-ep, *High Energy Density Physics*, *9*(1), 122 – 131, doi:http://dx.doi.org/10.1016/j.hedp.2012.11.008.

Malamud, G., A. Shimony, W. Wan, C. Di Stefano, Y. Elbaz, C. Kuranz, P. Keiter, R. Drake, and D. Shvarts (2013b), A design of a two-dimensional, supersonic kh experiment on omega-ep, *High Energy Density Physics*, *9*(4), 672 – 686, doi:http://dx.doi.org/10.1016/j.hedp.2013.06.002.

Malamud, G., E. Leinov, O. Sadot, Y. Elbaz, G. Ben-Dor, and D. Shvarts (2014), Reshocked richtmyer-meshkov instability: Numerical study and modeling of random multi-mode experiments, *Physics of Fluids*, *26*(8), 084107, doi:http://dx.doi.org/10.1063/1.4893678.

Marinak, M. M., B. A. Remington, S. V. Weber, R. E. Tipton, S. W. Haan, K. S. Budil, O. L. Landen, J. D. Kilkenny, and R. Wallace (1995), Three-dimensional single mode rayleigh-taylor experiments on nova, *Phys. Rev. Lett.*, *75*, 3677–3680, doi:10.1103/PhysRevLett.75.3677.

Martinez, D., R. Presura, S. Wright, C. Plechatys, S. Neff, L. Wanex, and D. Ampleford (2009), Generation of shear flow in conical wire arrays with a center wire, *Astrophysics and Space Science*, *322*(1-4), 205–208, copyright - Springer Science+Business Media B.V. 2009; Document feature - ; Last updated - 2014-08-09.

Maywar, D. N., et al. (2008), Omega ep high-energy petawatt laser: progress and prospects, *Journal of Physics: Conference Series*, *112*(3), 032,007.

McCrory, R. L., et al. (2008), Progress in direct-drive inertial confinement fusion, *Physics of Plasmas*, *15*(5), 055,503, doi:10.1063/1.2837048.

McFarland, J., D. Reilly, S. Creel, C. McDonald, T. Finn, and D. Ranjan (2013), Experimental investigation of the inclined interface richtmyer–meshkov instability before and after reshock, *Experiments in Fluids*, *55*(1), 1–14, doi:10.1007/s00348-013-1640-1.

Melander, M. V., J. C. Mcwilliams, and N. J. Zabusky (1987a), Axisymmetrization and vorticity-gradient intensification of an isolated two-dimensional vortex through filamentation, *Journal of Fluid Mechanics*, *178*, 137–159.

Melander, M. V., N. J. Zabusky, and J. C. McWilliams (1987b), Asymmetric vortex merger in two dimensions: Which vortex is "victorious"?, *The Physics of Fluids*, *30*(9), 2610–2612, doi:10.1063/1.866103.

Melander, M. V., N. J. Zabusky, and J. C. Mcwilliams (1988), Symmetric vortex merger in two dimensions: causes and conditions, *Journal of Fluid Mechanics*, *195*, 303–340.

Merritt, E. C., F. W. Doss, E. N. Loomis, K. A. Flippo, and J. L. Kline (2015), Modifying mixing and instability growth through the adjustment of initial conditions in a high-energy-density counter-propagating shear experiment on omega, *Physics of Plasmas*, *22*(6), 062,306, doi:10.1063/1.4922910.

Meshkov, E. E. (1969), Instability of the interface of two gases accelerated by a shock wave, *Fluid Dynamics*, *4*(5), 101–104, doi:10.1007/BF01015969.

Mikaelian, K. O. (1994), Oblique shocks and the combined rayleigh-taylor, kelvin-helmholtz, and richtmyer-meshkov instabilities, *Physics of Fluids*, *6*(6), 1943–1945, doi:http://dx.doi.org/10.1063/1.868198.

Miura, A., and P. L. Pritchett (1982), Nonlocal stability analysis of the mhd kelvin-helmholtz instability in a compressible plasma, *Journal of Geophysical Research: Space Physics*, *87*(A9), 7431–7444, doi:10.1029/JA087iA09p07431.

Molvig, K., M. J. Schmitt, B. J. Albright, E. S. Dodd, N. M. Hoffman, G. H. McCall, and S. D. Ramsey (2016), Low fuel convergence path to direct-drive fusion ignition, *Phys. Rev. Lett.*, *116*, 255,003, doi:10.1103/PhysRevLett.116.255003.

Moody, J. D., et al. (2014), Progress in hohlraum physics for the national ignition facility), *Physics of Plasmas (1994-present)*, *21*(5), 056317, doi:http://dx.doi.org/10.1063/1.4876966.

Nagel, S. R., et al. (2015), Effect of the mounting membrane on shape in inertial confinement fusion implosions, *Physics of Plasmas*, *22*(2), 022,704, doi:10.1063/1.4907179.

Nishimura, H., et al. (1988), Hydrodynamic instability in an ablatively imploded target irradiated by high power green lasers, *The Physics of Fluids*, *31*(10), 2875–2883, doi:10.1063/1.866996.

Nuckolls, J. (1998), Early steps toward inertial fusion energy (ife) (1952 to 1962); report number urcl-id-131075, doi:http://dx.doi.org/10.2172/658936.

Nuckolls, J., L. Wood, A.Thiessen, and G. Zimmerman (1972), Laser compression of matter to super-high densities: thermonuclear (ctr) applications, *Nature*, *239*, 139–142, doi:http://dx.doi.org/10.1038/239139a0.

Oron, D., L. Arazi, D. Kartoon, A. Rikanati, U. Alon, and D. Shvarts (2001), Dimensionality dependence of the rayleigh-taylor and richtmyer-meshkov instability late-time scaling laws, *Physics of Plasmas*, *8*(6), 2883–2889, doi:http://dx.doi.org/10.1063/1.1362529.

Oron, D., et al. (1999), Studies in the nonlinear evolution of the rayleigh-taylor and richtmyer-meshkov instabilities and their role in inertial confinement fusion, *Laser and Particle Beams*, *17*(3), 465–475.

Overman II, E. A., and N. J. Zabusky (1982), Evolution and merger of isolated vortex structures, *The Physics of Fluids*, *25*(8), 1297–1305, doi:10.1063/1.863907.

Papamoschou, D., and A. Roshko (1988), Observations of supersonic free shear layers, *Sadhana*, *12*(1), 1–14, doi:10.1007/BF02745657.

Paral, J., and R. Rankin (2013), Dawn-dusk asymmetry in the kelvin-helmholtz instability at mercury, *Nature*, *4*, doi:10.1038/ncomms2676.

Patnaik, P. C., F. S. Sherman, and G. M. Corcos (1976), A numerical simulation of kelvin-helmholtz waves of finite amplitude, *Journal of Fluid Mechanics*, *73*, 215–240, doi:10.1017/S0022112076001353.

Payman, W., and W. Shepherd (1946), Explosion waves and shock waves vi. the disturbance produced by bursting diaphragms with compressed air, *Proceedings of the Royal Society of London*, *186*, 293, doi:10.1098/rspa.1946.0045.

Peyser, T. A., P. L. Miller, P. E. Stry, K. S. Budil, E. W. Burke, D. A. Wojtowicz, D. L. Griswold, B. A. Hammel, and D. W. Phillion (1995), Measurement of radiation-driven shock-induced mixing from nonlinear initial perturbations, *Phys. Rev. Lett.*, *75*, 2332–2335, doi:10.1103/PhysRevLett.75.2332.

Pfalzner, S. (2006), Fundamentals of inertial confinement fusion, in *An Introduction to Inertial Confinement Fusion*, edited by S. Cowley, Taylor & Francis Group, LLC, New York.

Pickworth, L. A., et al. (2016), Measurement of hydrodynamic growth near peak velocity in an inertial confinement fusion capsule implosion using a self-radiography technique, *Phys. Rev. Lett.*, *117*, 035,001, doi:10.1103/PhysRevLett.117.035001.

Pope, A., and K. Goin (1978), , in *High-Speed Wind Tunnel Testing*, Krieger Pub. Co., New York.

Pozrikidis, C., and J. J. L. Higdon (1985), Nonlinear kelvin-helmholtz instability of a finite vortex layer, *Journal of Fluid Mechanics*, *157*, 225–263, doi:10.1017/S0022112085002361.

Raman, K. S., et al. (2012), Three-dimensional modeling and analysis of a high energy density kelvin-helmholtz experiment, *Physics of Plasmas*, *19*(9), 092,112, doi:10.1063/1.4752018.

Rayleigh (1882), Investigation of the character of the equilibrium of an incompressible heavy fluid of variable density, *Proceedings of the London Mathematical Society*, *s1-14*(1), 170–177, doi:10.1112/plms/s1-14.1.170.

Remington, B. A., S. W. Haan, S. G. Glendinning, J. D. Kilkenny, D. H. Munro, and R. J. Wallace (1992), Large growth, planar rayleigh-taylor experiments on nova, *Physics of Fluids B: Plasma Physics*, *4*(4), 967–978, doi:10.1063/1.860113.

Remington, B. A., et al. (1997), Supernova hydrodynamics experiments on the nova laser, *Physics of Plasmas*, *4*(5), 1994–2003, doi:10.1063/1.872341.

Remington, B. A., et al. (2016), Hydrodynamic instabilities and mix studies on nif: predictions, observations, and a path forward, *Journal of Physics: Conference Series*, *688*(1), 012,090.

Remington, B. A., et al. (2017), Mixing with applications to inertial-confinement-fusion implosions, *Physical Review E*, *95*(1).

Richtmyer, R. D. (1960), Taylor instability in shock acceleration of compressible fluids, *Communications on Pure and Applied Mathematics*, *13*(2), 297–319, doi:10.1002/cpa.3160130207.

Rikanati, A., U. Alon, and D. Shvarts (1998), Vortex model for the nonlinear evolution of the multimode richtmyer-meshkov instability at low atwood numbers, *Phys. Rev. E*, *58*, 7410–7418, doi:10.1103/PhysRevE.58.7410.

Rikanati, A., U. Alon, and D. Shvarts (2003), Vortex-merger statistical-mechanics model for the late time self-similar evolution of the kelvin-helmholtz instability, *Physics of Fluids*, *15*(12), 3776–3785, doi:http://dx.doi.org/10.1063/1.1624837.

Robey, H. F., et al. (2016), Performance of indirectly driven capsule implosions on the national ignition facility using adiabat-shaping, *Physics of Plasmas*, *23*(5), 056,303, doi:10.1063/1.4944821.

Rutter, E., M. Grosskopf, G. Malamud, C. Kuranz, E. Harding, P. Keiter, and R. Drake (2013), Comparison between kelvin-helmholtz instability experiments on {OMEGA} and simulation results using the {CRASH} code, *High Energy Density Physics*, *9*(1), 148 – 151, doi:http://dx.doi.org/10.1016/j.hedp.2012.12.002.

Sadot, O., L. Erez, U. Alon, D. Oron, L. A. Levin, G. Erez, G. Ben-Dor, and D. Shvarts (1998), Study of nonlinear evolution of single-mode and two-bubble interaction under richtmyer-meshkov instability, *Phys. Rev. Lett.*, *80*, 1654–1657, doi:10.1103/PhysRevLett.80.1654.

Sadot, O., V. A. Smalyuk, J. A. Delettrez, D. D. Meyerhofer, T. C. Sangster, R. Betti, V. N. Goncharov, and D. Shvarts (2005), Observation of self-similar behavior of the 3d, nonlinear rayleigh-taylor instability, *Phys. Rev. Lett.*, *95*, 265,001, doi: 10.1103/PhysRevLett.95.265001.

Schubauer, G. B., and H. K. Skramstad (1947), Laminar boundary-layer oscillations and transition on a flat plate, *Journal of Research of the National Bureau of Standards*, *38*, 251–292.

Sharma, R., and K. Srivastava (1968), Effects of horizontal and vertical magnetic fields on kelvin-helmholtz instability, *Australian Journal of Physics*, *21*, 917–921, doi:10.1071/PH680917.

Sharp, D. (1984), An overview of rayleigh-taylor instability, *Physica D: Nonlinear Phenomena*, *12*(1), 3 – 18, doi:http://dx.doi.org/10.1016/0167-2789(84)90510-4.

Shimony, A. (2016), The development of kelvin-helmholtz instability in high mach numbers, Ph.D. thesis, Ben Gurion University of the Negev, Department of Physics.

Shimony, A., D. Shvarts, G. Malamud, C. Di Stefano, C. Kuranz, and R. Drake (2016a), The effect of a dominant initial single mode on the kelvin-helmholtz instability evolution: New insights on previous experimental results, *Journal of Fluids Engineering*, *138*(7), 070,902, doi:http://dx.doi.org/10.1115/1.4032530.

Shimony, A., W. Wan, G. Malamud, S. Klein, R. Drake, C. Kuranz, and D. Shvarts (2016b), Compressible nonlinear multimode kelvin-helmholtz instability - theory, simulations, and experimental validation, *Submitted to Physical Review Letters*.

Shvarts, D., et al. (2000), Scaling laws of nonlinear rayleigh-taylor and richtmyer-meshkov instabilities in two and three dimensions, *Comptes Rendus de l'Académie des Sciences - Series IV - Physics*, *1*(6), 719 – 726, doi:http://dx.doi.org/10.1016/S1296-2147(00)01077-5.

Shyh, C., and B. Munson (1985), Interfacial instability of an oscillating shear layer, *Journal of Fluids Engineering*, *108*(1), 89–92, doi:10.1115/1.3242549.

Siegel, K. (1974), KMS Announces Major New Progress in Obtaining Energy from Laser Fusion, in *K.M. Siegel papers, 1953-1983*, Bentley Historical Library, University of Michigan.

Slessor, M. (1998), Aspects of turbulent-shear-layer dynamics and mixing, Ph.D. thesis, California Institute of Technology.

Slessor, M., M. Zhuang, and P. Dimotakis (2000), Turbulent shear-layer mixing: growth-rate compressibility scaling, *Journal of Fluid Mechanics*, *414*, 35–45, doi: http://dx.doi.org.proxy.lib.umich.edu/10.1017/S0022112099006977.

Slutz, S. A., R. A. Vesey, and M. C. Herrmann (2007), Compensation for time-dependent radiation-drive asymmetries in inertial-fusion capsules, *Phys. Rev. Lett.*, *99*, 175,001, doi:10.1103/PhysRevLett.99.175001.

Smalyuk, V., et al. (2013), Measurements of turbulent mixing due to kelvin-helmholtz instability in high-energy-density plasmas, *High Energy Density Physics*, *9*(1), 47 – 51, doi:http://dx.doi.org/10.1016/j.hedp.2012.10.001.

Smalyuk, V. A. (2012), Experimental techniques for measuring rayleigh-taylor instability in inertial confinement fusion, *Physica Scripta*, *86*(5), 058,204.

Smalyuk, V. A., S. X. Hu, J. D. Hager, J. A. Delettrez, D. D. Meyerhofer, T. C. Sangster, and D. Shvarts (2009), Spherical rayleigh-taylor growth of three-dimensional broadband perturbations on omega, *Physics of Plasmas*, *16*(11), 112701, doi:http://dx.doi.org/10.1063/1.3253321.

Smalyuk, V. A., et al. (2012), Experimental observations of turbulent mixing due to kelvin-helmholtz instability on the omega laser facility, *Physics of Plasmas (1994-present)*, *19*(9), 092702, doi:http://dx.doi.org/10.1063/1.4752015.

Spencer, B., and B. Jones (1971), Statistical investigation of pressure and velocity fields in the turbulent two-stream mixing layer, *4th Fluid and Plasma Dynamics Conference*, doi:10.2514/6.1971-613.

Srinivasan, B., and X.-Z. Tang (2014), Role of hydrodynamic instability growth in hot-spot mass gain and fusion performance of inertial confinement fusion implosions, *Physics of Plasmas*, *21*, 102,704, doi:10.1063/1.4897938.

Stoeckl, C., G. Fiksel, D. Guy, C. Mileham, P. M. Nilson, T. C. Sangster, M. J. Shoup, and W. Theobald (2012), A spherical crystal imager for omega ep, *Review of Scientific Instruments*, *83*(3), 033107, doi:http://dx.doi.org/10.1063/1.3693348.

Takaki, R., and L. S. G. Kovasznay (1978), Statistical theory of vortex merger in the two-dimensional mixing layer, *Physics of Fluids*, *21*(2), 153–156, doi:http://dx.doi.org/10.1063/1.862208.

Taylor, G. (1950a), The instability of liquid surfaces when accelerated in a direction perpendicular to their planes. i, *Proceedings of the Royal Society of London A: Mathematical, Physical and Engineering Sciences*, *201*(1065), 192–196, doi:10.1098/rspa.1950.0052.

Taylor, G. (1950b), The formation of a blast wave by a very intense explosion. i. theoretical discussion, *Proceedings of the Royal Society of London. Series A, Mathematical and Physical Sciences*, *201*(1065), 159–174.

Taylor, G. (1950c), The formation of a blast wave by a very intense explosion. ii. the atomic explosion of 1945, *Proceedings of the Royal Society of London. Series A, Mathematical and Physical Sciences*, *201*(1065), 175–186.

Thorpe, S. A., and J. T. Holt (1995), The effects of laterally sloping upper and lower boundaries on waves and instability in stratified shear flows, *Journal of Fluid Mechanics*, *286*, 49–65.

Titus, J. B., A. B. Alexander, and J. A. J. III (2013), Note: A high mach number arc-driven shock tube for turbulence studies, *Review of Scientific Instruments*, *84*(4), 046,102, doi:10.1063/1.4799176.

Town, R. P. J., et al. (2014), Dynamic symmetry of indirectly driven inertial confinement fusion capsules on the national ignition facility, *Physics of Plasmas*, *21*(5), 056,313, doi:10.1063/1.4876609.

Turner, J. (1973), The stability of a free shear layer, in *Buoyancy effects in fluids*, edited by G. Batchelor, Cambridge University Press, New York.

van der Holst, B., et al. (2011), Crash: A block-adaptive-mesh code for radiative shock hydrodynamics-implementation and verification, *The Astrophysical Journal Supplement Series*, *194*(2), 23.

van Haren, H., and L. Gostiaux (2010), A deep-ocean kelvin-helmholtz billow train, *Geophysical Research Letters*, *37*(3), n/a–n/a, doi:10.1029/2009GL041890, l03605.

Velarde, G. (2002), Academician nikolai g. basov: the father of inertial fusion. a scientific and human approach, *Quantum Electronics*, *32*(12), 1038.

Vieille, P. (1899), Sur les discontinuites produites par la detente brusque de gas comprimes, *Comptes Rendus*, *129*, 1229.

Wan, W., et al. (2017a), Impact of ablator thickness and laser drive duration on a platform for supersonic, shockwave-driven hydrodynamic instability experiments, *High Energy Density Physics*, *22*, 6 – 11, doi:http://dx.doi.org/10.1016/j.hedp.2016.12.001.

Wan, W. C., G. Malamud, A. Shimony, C. A. Di Stefano, M. R. Trantham, S. R. Klein, D. Shvarts, C. C. Kuranz, and R. P. Drake (2015), Observation of single-mode, kelvin-helmholtz instability in a supersonic flow, *Phys. Rev. Lett.*, *115*, 145,001, doi:10.1103/PhysRevLett.115.145001.

Wan, W. C., G. Malamud, A. Shimony, C. A. D. Stefano, M. R. Trantham, S. R. Klein, D. Shvarts, R. P. Drake, and C. C. Kuranz (2017b), Observation of dual-mode, kelvin-helmholtz instability vortex merger in a compressible flow, *Physics of Plasmas*, *24*(5), 055,705, doi:10.1063/1.4982061.

Wark, J. S., J. D. Kilkenny, A. J. Cole, M. H. Key, and P. T. Rumsby (1986), Observations of the rayleigh-taylor instability in laser imploded microballoons, *Applied Physics Letters*, *48*(15), 969–971, doi:10.1063/1.96626.

Welser-Sherrill, L., J. Fincke, F. Doss, E. Loomis, K. Flippo, D. Offermann, P. Keiter, B. Haines, and F. Grinstein (2013), Two laser-driven mix experiments to study reshock and shear, *High Energy Density Physics*, *9*(3), 496 – 499, doi:http://dx.doi.org/10.1016/j.hedp.2013.04.015.

Whitlock, R. R., M. H. Emery, J. A. Stamper, E. A. McLean, S. P. Obenschain, and M. C. Peckerar (1984), Observation of rayleigh-taylor-like structures in a laser-accelerated foil, *Phys. Rev. Lett.*, *52*, 819–822, doi:10.1103/PhysRevLett.52.819.

Winant, C., and F. Browand (1974), Vortex pairing : the mechanism of turbulent mixing-layer growth at moderate reynolds number, *Journal of Fluid Mechanics*, *63*(2), 237–255.

Wright, S., R. Presura, A. Esaulov, S. Neff, C. Plechaty, D. Martinez, and A. Haboub (2009), Kelvin-helmholtz instabilities actuated by an external magnetic field, *Astrophysics and Space Science*, *322*(1-4), 201–204.

Wygnanski, I., and H. E. Fiedler (1970), The two-dimensional mixing region, *Journal of Fluid Mechanics*, *41*(2), 327–361.

Yamanaka, C. (1999), Inertial confinement fusion: The quest for ignition and energy gain using indirect drive, *Nuclear Fusion*, *39*(6), 825.

Yoshikawa, H., and J. Wesfreid (2011a), Oscillatory kelvin-helmholtz instability. part 1. a viscous theory, *Journal of Fluid Mechanics*, *675*, 223–248.

Yoshikawa, H., and J. Wesfreid (2011b), Oscillatory kelvin-helmholtz instability. part 2. an experiment in fluids with a large viscosity contrast, *Journal of Fluid Mechanics*, *675*, 249–267.

Zhelyazkov, I. (2015), On modeling the kelvin–helmholtz instability in solar atmosphere, *Journal of Astrophysics and Astronomy*, *36*(1), 233–254, doi:10.1007/s12036-015-9332-2.

Zylstra, A. B., et al. (2014), The effect of shock dynamics on compressibility of ignition-scale national ignition facility implosions, *Physics of Plasmas*, *21*(11), 112701, doi:http://dx.doi.org/10.1063/1.4900621.